In Vitro and *In Vivo* Macromolecular Dynamics - From Biofilaments to Living Cells

Inauguraldissertation

zur
Erlangung der Würde eines Doktors der Philosophie
vorgelegt der
Philosophisch-Naturwissenschaftlichen Fakultät
der Universität Basel

von

Natalja Strelnikova

aus

Jelgava, Lettland

Basel, 2017

Genehmigt von der Philosophisch-Naturwissenschaftlichen Fakultät auf Antrag von:

Prof. Dr. Wolfgang Meier, Dr. Thomas Pfohl und Prof. Dr. Cornelia Palivan

Basel, 18.04.2017

Prof. Dr. Martin Spiess

Abstract

Studying macromolecules and living cells dynamics *in situ* significantly contribute to the understanding of various biological processes in living organisms. The biopolymer actin is one of the major building blocks of the cytoskeleton and is further crucial for numerous biological processes. Numerous mechanical responses of the cell including deformation and movement are based on physical properties of cytoskeletal networks, which are influenced by chemical gradients and modulate cytoskeletal functionality. In order to analyze the formation and properties of actin networks in concentration gradients, we developed multi-height microfluidic devices with diffusion-controlled microchambers. This unique approach enables for creating flow-free, steady state concentration gradients of different profiles, such as linear or step-like.

Specific features of actin networks emerging in defined gradients are investigated. In particular, we analyzed the effects of spatial conditions on network properties, bending rigidities of network links, and the network elasticity.

Furthermore, we study the actin filaments as a model system for semiflexible polymers in microfluidic flow. Filamentous actin facing hydrodynamic forces undergo conformational transitions and analyzing their behavior provides a better understanding of non-Newtonian fluids in microchannels and in living organisms. We introduce a microfluidic device with wide and narrow channel segments, resulting in flow fields of spatially varying flow strength. These structured microchannels with alternating high- and low-velocity segments generate non-equilibrium and non-stationary alternating stretch-coil and coil-stretch transitions of fluorescently labeled actin filaments. We study the

conformational transitions of filaments with different contour lengths and at different flow velocities. When the filament enters the wider section of the channel they coil under compression, whereas they are starching with a suppression of thermal fluctuations in the extensional regime during reentering the narrow part of the channel. Actin filaments exposed to hydrodynamic forces in structured microchannels with high- and low-velocity segments were characterized by center of mass velocity changes, the evolution of end-to-end distances and bending energies of the filament passing through the channel.

Another biopolymer being essential for all known forms of life is DNA. We study the reversible process of DNA packing and unpacking, which is crucial for cell functioning. In eukaryotic cells, the DNA is wrapped around histone proteins, creating repeatable subunits called nucleosomes, which are then further folded into the chromosomes. For the experiments, histones were replaced by a positively charged, nearly spherical and biocompatible polyamidoamine (PAMAM) dendrimers of generation 6 (G6). In analogy to the histone, PAMAM G6 forms complexes with the DNA through sequence-independent, electrostatic interaction between the negatively charged nucleic acid and the protonated, positively charged dendrimer. We analyze the DNA / PAMAM G6 complex organization at different pH of the solution. Moreover, we study DNA decondensation, which is essential for processes such as transcription, replication and repair. DNA unwrapping was initiated by the DNA / PAMAM G6 complex interaction with heparin, which is highly negatively charged and serves as the competitive agent for DNA. First, DNA compaction and decompaction measurements were performed in glass capillaries using small angle X-ray scattering (SAXS), where we successfully analyzed structural changes of the DNA / PAMAM G6 complexes. Furthermore, specially developed microfluidic devices allow the measurement of the reaction dynamics of these processes. Using X-ray compatible, hydrodynamic focusing microfluidic devices with chevron/herringbone structures, we analyzed the real-time dynamics of DNA release from artificial gene carriers at different heparin concentrations.

In this thesis, studies of live cell X-ray imaging are also discussed. Visualization of nanoscale features in living cells is very desirable for investigations of intracellular structures. We use X-ray ptychography to directly explore the dynamics of unstained living fission yeast *Schizosaccharomyces pombe* cells during meiosis in a natural, aqueous environment. X-ray imaging techniques allow us to investigate soft matter of several micrometers thickness in hydrated states without labeling at nanoscale resolution. We show that it is possible to make a sequence of X-ray images of living cells, which was not feasible so far and additionally, visualize the dynamic changes. Cells were alive even after several ptychographic X-ray scans and we obtained a sequence of X-ray images of individual living fission yeast, which allowed us to visualize and examine the meiotic nuclear oscillations and autophagic cell death subsequently induced by the ionizing radiation. Furthermore, the accumulated radiation after each scan allowed for a precise determination of the critical X-ray doses of autophagic vacuole formation and the lethal dose for fission yeast. This method enables looking at living biological samples and processes in a time-resolved label-free setting.

Contents

1. Introduction 1

1.1 Dynamics of biomacromolecules 1

1.2 Out of equilibrium experiments 5

1.2.1 Microfluidics 5

1.2.2 The combination of microfluidics and small angle X-ray scattering (SAXS) 8

1.3 *In vitro* studies of actin and DNA dynamics 9

1.4 Lensless X-ray imaging 12

1.4.1 X-ray Ptychography 13

1.5 *In vivo* studies of dynamical changes of living cells 15

1.6 Outline of the thesis 17

2. Dynamic Studies of DNA Using Small-Angle X-ray Scattering 19

2.1 Electrostatic interactions of DNA 19

2.1.1 DNA interactions with artificial gene carriers 22

2.1.2 DNA compaction at different pH 23

2.1.3 DNA decompaction and controlled release 24

2.2 SAXS and Microfluidics 25

2.2.1 SAXS 25

2.2.2 Fast mixing microfluidic device 28

2.2.3 The liquid crystal n-octyl-4-cianobiphenyl (8CB) flowing in microchannels 30

2.3 SAXS of biological macromolecules 31

2.4 DNA decondensation measurements in bulk 33

2.5 Dynamic changes during DNA decondensation 36

2.6 Summary and outlook 39

3. Formation of actin networks in microfluidic concentration gradients 41

3.1 Introduction 43

3.2 Materials and Methods 44

3.2.1 Microfluidics platform 44

3.2.2 Protein solutions 44

3.2.3 Microscopy and image analysis 45

3.2.4 Simulations 46

3.3 Results and Discussions 47

3.3.1 Microfluidic device for flow-free, steady state linear gradients 47

3.3.2 Actin polymerization in KCl gradients 49

3.3.3 Formation of networks of F-actin bundles in Mg^{2+} gradients 51

3.3.4 Gradient formation across sequential microchambers 56

3.4 Conclusions 60

4. Direct observation of alternating stretch-coil and coil-stretch transitions of semiflexible polymers in microstructured flow 63

4.1 Introduction 65

4.2 Materials and Methods 66

4.2.1 Actin filament solution 66

4.2.2 Microfluidcs platform 66

4.2.3 Microscopy and image analysis 67

4.2.4 Computational fluid dynamics (CFD) simulations 68

4.3 Results and Discussion 69

4.3.1 Design of microstructured flow 69

4.3.2 Center-of-mass velocity, end-to-end distance and bending energy . 71

4.3.3 Bending energies calculated from xy-projections vs. obtained from 3D coordinates 78

4.4 Conclusions 80

5. Live cell X-ray imaging of autophagic vacuoles formation and chromatin dynamics in fission yeast 84

5.1 Introduction 86

5.2 Results and Discussion 87
5.2.1 X-ray induced autophagy in fission yeast cells 89
5.2.2 X-ray imaging of the chromosome motion 91
5.3 Conclusions 94
5.4 Materials and Methods 95

6. Conclusions and outlook 100

References 103

Publications 118

Acknowledgements 119

Curriculum Vitae 120

Chapter 1

Introduction

In living organisms, most of biological reactions and mechanisms are governed by macromolecules and complex macromolecular assemblies at nanometer and micrometer scales. It is very desirable to visualize and analyze the dynamical changes of biological processes including physical properties of the living cell *in situ*. Due to the fact that the functions in living organisms are very complex, it is important at the first stage of a study to simplify the environment and perform the experiments *in vitro*. For this purpose, specially designed microfluidic devices can be developed that would fit to the various requirements of the experiment such as spatially and temporal control of the reaction components and stimuli. These microfluidic devices are especially suitable for the studies of the biofilaments. Moreover, solutions containing biofilaments are considered as non-Newtonian fluids and have typical properties such as viscosity changes with fluid's velocity, stress or pressure change[1].

1.1 Dynamics of biomacromolecules

There are four major types of macromolecules essential for all known forms of life: proteins, lipids, carbohydrates (polysaccharides), and nucleic acids. Living eukaryotic cells can be characterized as dynamic structures displaying continued physical rearrangement and adjustment in shape, appearances,

location, and interactions with extracellular structures including other cells. The cytoskeletal meshwork mainly consists of filamentous actin (F-actin) microtubules and intermediate filaments (**Figure 1.1**). These biopolymers together with hundreds of proteins form bundles as well as networks and provide the structure and viscoelastic properties of cells.

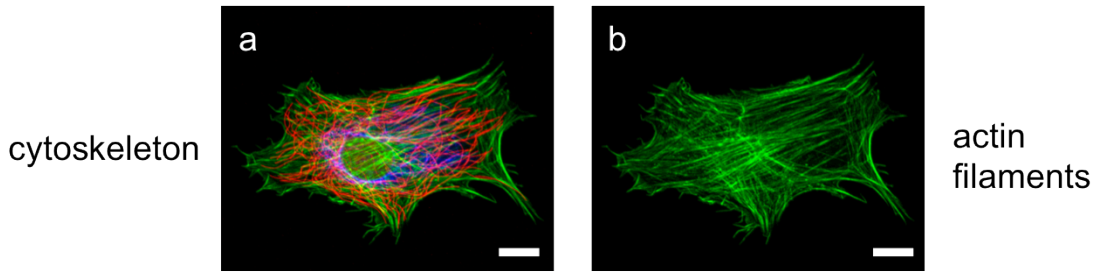

Figure 1.1: Fluorescence micrographs of the cytoskeleton visualized in a Rat2sm9 fibroblast. (a) Cytoskeleton of three kinds of biopolymers, where actin filaments are labeled in green, vimentin (intermediate) networks in blue and microtubules in red. (b) Only actin filaments. Scale bars correspond to 10 µm. Images are taken from R. Suetterlin and C.-A. Schoenenberger, University of Basel.

Physical functions are provided by frequent changes in macromolecular assemblies, signal inputs and metabolic flux, including cytoskeletal scaffold structures of actin microfilaments, which undergo dynamic changes in both polymerization and their interactions with specific binding proteins. Actin is a highly conserved, globular, cytoskeletal protein and is the major protein in almost every type of eukaryotic cell that has been examined[2]. It is a critical player in many cellular functions such as cell division, cell motility and the formation and maintenance of specialized structures in differentiated cells, which are regulated by the dynamics of the actin cytoskeleton[3]. Actin monomers consist of approximately 375 amino acids with a molecular weight of about 42 kD forming a folded single polypeptide chain[4]. The ability of actin to change between monomeric (G-actin) and filamentous (F-actin) is controlled by nucleotide hydrolysis and is dependent on local intracellular concentrations of ATP-bound monomeric globular actin (G-actin) and a large number of actin-binding proteins, which determine the rate and direction of the polymerization as well as the shape of the newly generated filament[5]. Polymerized actin (F-actin) consists of two chains that turn gradually around each other forming a right-handed, long helix composed of globular subunits

(G-actin) approximately 8 nm in diameter[2]. Fluorescently labeled polymerized actin in microfluidic chambers and in a living cell is shown in **Figure 1.2**. Actin polymerization is a reversible process, which can be initiated *in vitro* by the addition of salt (e.g. Mg^{2+}, K^{+}) in presence of adenosine triphosphate (ATP) to a G-actin solution and can occur, when the concentration of unassembled actin subunits is above a critical concentration of G-actin, which is e.g. 0.1 µM in 100 mM KCl[6].

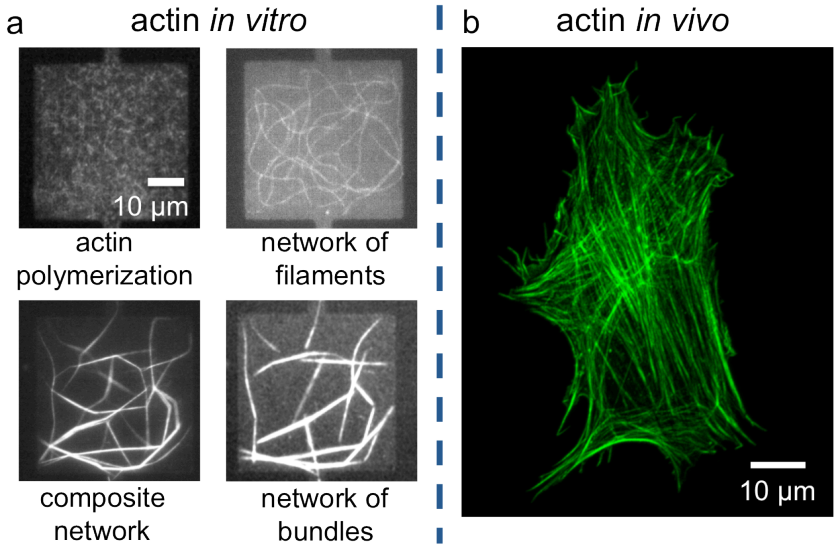

Figure 1.2: (a) Polymorphism of actin in microfluidic chambers: polymerization of actin monomers, formation of filaments and bundles. (b) Fluorescence micrograph of an actin network in a Rat2sm9 fibroblast. Image (b) is taken from R. Suetterlin and C.-A. Schoenenberger, University of Basel.

Monomers join in the (ATP)-bound state and form polar filaments with two filament ends, which are non-equivalent due to different polymerization properties. Actin monomers in the ATP state join the faster growing (+) end of the filament, whereas ADP-actin monomers faster dissociate from the ( ) end. Inside the cell, F-actin can be found in different structures such as lamellae, phagocytic cups and pits, circular dorsal ruffles[7], finger-like protrusive structures, adhesion structures, blebs, podosomes[8], and stress fibers[9]. Dynamic rearrangements of actin filaments generate intracellular counter-forces needed for motility functions, cell migration, spreading, adhesion, contraction and polarization, cell cell contacts and cell extracellular matrix interactions.[5] The persistence length of an actin filament is about 10-13 µm and

the highly regulated contour length is in the range of 1-100 μm[10]. F-actin is a well-studied model for semiflexible biopolymers[11,12].

Another major type of macromolecules is deoxyribonucleic acid (DNA). Double-stranded DNA is also a well-known semiflexible biopolymer with a persistence length of about 30-100 nm and a diameter of around 2.0 nm[13]. It is composed of repeating units called nucleotides made of three components: the sugar deoxyribose, the phosphate group, and a nitrogenous base. DNA is a macromolecule for information storage that carries the genetic instructions (the genome), which are required for the development, functioning and reproduction of all known living organisms and most viruses[14]. The idea of the DNA studies in this thesis is sketched in **Figure 1.3**: *in vitro* by using artificial gene carriers and *in vivo* performed in the living cell.

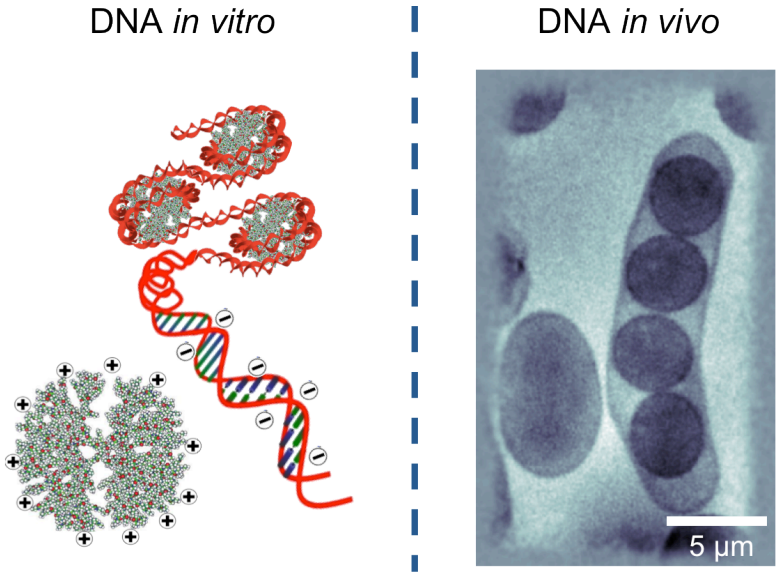

Figure 1.3: DNA electrostatic interactions with cationic nanospheres and DNA in living fission yeast cell spores visualized by applying the ptychographic X-ray imaging technique.

The dynamics of DNA has generated considerable interest over time[15,16]. Large DNA molecules in solution behave as random coils and small molecules as rods, whereas in chromatin and virus particles, DNA is folded into compact assemblies[13]. In the cell, the dynamic rearrangements of the DNA play a key role in many fundamental processes, including DNA folding into chromosomes, which is essential for gene packing and protection. DNA unwrapping from histone proteins is needed for DNA replication,

transcription, repair and recombination to occur, because it must be accessible for DNA-binding proteins[17]. During transcription new proteins can be produced[18], whereas during replication new DNA chains are created. Very fascinating dynamics occur during meiotic cell division in fission yeast, when chromosomes are oscillating from one cell end to another. This motion leads to alignment and exchange of genetic material between homologous chromosomes that results in recombinant genes; this phase is called synapsis[19].

Biopolymers are responsible for most of the cell's functions and their physical properties are very challenging to investigate *in vivo*[20]. Therefore, scientists developed different methods to model the cellular mechanics with purified, reconstituted *in vitro* systems[21].

1.2 Out of equilibrium experiments

Biological organisms are continuously facing complex and uncertain environments. This complexity is caused by the fact that even the most basic and seemingly simple interactions can lead to quit complicated non-equilibrium dynamics. Non-equilibrium systems are continuously energy-driven systems and therefore also flows have non-equilibrium behavior.

1.2.1 Microfluidics

Microfluidics is an ideal technology for non-equilibrium experiments. It is a rapidly evolving multidisciplinary research field, which deals with the geometrically constrained flows of fluids at submillimeter-sized scale[22]. Scaling down standard laboratory setups by a factor of 1'000'000 or more, microfluidic systems work with nL or pL amounts of fluids. Such a dramatic reduction in volume of required samples noticeably reduces the reaction time, pollution, lowers costs, enables efficient experiment observations and manipulations[22]. Potentially, a system of procedures can be integrated in microfluidic devices that commonly might require a whole lab. Applying microfluidics the new possibilities such as precise dynamic control over concentrations of molecules in space and time become available. Thus it might become a promising

method in the analysis and synthesis in the future. The physical properties of microfluidics are characterized by almost no inertia, almost no gravity, laminar flow, and a low Reynolds number (Re). The Reynolds number characterizes the ratio between inertial and viscous forces acting on fluids[23]. The dimensionless Péclet number (Pe), which is important in many microfluidic applications, represents the ratio between convective transport and diffusive transport[23]. An advantage of microfluidics is the absence of turbulence due to laminar flow. On the macroscopic scale, fluids mix convectively, since inertia is more dominating than viscosity, whereas in microsystems fluids do not mix convectively. Thus, when two solutions streams come together in a microchannel, they flow parallel to each other and the only mixing that happens is due to the diffusion of molecules through the interface between the fluid streams[24]. Therefore, as shown in **Figure 1.4** (a), the highly defined laminar flow along the gray outlet channels of this specific microfluidic device create a stable concentration gradient due to diffusive mixing in the pink adjacent microchambers. Thus, each position along the microchambers contains a different concentration of the reactants. Consequently, non-equilibrium structure formation such as actin polymerization in a concentration gradient can be studied.

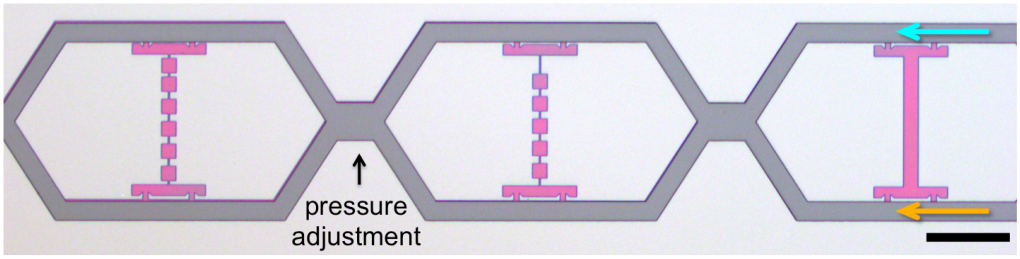

Figure 1.4: Bright field image of the multi-height microfluidic device master with flow-free microchambers prepared using photolithography. The flow channels are visible in dark gray and microchambers with bypasses in pink. For non-equilibrium, steady-state gradient experiments, one flow channel is used as the source of the substance and the other as the sink. Pressure adjustment points between the main channels reduce possible cross-flow in micro-chamber. Scale bar: 200 µm.

In this manner, a variety of different compound and mixture environments can be created easily. Thus, microfluidic devices can be designed to ensure a non-equilibrium rise and a drop of reactant concentrations. Changing the flow

velocities and the observation positions in the device, reactions can be studied at different states under controllable conditions. Microfluidic devices can be produced using standard soft lithography techniques[25]. Moreover, based on soft-lithography procedures, essential methods were developed to fabricate structures that serve as valves[26,27], mixers[28 30] and pumps[31]. For example, a device, which enables fast and efficient mixing of fluids with chevron/herringbone micromixer demonstrated in ref.[32], was successfully used for the production of monodisperse, unilamellar liposomes with excellent gold nanoparticles encapsulation efficiency[30]. Furthermore, the used biocompatible materials, polydimethylsiloxane (PDMS) and glass (**Figure 1.5**), makes microfluidics an excellent tool for life sciences to discover biological systems including bacteria, living cells and whole tissues.

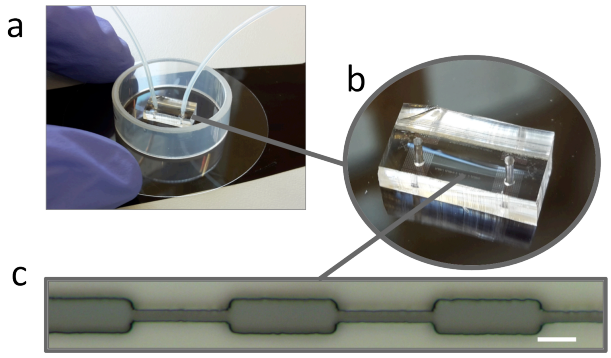

Figure 1.5: Microfluidic device made of PDMS and a glass slide. (a) A PDMS replica bound to a glass slide with a plastic ring to keep the device in water and to achieve water equilibration. Tubing is connected to the inlet and outlet of the device. (b) PDMS replica with punched holes covalently bound to a glass slide. (c) Example of a possible design of a microdevice. Scale bar: 10 µm.

Different microfluidic device architectures create specific environments and open a huge area of possible analyses, e.g., for single macromolecules studies such as DNA[33], actin[34 36] or individual cells[37,38] and bacteria[39,40]. Furthermore, industrially applicable microdevices with high-throughput and easy-to-build architectures for mass production represent one of the major subjects of future investigations[41].

1.2.2 The combination of microfluidics and small angle X-ray scattering (SAXS)

The most common techniques used for the detection in microfluidics experiments are bright field microscopy, fluorescence microscopy and spectro-microscopy however, the combinations of microfluidics and X-ray scattering systems recently became feasible[37,42,43]. Small angle X-ray scattering (SAXS) is an analytical technique that provides information about the average particle size, shape and organization in a sample[44]. Due to the high penetration depths and short wavelengths, X-rays have an advantage over several other analytical techniques. It provides the possibility to analyze label free, thick and unsanctioned samples with nanoscale resolution[45], making it an attractive tool for biological sample measurements. However, X-ray ionizing radiation may cause serious damage and even kill living samples. Therefore, continuous flow in microdevices enables constant sample exchange by avoiding long exposures[33] or in case of single cell measurements[37], flushing away free initiated radicals by constant fresh buffer supply. Consequently, the combination of SAXS and microfluidics provides wider opportunities to study biopolymers and living organisms, such as cells and bacteria. The most popular and well-established materials for microfluidic device fabrication are glass and PDMS, which are compatible with various optical detection methods. However, for X-ray measurements standard PDMS devices are not suitable due to a high X-ray absorption and a strong background signal. Thus, in order to obtain enough signal from the small volume of the sample, background scattering must be reduced. Therefore, the materials must be compatible with X-ray scattering techniques and meet the requirements of microfluidics such as stability, flexibility in channel architecture and dimensions, low-cost, fast in manufacturing, and ease in handling. For this purpose, microfluidic devices based on different materials have been proposed as reviewed by Köster and Pfohl[37]. One example is a device built of thin polyimide (Kapton) windows and a thin film of a PDMS to define the channel structure[46]. Kapton is a useful material for SAXS, as it is resistant to strong X-ray beams and has low X-ray absorption, which enables high quality SAXS experiments. Additionally, Kapton is biocompatible, inert to a series of solvents, and has an excellent chemical and thermal stability. Other channel

defining materials between Kapton films have been used, such as stainless steel plates[47] and UV-curable Norland Optical Adhesive 81 (NOA 81)[48]. Other often used X-ray compatible materials are cyclic olefin copolymers[49–51] and polystyrene foils[52,53], which can be used instead of Kapton. Microfluidic devices made of Kapton or polystyrene foils with NOA 81 are shown in **Figure 1.6**.

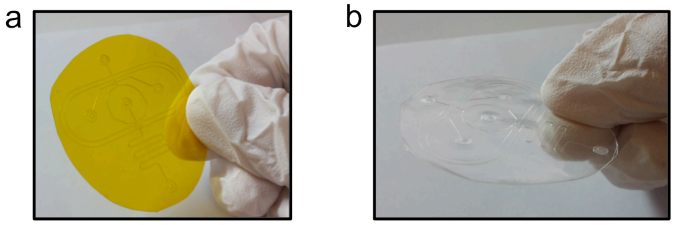

Figure 1.6: X-ray compatible sandwich-like microfluidic devices made of (a) Kapton-NOA-Kapton or (b) polystyrene-NOA-polystyrene.

Various soft and complex materials, such as DNA[33,54,55], proteins[43,52,56], micelles[57–59], liquid crystals[46,49], droplets[60] and the formation of nanoparticles[61], have been successfully studied in microfluidic devices using SAXS. Thus, this combination of techniques is appropriate for non-equilibrium dynamic studies of biopolymers.

1.3 *In vitro* studies of actin and DNA dynamics

Living organisms are systems of very complex dynamics that are made of a countless number of different molecules and compounds, which continuously interact with each other and with their surrounding. This complexity makes it difficult to explore basic biological functions *in vivo*. Therefore, it is essential to simplify the complex processes of living beings in order to make a straightforward, more detailed and more convenient analysis; for example, *in vitro* studies, which are performed on biomolecules isolated from their natural biological surrounding. Traditionally, *in vitro* studies are done in artificial culture media and buffer solutions using flasks, tubes or Petri dishes. However, a more advanced and beneficial technique is microfluidics, where microdevice geometries enable, for example, producing microchannels with alternating high- and low-velocity segments or creating a chemical gradient in

microchambers. Multi-height devices based on the idea of diffusion-advection chamber microfluidics[62] enable creating flow-free, steady state concentration gradients (**Figure 1.4**). These gradients reflect the significance of the heterogeneity of cellular microenvironments and can be applied for cytoskeletal functionality studies. In particular, the formation and structural properties of fluorescently labeled actin networks by analyzing the effects of spatial conditions, bending rigidities of network links, and the network elasticity were studied. An example of bundled F-actin networks formation in step-like gradient is as shown in **Figure 1.7**.

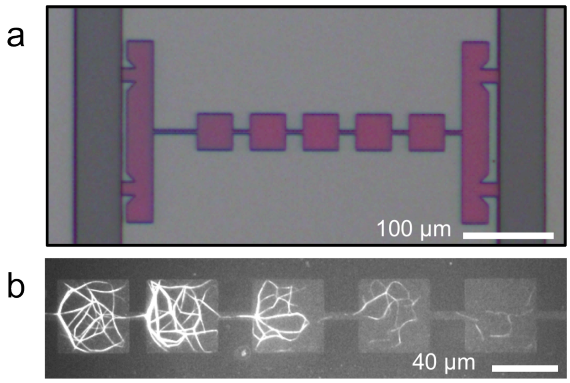

Figure 1.7: Multi-height microfluidic device with flow-free microchambers for non-equilibrium, steady-state, step-like gradient experiments. (a) Bright field image of the device with flow channels in dark gray and microchambers with bypasses in pink (b) Fluorescence microscopy image of bundled F-actin networks formation in a double gradient of KCl and Mg^{2+} using the left flow channel as the source and the right one as the sink.

There are alternative gradient generating microfluidic platforms such as transient[63] and steady state[64], where an interference of flow with the assembly process is mainly excluded, which is important for the formation of soft matter assemblies and networks. As discussed above, actin polymerization *in vitro* is initiated by adding KCl to a buffered solution of monomeric actin. Using a KCl solution as the concentration source and a solution without KCl as the sink, a F-actin gradient establishes across the microchamber. Moreover, using the same gradient generation principle by adding Mg^{2+} to the KCl solution, the formation of F-actin bundles in Mg^{2+} gradients can be initiated. The principle of microfluidic gradients can be applied to study the variety of different macromolecular interactions. Moreover, in the combination with different

detection techniques properties of the microfluidic devices can be also extended.

Another important step towards a better understanding of complex semiflexible biopolymer dynamics is to study their behavior under hydrodynamic forces in microchannels with constrictions. Flowing actin filaments entering wider channel segments undergo a buckling transition, whereas entering narrow constrictions a transition from a coiled to a stretched conformation of the filaments can be observed. Examples of stretch-coil and coil-stretch transitions of individual actin filaments in structured microchannels with different channel width ratios are shown in **Figure 1.8**.

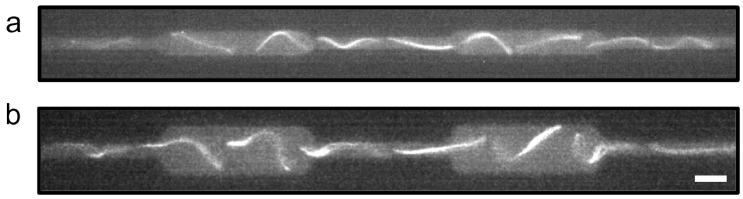

Figure 1.8: Overlay of fluorescence image sequences of F-actin flowing through microchannels with constrictions. (a) Channel width ratio 1:2 and (b) 1:4. Scale bar: 5 µm.

The nature of these non-equilibrium conformational transitions strongly depends on the flow velocity, actin filament length as well as the width ratio between the wide and narrow parts of the channel. Furthermore, a detailed understanding of these dynamic processes shed light on non-Newtonian flow behavior[65] and pattern formation processes in cytoplasmic streaming[66].

Other dynamic biopolymer transitions that we have studied were reversible compaction and decompaction of DNA, which play a significant role for cellular mechanisms. *In vivo* DNA condensation occurs by interaction with histone and is the process of packing and protection of the genetic information, whereas DNA decondensation is catalyzed by enzymes and is related to transcription, replication and repair[67]. It is possible to imitate these interactions using cationic dendrimers, which mimic the physical properties of histone proteins, such as size and charge density. The most suitable dendrimer for this purpose is the biocompatible polyamidoamine of generation 6, known as PAMAM G6. This dendrimer was investigated for drug delivery, gene expression, and gene therapy[68]. To study the nanostructural

evolution of the DNA / PAMAM G6 complex formation and DNA decondenstation from PAMAM G6 we applied SAXS, which is one of the most suitable techniques for quantitative characterization of macromolecules at their different conformational states[69]. Moreover, the dynamic changes of the evolution of DNA and PAMAM interactions were performed in the combination of microfluidics and SAXS. A X-ray compatible hydrodynamic focusing microfluidic device with chevron/herringbone structure, focuses the stream from the sides as well as from the top and bottom[32,70]. The principle of time-resolved reaction measurements using SAXS is shown in **Figure 1.9a,b**. Measuring the scattering signal at different channel positions provides information about the temporal evolution of the reaction, which allows for a detailed understanding of the dynamics of DNA and dendrimer interactions.

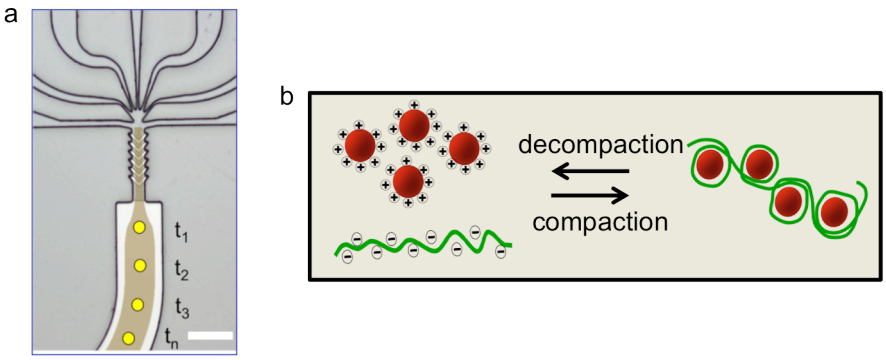

Figure 1.9: The schematic representation of the DNA compaction and decompaction in a microfluidic device. (a) Microfluidic device for time-resolved measurements of the reaction *in situ*. (b) Schematic representation of the DNA charge induced electrostatic interactions with cationic dendrimers and a beads-on-a-string structure formation. Scale bar: 300 µm.

1.4 Lensless X-ray imaging

Imaging without lenses records diffraction patterns of an object, which is illuminated by a coherent light source. Thus, it is a coherent diffractive imaging (CDI) technique. Diffracted waves can be X-rays, electrons or photons, but the waves must have a constant phase difference and the same frequency. In diffraction measurements, only the intensity is recorded and the main issue is the retrieval of the phase information from a recorded diffraction pattern[71]. The missing phase can be numerically reconstructed by iterative

phase retrieval algorithms[72]. These algorithms vary between real and reciprocal space imposing boundary constraints[73]. The resolution in X-ray microscopy is limited due to the difficulties in developing high-quality nanostructured X-ray optical elements. In contrast, lensless X-ray imaging is only resolution limited by the wavelength, radiation damage, the collected solid angle, and the number of collected X-rays. This capability provides a valuable tool for discovering cellular biology at the nanoscale.

1.4.1 X-ray Ptychography

Ptychography is a coherent diffractive imaging technique, where numerous diffraction patterns of the object are collected during the measurement. These patterns are measured at different, but overlapping regions of the specimen. During the measurement, the sample is moved laterally across the illumination beam. Ptychography combines scanning microscopy with iterative reconstruction algorithms. Thus, a single projection image of the specimen consists of all recorded diffraction patterns.

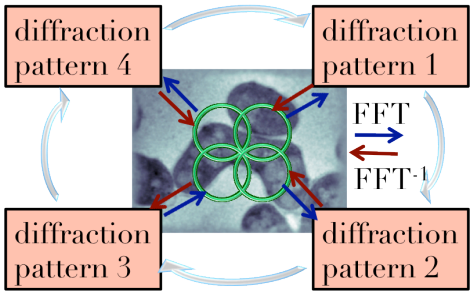

Figure 1.10: Schematic representation of the iterative phase-retrieval algorithm for X-ray ptychography data reconstruction. The blue and red arrows indicate the iterative algorithms, which transform and update the functions back and forth between the real and Fourier space that link the diffraction patterns with the object. The circular arrows show that the redundancy in data is used to update the object functions in the real space. The green circles show the overlapping scanning positions of the specimen.

The major challenge of X-ray imaging of living cells is the very low lethal radiation dose. For a proper X-ray image, the samples have to be exposed long enough for a good contrast and at the same time not exceed the tolerable radiation dose of the specimen. In previous studies, the applied radiation

doses were much higher than the lethal dose for the cells[74,75]. This problem can be circumvented by chemical or cryo-fixation of the sample, which reduces radiation-induced degradation[76,77]. This allows for using higher radiation doses and improves image quality. However, fixation of the sample itself stops cells function and basically kills it. Therefore, in order to discover the dynamics of the cell *in situ,* it is essential to analyze a living sample. One of the most crucial steps in successful X-ray imaging of living cells is a suitable sample preparation method. We have developed and optimized a technique, which is straightforward and efficient in use. For the X-ray windows of the sample, we used silicon nitride (Si_3N_4) membrane windows (**Figure 1.11**), which consist of a frame ($5 \times 5\ mm^2 \times 200\ \mu m$) and a membrane ($1.5 \times 1.5\ mm^2 \times 200\ nm$). The silicon nitride membrane was coated with lectin to increase cell adhesion on the membrane surface. This step is essential to avoid sample motion in the buffer solution. Any unrequired motion of the sample during X-ray imaging, leads to the resolution depredation, which was discussed by M. Bartels *et al.* in more detail[78]. In the next step, a small drop of fission yeast cells in nutrition deficient Edinburgh minimal medium (EMM-N) was placed on the Si_3N_4 membrane. Here, no fixation steps are required, which makes the sample production even easier. Finally, the device was covered by an uncoated Si_3N_4 membrane window and glued at the edges.

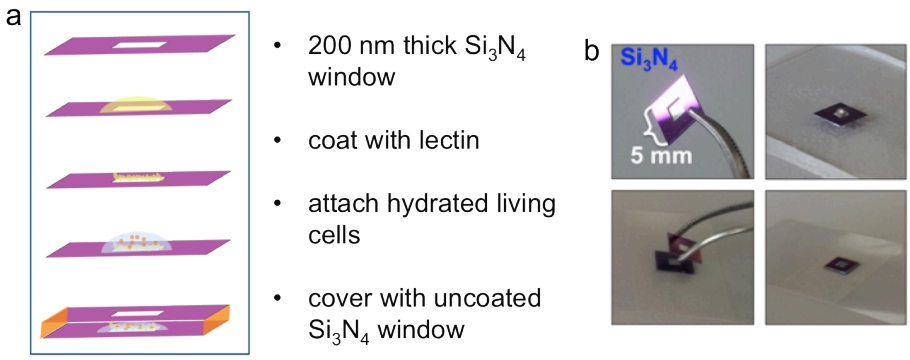

Figure 1.11: (a) Schematic representation of the sample preparation for X-ray measurements of living cells. (b) Images of the sample preparation using Si_3N_4 membrane windows.

With this preparation method, the achieved hydrated sample thickness is about 5 to 10 µm, which is beneficial for X-ray measurements, because aqueous environments significantly decrease the electron density contrast. For

thicker samples, higher X-ray fluxes are required, which consequently increase the radiation dose and damages the living cells. In fact, here we meet both requirements: reduced background noise and favorable environment for living cells. X-ray ptychography owes its success as an effective tool to observe the dynamic changes of unstained living specimens in natural, aqueous environments at nanoscale resolution.

1.5 *In vivo* studies of dynamical changes of living cells

In this work, the studies performed in the context of intact organisms or so-called *in vivo* studies were done on fission yeast, *Schizosaccharomyces* pombe cells. We discovered the dynamical changes of chromosome oscillations during the meiotic division[79 81]. Meiosis is a fundamental process in all eukaryotes, leading to genetic diversity, but the details of this process and the mechanism of homologous chromosome recombination are still poorly understood. A schematic representation of meiosis in fission yeast is shown in **Figure 1.12**.

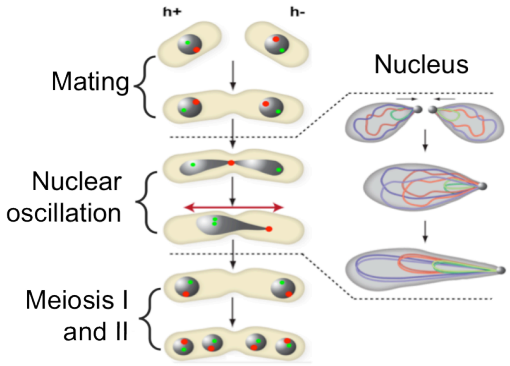

Figure 1.12: Schematic representation of meiosis stages: mating, kariogamy and nuclear oscillation, meiosis I and II. Red dots mark the positions of the spindle pole bodies (SPBs) and green dots indicate fluorescently labeled homologous loci. In the left panel, the merger of nuclei and arrangement of the three chromosomes into bouquet configuration are shown. Image taken and modified from M. Chacón Rodríguez and P. Delivani, Max-Planck-Institute of Molecular Cell Biology and Genetics, Dresden.

Fission yeast is an ideal model organism, because it is a eukaryotic cell and many of basic cellular principles and cell regulators are conserved from yeast to humans[82]. Moreover, it has only three pairs of chromosomes, whereas human cells have 23 pairs of chromosomes. One of the basic questions is how the chromosomes are aligned for proper recombination. Since errors in the recombination and chromosome segregation for the offspring can be fatal, the process must happen with exceptional precision. Oscillatory nuclear movements in fission yeast occur during the so-called horsetail stage[83]. Bright field and fluorescence microscopy images of three *S. pombe* living cells, with two "banana" shape meiotic cells and one non-meiotic cell, are shown in **Figure 1.13**. The fluorescence microscopy images show that one of the zygotes is at the horsetail stage. Thus, using bright field microscope zygotes and non-zygotic cells can be easily recognized, whereas oscillating and non-oscillating zygotes are not distinguishable.

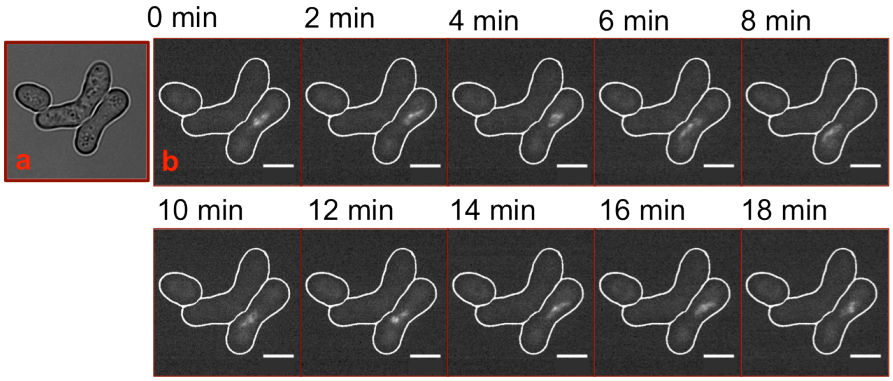

Figure 1.13: Nuclear oscillations during meiotic prophase of *S. pombe*. (a) Visible light bright-field microscopy image of living fission yeast cells. (b) Fluorescence microscopy images of the same cells with a time interval of 2 min. The rec25 gene was labeled with green fluorescent protein and used as an indirect marker of DNA double strand breaks[84]. Only one zygote is at the horsetail stage.

The oscillating, fluorescently labeled chromosomes can be seen as a bright spot, which is oscillating from one cell end to the other. Back and forth motion along the cell axis can emerge for several hours followed by the first and second meiotic divisions[79]. Studies using fluorescent labeling do not give direct information about the structure and additionally might cause the formation of artifacts. Therefore, we employed X-ray ptychography to directly explore the dynamics of unstained living fission yeast. X-ray ptychography

visualizes the densification of chromosomes, motion and shape transformations during the horsetail stage in natural, aqueous environment at high resolution. Moreover, due to the contrast sensitivity it is possible to reduce the X-ray radiation dose and make several X-ray ptychography images of individual living cells, which allows for examining the dynamics of nuclear oscillations. Furthermore, when exposed to a higher amount of X-rays, rounded bodies appear in the (**Figure 1.14**). These bodies show a similarity to vacuoles and autophagic bodies[85]. A bursting of the cell membrane and shrinkage of the cell follow the formation of autophagic bodies and after accumulating a certain amount of the ionizing radiation, the cell perishes. Thus autophagic vacuole formation and cell lysis caused by the ionizing X-ray radiation can be analyzed and the critical X-ray doses determined.

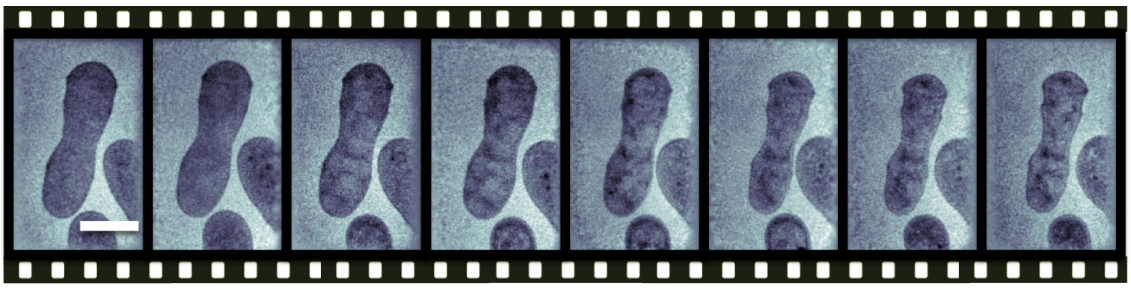

Figure 1.14: Sequence of X-ray ptychography images of a living *S. pombe* zygote. Scale bar: 5 µm.

1.6 Outline of the thesis

The goal of this thesis is to observe and analyze dynamical changes of different biological processes *in situ* by applying microfluidics and detection techniques such as bright field microscopy, fluorescence microscopy, small-angle X-ray scattering and X-ray ptychography. We study the physical properties of actin and DNA as well as the chromosome oscillations and vacuole formation in fission yeast, which are discussed in separate chapters as following:

Chapter 2 covers the reversible DNA condensation and decondensation studies with PAMAM G6 dendrimers using small-angle X-ray scattering. Following the measurements in bulk, we apply the fast mixing microfluidic

device to analyze the dynamic evolution of DNA electrostatic interactions with PAMAM G6 dendrimers. In chapter 3 is presented the actin polymerization, bundling, and network formation in microfluidic-based steady state and flow-free concentration gradients. We analyze the density distribution and the physical properties of the networks of actin filaments and bundles. The alternating stretch-coil and coil-stretch transitions of actin filaments in microstructured flow are presented in chapter 4. We analyze non-equilibrium and non-stationary conformational transitions of individual F-actin under hydrodynamic forces flowing through alternating high- and low-velocity segments. Chapter 5 deals with X-ray ptychographic imaging of living fission yeast cells, where the dynamics of chromosome oscillations and autophagic vacuoles formation caused by ionizing radiation are studied. Additionally, we estimate the average radiation dose at which autophagy occurs and the dose of cell membrane bursting. Finally an overview and conclusions about all projects are presented in chapter 6.

Chapter 2

Dynamic Studies of DNA Using Small-Angle X-ray Scattering

2.1 Electrostatic interactions of DNA

DNA is a biopolymer consisting of a double helix and is essential for all known forms of life. The diameter of the DNA helix is approximately 2 nm, and the vertical rise per base pair is 0.34 nm[86], its persistence length is $\xi_p = 30$ – 100 nm and its contour length can be up to several meters. DNA is a negatively charged polyelectrolyte and positively charged amino acid side chains of proteins or polyamines can neutralize DNA charges[87]. Charge neutralization of DNA is part of the driving force for nucleosome folding and DNA tends to bend toward the neutralized face[88]. In viruses, DNA is compressed in extremely dense bundles with hexagonal symmetry. Small multi-cationic polyamines like spermidine and spermine aggregate along DNA strands reducing the repulsion between DNA segments[89,90]. Different types of DNA compaction are manifested in bacteria[91,92] and eukaryotic cells[18,67] where DNA exists in highly organized states (**Figure 2.1**).

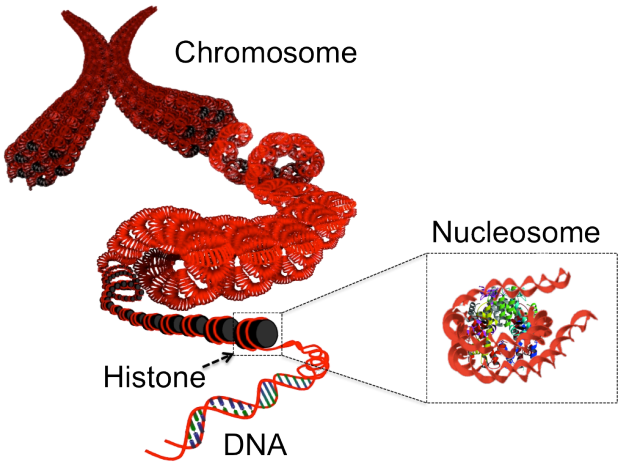

Figure 2.1: DNA packing in the chromosome of eukaryotic cells. Picture taken and modified from Ref. 10[93].

DNA is wrapped in 1.65 turns around the highly basic histone-octamer core, forming repeatable units called nucleosomes, which are connected by a flexible stretch of linker-DNA and build a "beads-on-a-string" structure[94,95]. Nucleosomes are than folded into 30 nm fibers[86] caused by linker-histones binding to the linker-DNA and further fiber coiling forms the chromosome.
In general, electrostatic interactions belong to non-covalent interactions and are crucial in maintaining the three-dimensional structure of large molecules, such as proteins and nucleic acids and are involved in many biological processes when large molecules bind to one another[87]. The interaction of a negatively charged nucleic acid with positively charged ligands causes a perturbation of the electrostatic potential and some of the Manning condensed small counterions are released into the solution with an entropy increase (approximately 1 k_BT per counterion, where k_B- Boltzmann's constant and T- the absolute temperature)[96,97]. The Manning's theory treat nucleic acids as uniform charged lines partially neutralized by binding of counterions, which condense on polyions until the charge density between neighboring monomers is reduced below a certain critical value. In solution, two equal charges can drift appart by a distance l_B (called Bjerrum length) with an energy cost of k_BT:

$$l_B = \frac{e^2}{4\pi\varepsilon_0\varepsilon k_BT} \tag{2.1}$$

where $e = 1.6\times10^{-19}\,\mathrm{C}$ is the charge of an electron, ε_0 is vacuum permittivity and ε is the dielectric constant (ε =80 for water). In contrast, removing a charge from the surface of a protein of radius R costs the energy

$$U = k_B T \frac{l_B 8R^3}{Dr^4} \tag{2.2}$$

where r is the radius of an individual residue[98]. The free energy of DNA binding to the nucleosome is about 0.42 0.63 kJ/mol per base pair (ionic strengths of 50 150 mM)[99]. Moreover, DNA packing and unpacking are reversible and dynamic processes, which are crucial for fundamental cell functions.

The free-energy G of nucleosome formation is:

$$G_{nucleosome} = G_{bend} + G_{DNA-histone}. \tag{2.3}$$

The energy stored in the DNA by virtue of its deformation is:

$$G_{bend} = \frac{\pi \xi_p k_B T}{R_{DNA}}, \tag{2.4}$$

where R_{DNA} is the radius of curvature of wrapped DNA, ξ_p the DNA persistence length $\xi_p = \kappa/k_B T$, where κ is the flexural rigidity of the filament. The interaction between DNA and histone octamer is a favorable electrostatic interaction. This interaction energy can be characterized via an adhesive energy γ_{ad} (units energy/ length) by

$$G_{DNA-histone} = 2\gamma_{ad} L = 4\pi R_{DNA} \gamma_{ad} \tag{2.5}$$

assumig that the DNA is wrapped around the histone octamer about twice[98]. The adhesive energy of DNA-histone is $\gamma_{ad} \approx -0.2\, k_B T/\mathrm{nm} \approx -0.50 \frac{\mathrm{kJ}}{\mathrm{mol\,nm}}$ ($k_B T = 2.5\,\mathrm{kJ/mol}$), where the minus sign indicates that it is a favorable contact[17].

2.1.1 DNA interractions with artificial gene carriers

In eukaryotes, DNA has to be tightly packed up in order to fit into the cell nucleus. Moreover, packing is vital for gene protection and for gene regulation. In order to mimic DNA compaction, artificial gene carriers as a model protein were employed. We used polyamidoamine dendrimers, simply called PAMAM dendrimers as histone replacement (**Figure 2.2**). PAMAM dendrimers are a well-characterized and commercialized class of dendrimers suitable for many materials in science and biotechnology applications[68,100,101].

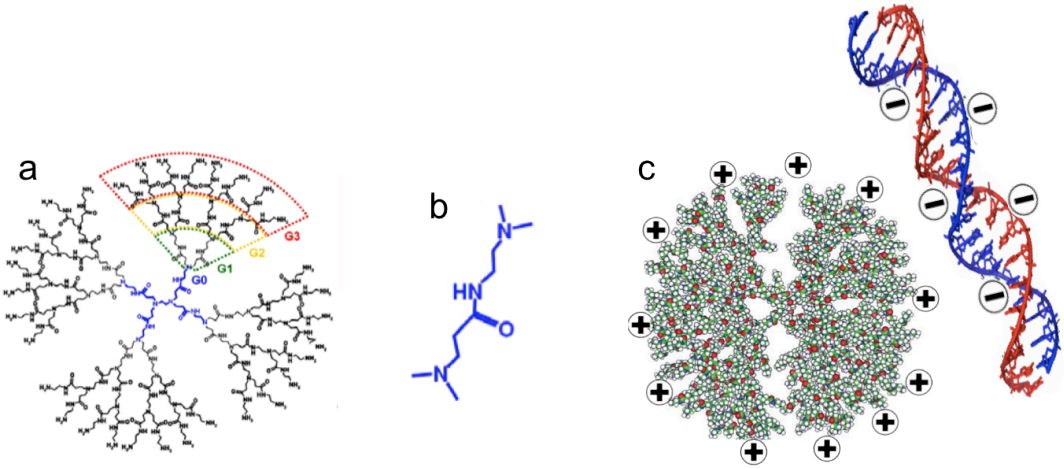

Figure 2.2: (a) Schematic representation of PAMAM dendrimers. (b) Chemical structure of PAMAM repeated subunit. (c) Electrostatic interaction between DNA and PAMAM. Pictures are taken and modified from Ref. [93] and Ref.[102].

PAMAM dendrimers are positively charged, nearly spherical polymers with a highly structural and chemical homogeneity. In particular, they consist of an alkyl-diamine core and tertiary amine branches and are obtainable in generations G 0 - 10 with 5 different core types and 10 functional surface groups. The specific properties of PAMAM dendrimers are the ability to tune their size and charge by changing the generation number and pH of the solvent. At higher pH values (pH > 10), radii of PAMAM dendrimers are smaller than at lower pH, because all amino groups of PAMAM dendrimers are unprotonated and the dendrimer is overall uncharged. At lower pH, amino groups are protonated and due to the increased intra-polymeric Coulomb repulsions, dendrimer branches are further extended[93,103]. This flexibility allows for the control of size, shape and functional groups location, which is

desirable for many life science applications. PAMAM dendrimers are biocompatible and are applied in cancer therapy[104], drug delivery[68,105], gene therapy[101,106 108] and for information storage[68]. In our studies, we used PAMAM of generation 6 (G6), because its size and charge is compatible to a histone core protein. These cationic polymers form complexes with DNA through sequence-independent, electrostatic interaction between negatively charged phosphate groups of the nucleic acid and protonated, positively charged amino groups of the dendrimer. Therefore, PAMAM dendrimers can be used as DNA compaction agents.

2.1.2 DNA compaction at different pH

The dynamic changes of DNA packing and unpacking are important for understanding fundamental cell functions. Condensation of the DNA by polycations is dependent on several factors including charge density, the nature of the ionic groups, molecular weight of macromolecules and the buffer properties. Different conformations of PAMAM G6 and DNA entities as well as the complex structures depending on the pH controlled dendrimer surface charge density are shown in **Figure 2.3**.

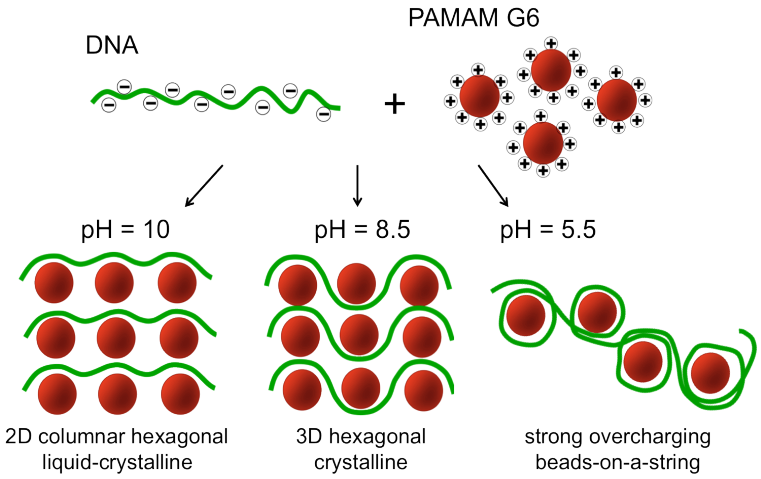

Figure 2.3: DNA and PAMAM G6 condensation at different buffer pH.

At pH = 5.5 a beads-on-a-string structure is formed, which is similar to a DNA wrapped around the histone protein. At pH = 8.5 DNA and PAMAM G6 form

a 3D hexagonal crystalline structure and at pH = 10 2D columnar hexagonal liquid-crystalline structures[93]. Essentially, by changing the pH of the solution, different DNA organization can be achieved. Thus, by regulating the pH, it is possible to tune the interactions of PAMAM G6 and DNA[93].
Furthermore, nucleic acid interactions with positively charged ligands is highly salt-dependent, such that the observed affinity decreases dramatically with increasing salt concentration and results from the polyelectrolyte nature of the linear nucleic acid[109].

2.1.3 DNA decompaction and controlled release

Conformational changes in the nucleosome structure play a key role in DNA metabolism and are generally difficult to resolve. Nucleosomes are DNA histone protein complexes that must be unwrapped for several fundamental enzymatic processes such as transcription, replication and repair[55]. Gene expression starts from transcription and for a gene to be transcribed it must be physically accessible to transcriptional factors, allowing gene expression to occur and proteins to be made. A further reason for DNA unwrapping is cell division where replication of DNA takes place and a copy of DNA is made. Both processes require the two strands of DNA to come apart temporarily, as sketched in **Figure 2.4**.

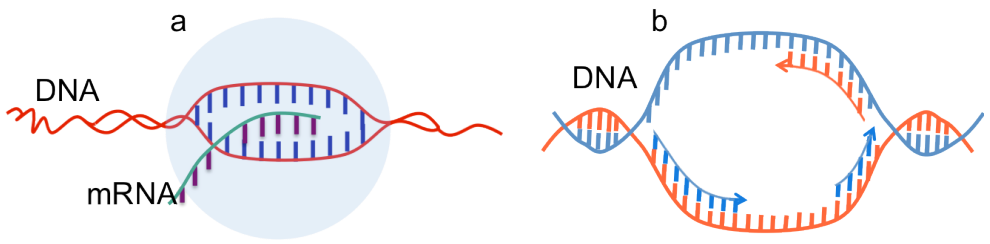

Figure 2.4: Schematic representation of (a) DNA transcription and (b) DNA replication.

DNA unwrapping can be potentially initiated by several factors, such as salt content in the solution, temperature and interactions with enzymes and competitive agents. The most suitable technique to study DNA decondensation as well as condensation is SAXS, because the wavelength of

the X-rays is in the order of magnitude as the size of DNA-dendrimer complexes. The scheme of DNA release from cationic dendrimers is shown in **Figure 2.5.** The DNA/PAMAM G6 complex at pH = 5.5 is a simple DNA compaction model system for bio-mimetic studies of DNA transformations.

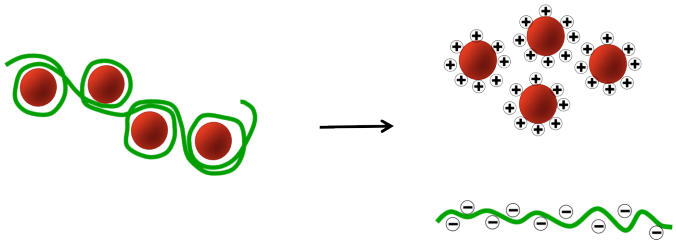

Figure 2.5: Schematic representation of the decompaction of PAMAM G6 and DNA.

2.2 SAXS and Microfluidics

2.2.1 SAXS

SAXS is one of the fundamental tools for the study of biological macromolecules in solutions, which can provide information about partly or completely disordered systems[69]. Investigations of the intermolecular interactions including assembly and conformational changes makes it probably the most suitable technique to study DNA reversible packing mechanisms[55]. SAXS experiments measure electron density distributions within the whole illuminated sample volume and provide information about average molecular sizes, shapes and inter-molecular interferences (over all objects and over all locations of the objects)[43,110]. The Fourier transform[111,112] of the measured electron density does not directly determine the morphology of the sample and two different morphologies can theoretically give identical scattering patterns. Therefore, some information about the shape and size should be known of the analyzed system already in advance[44]. DNA condensation and decondensation were measured using an in-house SAXS setup, which is sketched in **Figure 2.6**. It is built of an X-ray source, 3-pinhole apertures, the sample, a beamstop and the detector.

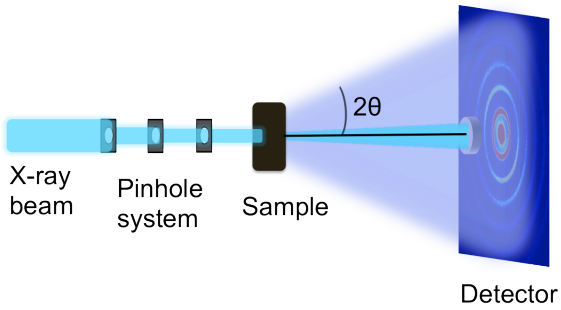

Figure 2.6: Schematic representation of SAXS setup.

An in-house Bruker-AXS Nanostar SAXS setup is equipped with an Incoatec Microfocus source (IμS), generating Cu-K-α radiation with a wavelength of 1.54 Å and intensity up to 10^{10} photons/s/mm^2. For the experiments in microfluidic devices, the X-ray beam size was aligned and adjusted to 150 μm by 3-pinhole system of 500 μm 150 μm 500 μm. The scattering data were recorded using a Bruker AXS Vantec-2000 detector with a 14 cm x 14 cm active area, pixel size of 68 μm and dynamic range of 10^9. All experiments were done at a Voltage of 45 kV and 650 μA (29.25 W) current on the filament and at sample to detector distance of 108 cm. The generated X-ray beam goes through a collimation system in order to control not only the size but also divergence of the beam, and to separate the incoming beam from the undesired parasitic scattered radiation. The beam path is kept under vacuum to avoid scattering from air. After the collimating system the beam hits the sample and the interaction of X-rays with the structure generates secondary waves. The resulting intensity is measured as a function of the angle between the incoming and scattered beams. The larger the scattering angle, the smaller the measured length scale. Small angle X-ray scattering (SAXS), has a scattering angle 2θ close to 0°, whereas wide angle X-ray scattering (WAXS) has $2\theta > 10°$. The combination of SAXS and WAXS allows for investigations of samples with length scales between 0.3 and 100 nm[113]. The angle can be adjusted by changing the distance between the sample and the detector. The obtained scattering patterns are usually characterized by the intensity I of the amplitude of the momentum transfer q, which is also called scattering vector[87]. The scattering vector q is defined by the scattering angle θ and the irradiated wavelength λ according to the following equation:

$$q = \frac{4\pi}{\lambda} \sin\theta. \tag{2.6}$$

The form of the scattering object is obtained from the interference pattern produced by all scattered waves that are detected from every atom/electron inside the object. Moreover, the structural organization of the scattering object can be analyzed, when the sample consists of densely packed and ordered entities, because the interference pattern additionally contains the information from neighboring entities and their position with respect to each other. Therefore, the integrated scattering intensity $I(q)$ consist of the form factor $F(q)$, which characterizes the shape of the entities and of the structure factor $S(q)$, which describes the interference effects between entities

$$I(q) \approx NF(q)S(q)\,, \tag{2.7}$$

where N is the number of entities. On integrated scattering curves at certain q values typical peaks might appear, known as Bragg peaks, and the peak positions determine the symmetry and dimensions of the system, whereas peak heights and shapes are determined by distortions such as lattice/system vibrations, defects, finite-size effects, and others[93]. The dimension of q is one over a length (e.g., [1/nm]). The scattering pattern is the Fourier transform of the real space structure and form. Therefore, using Fourier transformation, the reciprocal space $I(q)$ information can be converted in real space resulting in a $p(r)$ pair distance distribution function. The scattering intensity can be also defined using $p(r) = r^2\gamma(r)$ with the spherically averaged autocorrelation function[69] $\gamma(r) = \langle \int \Delta p(r')\Delta p(r'+r')dr' \rangle$ of intramolecular atomic distances:

$$I(q) = 4\pi \int_0^{Dmax} p(r) \frac{\sin(qr)}{qr} dr. \tag{2.8}$$

The pair distance distribution $p(r)$ can be calculated using the software GNOM developed by Svergun and coworkers[114].

2.2.2 Fast mixing microfluidic device

To analyze the real-time dynamics of the DNA release from artificial gene carriers, we employ soft lithography-based microfluidic reaction devices in combination with a lab source SAXS instrument. The developed microfluidic devices have a multi-height structure and an implemented staggered herringbone micromixer[115]. It was fabricated of two 0.05 mm thick polystyrene foils (GoodFellow, Huntingdon, UK) and NOA 81 (Norland, Cranberry, USA) optical adhesive and placed in a specially designed metal holder (**Figure 2.7**).

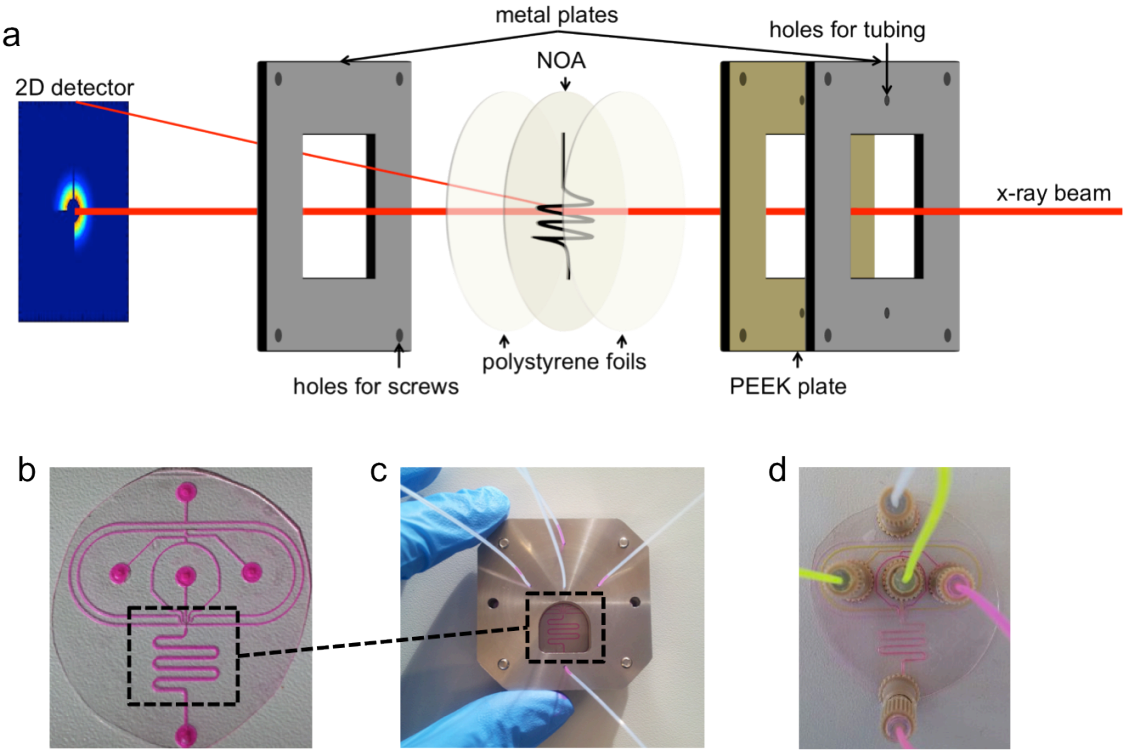

Figure 2.7: (a) Schematic representation of the microfluidic device used for SAXS measurements. Taken and modified from ref.[115]. (b) Micrograph of an X-ray compatible microfluidic device filled with rhodamine solution and (c) a device in precisely designed holder for the Bruker Nanostar SAXS. (d) An alternative way of tubing connections to the device, which can be used for different setups.

Plastic tubings were attached to the inlets and the outlet of the device and connected to microliter syringes. The inlet flows were controlled by syringe pumps. A bright field microscopy image of the microfluidic device is shown in **Figure 2.8a**. The reaction channel is 300 µm wide and has a height of 200 µm.

Seven inlet channels meet at a single staggered chevron/herringbone micromixer, which enables efficient mixing of fluids by repeated stretching and folding of the fluid interfaces[32,70]. The length of the mixer is 468 µm, the width is 80 µm and the height is 40 µm of the main part of the mixer (appears gray in **Figure 2.8a**) and 200 µm at staggered structures (appears white in **Figure 2.8a**). The main advantages of this device are hydrodynamic focusing and fast mixing. Micromixers can be generally classified into passive or active ones. Without external forces, mixing in microfluidic channels happens mainly by diffusion, which is classified as passive mixing. Classical types of passive micromixers are T- and Y-shaped, parallel lamination, sequential, focusing, chaotic advection and droplet micromixers[23]. In order to shorten the mixing time, the diffusion paths between the mixing substreams have to be reduced. Beneficial are multiple parallel streams. The width of the stream and sample volume can be adjusted and controlled by the flow velocities at the different inlets. A hydrodynamic focusing in plane is achieved by the buffer flowing from two lateral channels and additionally a chevron/herringbone micromixer focuses the stream in *z*-direction. Thus, a reaction stream is focused in the center of the device, where the velocity is maximum as well as almost constant and artifacts due to lower flow velocities close to the walls are eliminated (**Figure 2.8b**).

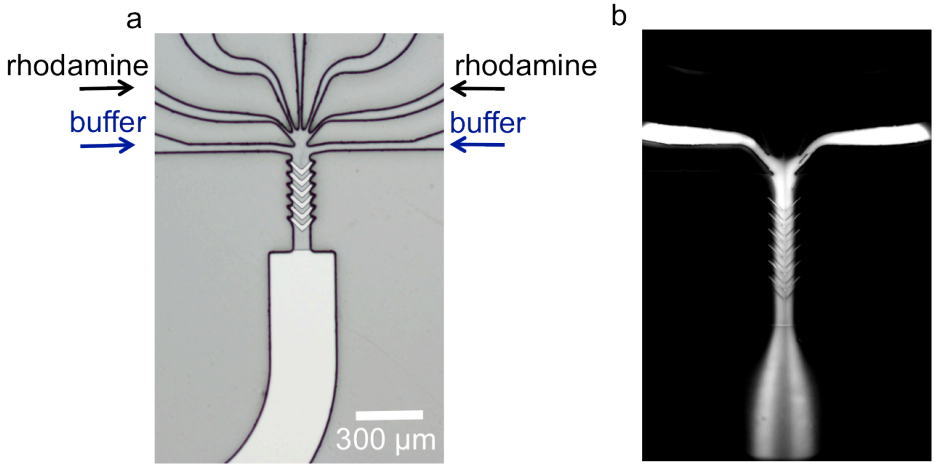

Figure 2.8: (a) Bright field microscopy image of the fast mixing and focusing device. The width of the main channel is 300 µm and height is 200 µm, width of the mixer 80 µm, length is 468 µm and the height is 40 µm (gray part of the channel) and 200 µm (white parts) at staggered structures. (b) Fluorescence microscopy image of the hydrodynamic focusing and mixing in the device.

A fluorescent image of the buffer flowing from the sides and pushing the flow of rhodamine in the middle of the channel is shown in **Figure 2.8b**. Thus, by regulating the velocity of the buffer, it is possible to change the stream width of the dyes. Moreover, scanning the reaction at different positions along the channel allows us to analyze the time evolution of the experiment, because the position of the channel is related to a reaction time. Combining the fast mixing microfluidic hydrodynamic focusing device with SAXS represents a powerful method for biomaterial analysis at nanometer scale.

2.2.3 The liquid crystal *n*-octyl-4-cianobiphenyl (8CB) flowing in microchannels

The combination of SAXS and microfluidics enables the precise control of the reaction measurements in a time-resolved manner[33,43,47]. The microflow device and the SAXS setup were tested using the well-characterized smectic liquid crystal system, *n*-octyl-4-cianobiphenyl (8CB). The ordering of the molecules in liquid crystals categorizes their phase, and in the smectic phase the molecules are aligned and arranged into layers. 8CB is a thermotropic liquid crystal and its molecular organization changes depending on the temperature between smectic A (T_{sm} = 21.5°C) and nematic (T_n = 33.5°C)[116]. At room temperature, 8CB is in a smectic A phase and the distance between consecutive layers is d = 3.17 nm, which can be detected using SAXS. In a plot of the scattering intensity *vs.* the momentum transfer, q appears a peak at q_0 = 0.02 nm^{-1} with $d = 2\pi/q_0$. External stress can change the mesoscale assembly and orientation of 8CB molecules[117,118], which makes it an even more attractive sample for characterization of microfluidic systems with different channel geometries. Depending of the integration of the scattering pattern, different information can be attained. The information of the 8CB lattice spacing is obtained by radially averaging the scattering image over 360° and reflected in a plot of intensity versus q (**Figure 2.9a**). The azimuthal distribution of the peak intensity quantifies the alignment of materials in microflow[119]. The absorption image of the microfluidic device with scattering positions 1 and 2 is shown in **Figure 2.9b**. Intensity distribution versus the azimuthal angle χ for positions 1 and 2 is obtained by azimuthal integration (χ = 0°–360°) along a

fixed radial position q, which shows the orientation of 8CB layers induced by the geometry of the curved channel and the flow direction (**Figure 2.9c**).

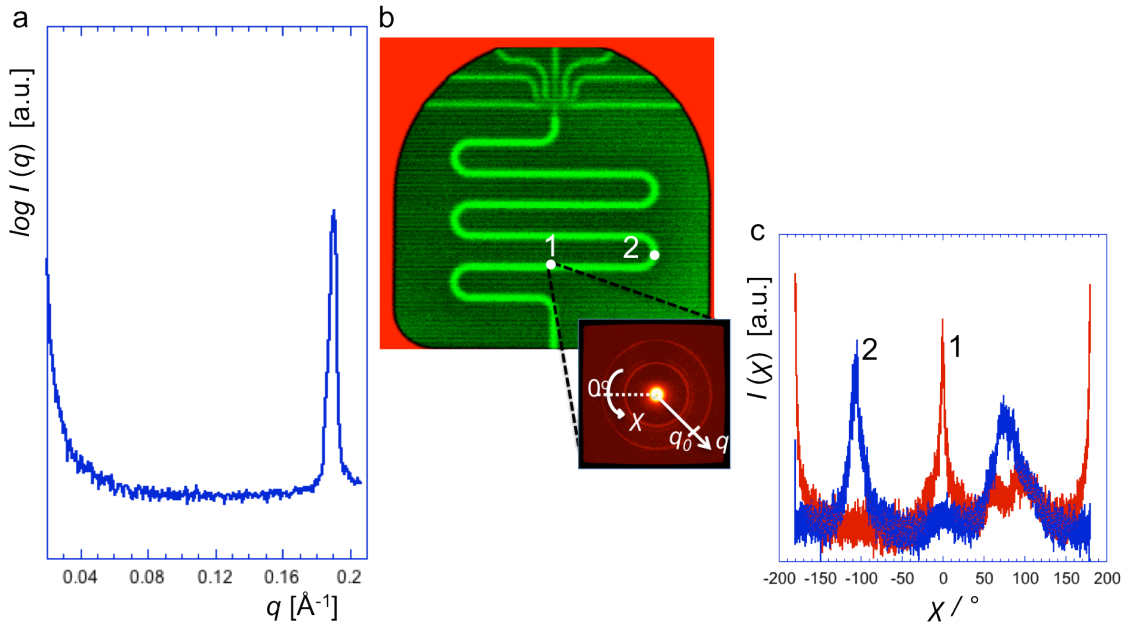

Figure 2.9: (a) SAXS profiles with the scattering intensity I versus momentum transfer q. The peak of the smectic A layer spacing appears at q_0 = 0.198 Å^{-1}. (b) The scanning X-ray absorption image of the microfluidic device with corresponding scattering positions. (c) The azimuthal intensity distribution of 8CB smectic A layers measured at corresponding positions of the channel represented in (b).

2.3 SAXS of biological macromolecules

Although, the scattering of biological systems is weak, obtainable signal to noise ratios can be improved by increasing the concentration of the material or the exposure time. Previous studies have discovered that DNA has a wide range of complex behavior including liquid-crystalline properties and its nature depends strongly on the DNA concentration in the solution[120]. SAXS experiments can measure DNA inter-helix spacing between nearest neighbors, which is dependent on the polymer concentration. For the experiments, lyophilized calf-thymus DNA was purchased from Sigma-Aldrich Chemie GmbH (Taufkirchen, Germany). The DNA was measured in the microfluidic device with the chevron/herringbone micromixer at concentrations from 10 to 50 mg/ml, which correspond to semi-dilute solutions. Using a microfluidic

device reduces the sample volume and in order to collect enough information without destroying the sample under X-ray radiation, it is important to find the optimal concentration and the exposure time for a sufficient signal to noise ratio. Moreover, the viscosity of the DNA due to the concentration has a significant impact on the flow in the microchannels and is an important characteristic of the DNA solutions for microfluidic experiments[33].

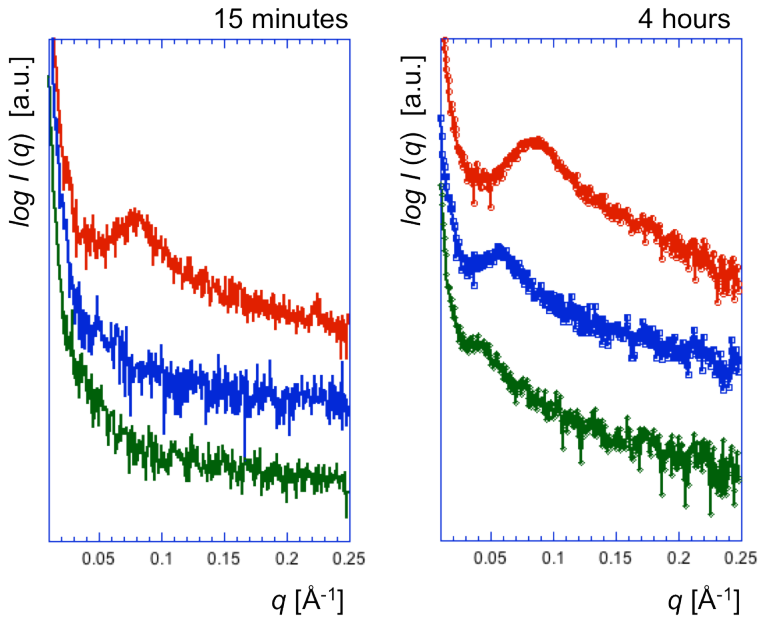

Figure 2.10: (a) SAXS profiles of different DNA concentrations in a microfluidic device, where 10 mg/ml (green), 20 mg/ml (blue) and 50 mg/ml (red) were measured for (a) 15 min and (b) 4 hours. Measurements were background-corrected by subtracting the scattering of the buffer recorded in separate runs. For a better visualization, the scattering curves are shifted by a constant factor.

Logarithmic plots of scattering intensities versus the scattering wave vector obtained from DNA solutions of three different concentrations, which were performed with an exposure time of 15 min and 4 hours, are shown in **Figure 2.10**. The scattering curves show a peak at a certain q_{DNA} position, which arises from the DNA DNA correlation and corresponds to the DNA interaxial distance d_{DNA}[47]. Increasing the DNA concentration in the solution give rise to increased peak intensity and the peaks shift toward higher q values. From the peak position q_{DNA}, the average distance d_{DNA} between molecules in solution can be calculated, using $d_{DNA} = \frac{2\pi}{q_{DNA}}$. Thus, d_{DNA} is 17.9 nm for a

concentration of 10 mg/ml, 10.5 nm for 30 mg/ml and 7.9 nm for 50 mg/ml. The broadening of the peak with the concentration is also dependent of the peak position q_{DNA}[121].

2.4 DNA decondensation measurements in bulk

DNA unwrapping from cationic macromolecules can possibly be initiated by several factors such as change in pH, salt addition to the solution or competitive electrostatic interactions[122,123]. Because DNA is negatively charged, a good potential competitor might be heparin. Heparin is a long unbranched polysaccharide consisting of a repeating disaccharide unit and is highly negatively charged. A possible DNA release from DNA/PAMAM G6 aggregates caused by higher the negative charge of heparin is sketched in **Figure 2.11**.

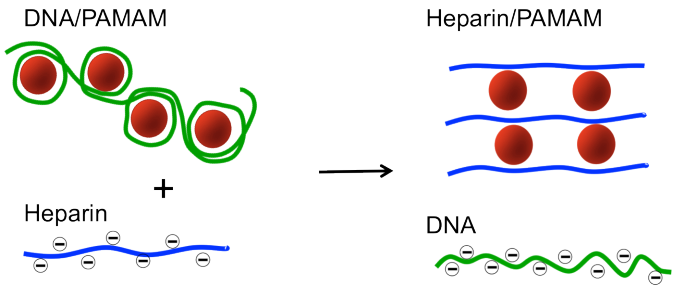

Figure 2.11: Schematic representation of the DNA/PAMAM G6 complex interaction with heparin.

Applying SAXS, we can measure and compare the shape and structures of the DNA/PAMAM G6 complexes and of the PAMAM/heparin complexes. Standard bulk measurements of DNA/PAMAM G6 and PAMAM/heparin were performed in glass capillaries with 1 mm in diameter. The X-ray beam size of 400 µm was adjusted with the pinhole set to 750 µm 400 µm 1000 µm. The scattering of the buffer solution was recorded in separate measurements and subtracted from the data. The integrated scattering data of PAMAM G6/heparin complexes, DNA/PAMAM G6 complexes and PAMAM G6 at pH = 8.5 are shown in **Figure 2.12 a**.

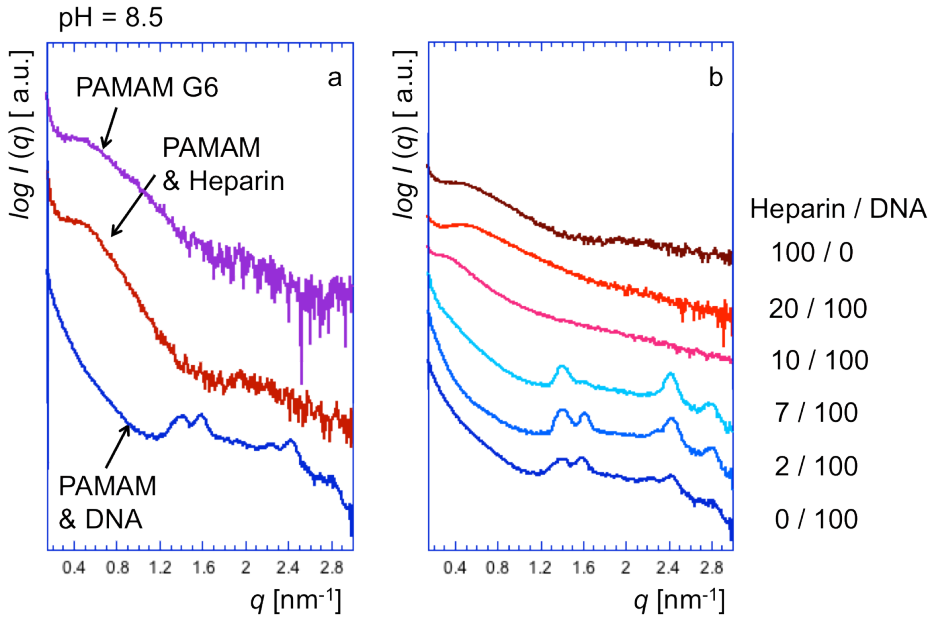

Figure 2.12: (a) SAXS profiles of DNA/PAMAM G6 complexes (blue), PAMAM G6/heparin complexes (red) and PAMAM G6 (violet). (b) Influence of SAXS profiles of heparin on the DNA/PAMAM G6 complex structure with variable heparin/DNA concentration ratio. The curves are shifted by a constant factor for better clarity.

The scattering intensity of DNA/PAMAM G6 complexes, at a relative ratio N/P=1, where N is the number of positively charged amine groups of PAMAM and P is the number of negatively charged phosphate groups in DNA, are presented in **Figure 2.12b**. Here, considering a molecular weight (MW) of one DNA base pair to be 660 g/mol and 2 negative charges $\frac{2}{660} = 3 \cdot 10^{-3}$, the concentration of molar charges can be calculated by $C^{DNA}_{molar\_charge} = 3 \cdot 10^{-3} \cdot C^{DNA}$. Similarly, considering PAMAM G6 MW = 68046.11 g/mol and 256 charges of positive surface groups, the concentration of molar charges is $C^{PAMAM6}_{molar\_charge} = 4.4 \cdot 10^{-3} \cdot C^{PAMAM6}$. The curve of the DNA/PAMAM G6 complex contains characteristic four Bragg peaks at the positions of $q = 1.4$, 1.6, 2.4, and 2.8 nm^{-1} respectively $d = 4.5$, 3.9, 2.6 and 2.2 nm. The peaks at $q =$ 1.4, 2,4 and 2.8 nm^{-1} correspond to the average distance between the DNA columns and are close to a ratio of $1:\sqrt{3}:2$, suggesting a 2D hexagonal organization of the DNA in a columnar phase. In contrast, the peak at $q = 1.6$ nm^{-1} may correspond to the average spacing between PAMAM G6 and DNA entities indicating the beginning of 3D ordered phase organization[93,124]. It means that DNA/PAMAM G6 complexes at pH = 8.5 have a 2D hexagonal

ordering with a tendency towards a 3D hexagonal organization. By adding heparin, this organization is strongly disturbed. When the ratio of heparin / DNA reaches 7 % in the DNA/PAMAM G6 solution, the peak at $q = 1.6$ vanishes, which can be interpreted in a way that the scattering objects in the complexes rearrange and change their morphology. Increasing the ratio of heparin / DNA to 10 % in the solution, all peaks disappear indicating that the 2D hexagonal organization is interrupted and DNA is released. Consequently, heparin can be used as a decompaction agent and unwarp DNA. As discussed above, the organization DNA/PAMAM complexes depend notably on the pH in the solution. At a pH = 5.5, DNA wraps around PAMAM G6, forming a beads-on-a-string structure and mimicking the nucleosome assembly in chromosomes. SAXS measurements of PAMAM G6/DNA and DNA/PAMAM G6 + 10% heparin at pH = 5.5 are shown in **Figure 2.13**, where the difference in the structure and shape of the complexes can clearly be observed.

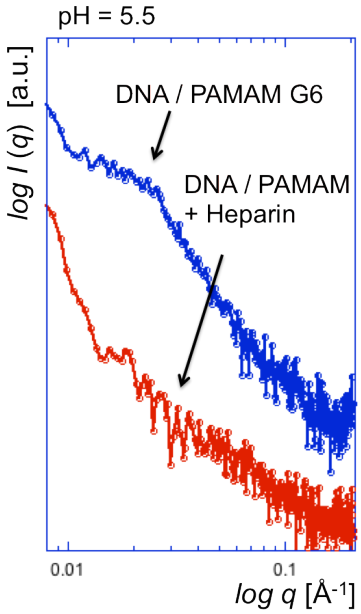

Figure 2.13: (a) Scattering curves of DNA/PAMAM G6 complexes (blue) and DNA/PAMAM G6 + 10% heparin complex structures (red). The curves are shifted by a constant factor for clarity.

2.5 Dynamic changes during DNA decondensation

During the studies in bulk, we discovered the difference of structures and forms of the PAMAM G6/DNA complexes and influence of heparin at various concentrations. Thereafter, the real-time dynamic evolution measurements of the interaction between DNA/PAMAM G6 complexes and heparin were performed using the aforementioned microfluidic device. Firstly, the PAMAM G6/DNA complex were prepared at the ratio of N/P = 1 and pH = 5.5. The X-ray absorption scan of the microfluidic device (step size 0.05 mm, exposure time 0.5 s) is shown in **Figure 2.14**. During the measurement, a solution with PAMAM G6/DNA complexes ($C_{DNA} = 8$ mg/ml) were pumped at 0.2 µl/s (3.3 mm/s) in the middle channel and 1 mg/ml heparin solution in the neighboring side channels at 0.2 µl/s (3.3 mm/s). As mentioned before, one of the main parameters for the fast mixing is a smaller diffusion path. Narrower reaction streams can be obtained using hydrodynamic focusing with two lateral buffer streams. The buffer flow rate was set to 0.6 µl/s (10 mm/s). Furthermore maximal flow velocity occurs in the middle of the channel, whereas the velocity at the walls is zero due to no slip boundary conditions. The measurements along the stream can be assigned to specific reaction times. The scattering data of the evolution of PAMAM G6/DNA complexes along the reaction with heparin measured for 4 hours per position are shown in **Figure 2.14**.

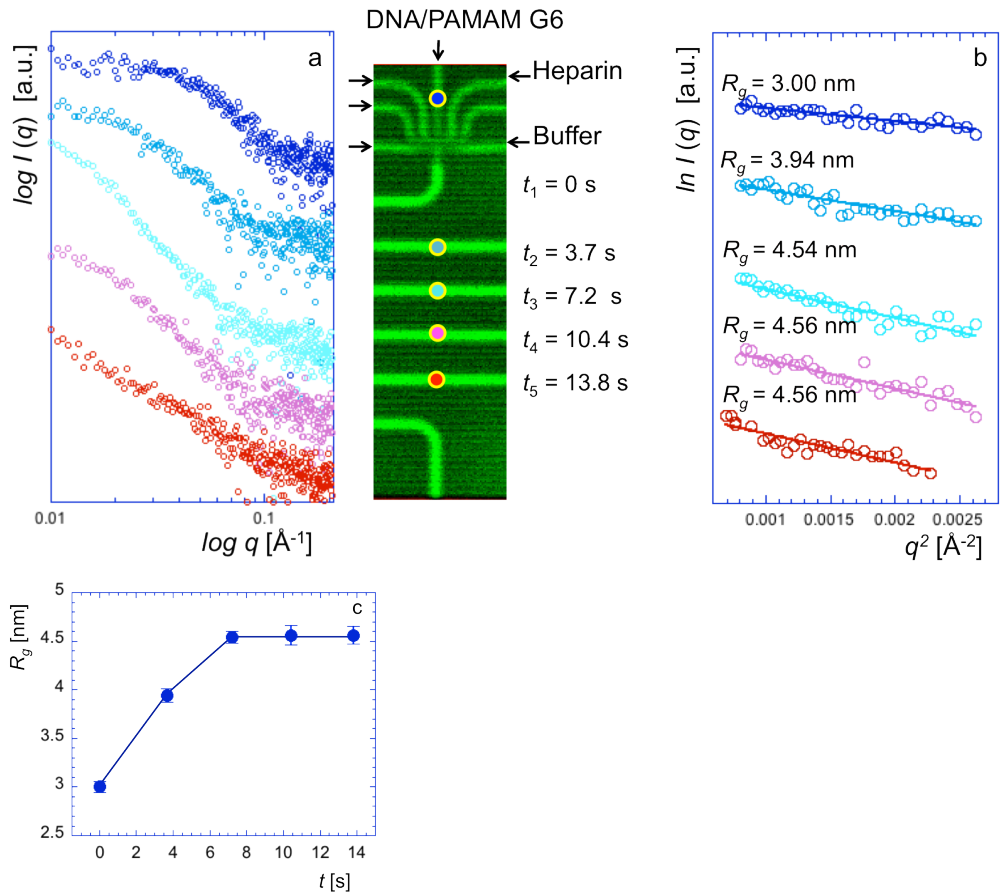

Figure 2.14: (a) SAXS intensity plots of time resolved PAMAM G6/DNA complexes during the reaction with heparin and the absorption scan of the device. Dot colors on the absorption scan coincide with the scattering curves, indicating the scattering position in the channel. (b) Guinier plots and linear fitting of the same data. (c) Radius of gyration changes versus reaction time. The curves are shifted by a constant factor for clarity.

In order to correctly subtract the background noise from the data, scattering of the buffer inside the device was acquired in a separate measurement at the same positions before the reaction. The shapes of the DNA/PAMAM/heparin complexes can be characterized by their radius of gyration R_g, which contains the information about the mass distribution within a complex[125]. The data can be analyzed using the Guinier approximation, which states that for sufficiently small values of q:

$$\ln[I(q)] = \ln[I(0)] - \frac{q^2 R_g^2}{3} \tag{2.9}$$

The Guinier plot of $\ln[I(q)]$ versus q^2 results in a straight line and R_g is determined by straight-line fitting from the slope $\left[-\frac{R_g^2}{3}\right]$[44,126]. The radii of gyration of DNA/PAMAM G6 complexes increase during the reaction with heparin. The interaction of heparin with the DNA/dendrimers complexes changes the form factor of the complex by releasing DNA from cationic dendrimers and further forming new and larger heparin/dendrimer complexes (**Figure 2.14a**).

The same microfluidic device geometry was used to obtain more advanced measurements of DNA condensation and decondensation in one experiment, where a direct competition between DNA and heparin for PAMAM occurs. The idea of the sample flow in the device and the scattering data of the mixture are shown in **Figure 2.15**. Different solutions were connected to the device as shown on the absorption scan in **Figure 2.15.** The flow rate for the DNA solution at the middle inlet was set to 0.2 µl/s, for the PAMAM G6 and heparin solutions to 0.2 µl/s and the buffer solution at the lateral inlet to 0.6 µl/s.

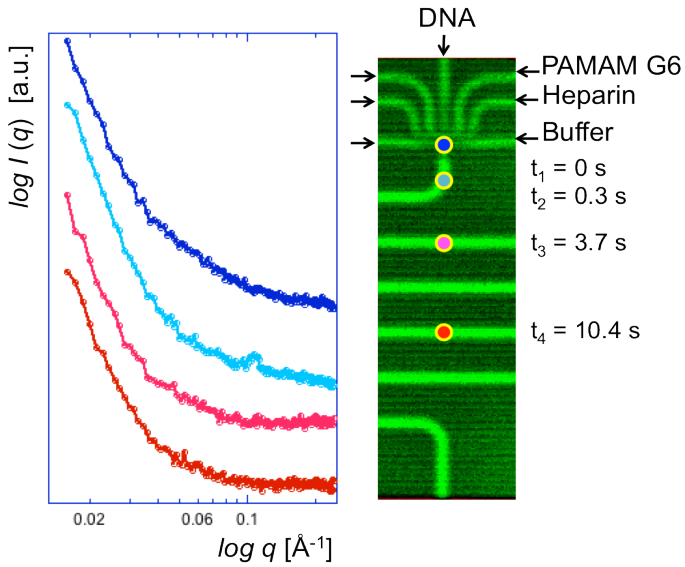

Figure 2.15: SAXS curves of the reaction of PAMAM, DNA and heparin and the absorption scan of the device. Dot colors on the absorption scan coincide with the scattering curves, indicating the scattering position in the channel. The curves are shifted by a constant factor for clarity.

Slight differences in curves can be observed, which probably indicates the heparin/PAMAM G6 complex formation. However, due to the short DNA and PAMAM G6 interaction time no DNA/PAMAM G6 complex was formed.

2.6 Summary and outlook

In summary, we have studied DNA compaction and release from PAMAM G6 dendrimers. Due to the size and charge density, PAMAM G6 can be used as a histone core model protein. Charge induced sequence independent electrostatic interaction between DNA and PAMAM G6 were investigated at a relative charge ratio of N/P=1 using an in-house SAXS setup. We have analyzed the DNA / PAMAM G6 complexes formation at different pH. At pH = 5.5 complexes form beads-on-a-string structures and at pH = 8.5 they have a 2D hexagonal organization with the tendency towards the 3D hexagonal organization. Thus, by changing the pH it is possible to control the interaction of PAMAM G6 and DNA. The DNA release from PAMAM G6 was initiated by heparin due to the competitive interaction with DNA. The bulk measurements were performed at different heparin concentrations in the DNA / PAMAM G6 complex solution at pH = 8.5. We found that in the presence of heparin, scattering objects in the DNA / PAMAM G6 complexes rearrange and change their morphology and the complex organization is disturbed. When the heparin / DNA ratio is about 10%, DNA is released from PAMAM G6. In order to perform real-time dynamic measurements of the DNA and PAMAM G6 interactions, we developed an X-ray compatible, fast mixing, microfluidic device. Scanning the reaction at different positions along the channel, we measured the time evolution of the heparin interaction with DNA / PAMAM G6 complexes. We detected the form factor changes of the scattering curves and measured the shape of the complex by their radii of gyration R_g, applying the Guinier approximation. The increase of R_g indicates DNA release from cationic dendrimers due to the interaction with heparin. Furthermore, measurements of the DNA, PAMAM G6 and heparin interactions were performed in a microfluidic device, which demonstrate the DNA / heparin complex formation, whereas no DNA / PAMAM G6 complex

was detected. The combination of SAXS and our fast mixing microfluidic device allows for time evolution measurements of reactions at nanoscale *in situ* and can be applied for further and different biomimetic systems.

Chapter 3

Formation of actin networks in microfluidic concentration gradients

The following section has been published in:

Frontiers in Materials, Volume 3, 20, 2016
http://dx.doi.org/10.3389/fmats.2016.00020

Formation of actin networks in microfluidic concentration gradients

Natalja Strelnikova[1], Florian Herren[1], Cora-Ann Schoenenberger[1], Thomas Pfohl[1,*]

[1]Department of Chemistry, University of Basel, Basel, Switzerland
* Correspondence: Thomas Pfohl, Department of Chemistry, University of Basel, Klingelbergstrasse 80, Basel, 4056, Switzerland
thomas.pfohl69@gmail.com

Keywords: microfluidics, filaments, bundling, heterogeneous networks, FEM simulations.

Abstract

The physical properties of cytoskeletal networks are contributors in a number of mechanical responses of cells including cellular deformation and locomotion, and are crucial for the proper action of living cells. Local chemical gradients modulate cytoskeletal functionality including the interactions of the cytoskeleton with other cellular components. Actin is a major constituent of the cytoskeleton. Introducing a microfluidic-based platform, we explored the impact of concentration gradients on the formation and structural properties of actin networks. Microfluidics-controlled flow-free steady state experimental conditions allow for the generation of chemical gradients of different profiles, such as linear or step-like. We discovered specific features of actin networks emerging in defined gradients. In particular, we analyzed the effects of spatial conditions on network properties, bending rigidities of network links, and the network elasticity.

3.1 Introduction

The active and passive mechanical performance of the cytoskeleton is based upon crowded solutions and networks that are mainly comprised of actin, microtubules and intermediate filaments[127]. Actin and actin filaments, the major structural and functional element of the cytoskeleton, form a variety of higher-order assemblies with specific designs, properties and functions[128,129]. These specialized superstructures are highly dynamic in space and time as evidenced most prominently by cells that move and/or change their shape[130]. Moreover, the heterogeneous structure and dynamic organization of the actin networks are essential for numerous biological processes.

Microfluidics has been applied in a wide range of studies on actin dynamics. For example, the behavior of filamentous actin (F-actin) in confinement[131] and microflow[132], and the assembly and dissembly of F-actin[133,134], bundles[135], and supramolecular networks[62,136] have been studied using microfluidics approaches.

Microfluidics is also a promising tool for establishing and controlling well-defined chemical gradients, which considering the significance of microenvironments, is of great interest in biological research[137,138]. Different microfluidic platforms are applicable including laminar flow[139], transient[63], and steady state[64] gradient generators. For example, laminar flow microfluidic gradient generators are being used for the analysis of chemotactic and migratory behavior of cells[38,140,141]. However, to study formation of soft materials, supramolecular assemblies and networks in concentration gradients, only flow-free transient or steady state generators are feasible where interference of flow with the assembly process can largely be excluded.

Here, we present a new approach to create steady state and flow-free concentration gradients for examining actin polymerization *in situ*. Using time-lapse epifluorescence microscopy with high spatiotemporal resolution, we monitored the formation of actin filaments in a KCl gradient. Moreover, using Mg^{2+} as a bivalent cationic bundling agent for actin filaments, we show the concentration-dependent formation of bundled F-actin networks with anisotropic physical properties.

3.2 Materials and Methods

3.2.1 Microfluidics platform

Using standard soft lithography methods[136], we have fabricated microfluidic devices with two flow channels (height $h_{channel}$ = 5 µm, width 50 µm), which are connected to small bypasses (h_{bypass} = 0.5 – 1 µm) as illustrated in **Figure 1** and **2**. The two bypasses are connected to either a rectangular gradient chamber ($h_{chamber}$ = 0.5 – 1 µm, width 40 µm, length 350 µm) or to five serially connected square chambers ($h_{chamber}$ = 0.5 – 1 µm, side length 40 µm each), which are both diffusion-controlled. The multi-height masters, which were used as a mold for corresponding microfluidic devices, were fabricated in SU8 negative photoresists (Microchem, Newton, MA, USA) coated on silicon wafers (Si-Mat, Kaufering, Germany). In order to produce the microdevices, replicas of the masters were fabricated in polydimethylsiloxane (PDMS) and finally plasma-sealed to glass slides. To prevent actin adsorption to the microdevice walls, the device was flushed with bovine serum albumin solution (BSA 1 mg/mL, Sigma Aldrich, Switzerland). The device was submerged in water before and during the experiments to eliminate permeation-driven flow through PDMS.
The controlled supply of solutions to the two flow channels was achieved by syringe pumps (neMESYs low pressure syringe pump, Cetoni GmbH, Germany) using 100 µL syringes (Hamilton, Switzerland), which were connected to the microdevice inlets via polytetrafluoroethylene (PTFE) tubing.

3.2.2 Protein solutions

Lyophilized actin and fluorescent Atto488-actin from rabbit skeletal muscle were purchased from Hypermol EK (Bielefeld, Germany). To prepare the monomeric actin solution, 3 µM stock solutions of Atto488-actin and actin in 2 mM Tris-HCl (pH 8.2), 0.4 mM ATP, 0.1 mM $CaCl_2$, 0.5 mM DTT were prepared and mixed at a 1:5 (v/v) ratio. For actin polymerization solution ("KCl solution"), monomeric actin solution was supplemented with 100 mM KCl, 2 mM $MgCl_2$, 0.1 mM $CaCl_2$, 1.4 mM ATP, 0.5 mM DTT, 10 mM imidazole, 2 mM

Tris-Cl (pH 7.4) and 0.2 % disaccharides. The actin bundling solution ("$MgCl_2$ solution") has the same composition as the actin polymerization solution ("KCl solution") with the exception of a higher $MgCl_2$ concentration of 50 mM.

3.2.3 Microscopy and image analysis

Polymerization and bundling experiments in gradients were observed with an Olympus IX81 inverted microscope equipped with fluorescence illumination (X-Cite Series 120 Q). 40x (N.A. 1.30) UPlanFL N or 100x (N.A. 1.49) UApo N oil immersion objectives were used for the experiments. Images were recorded with a PCO Edge SensiCam (PCO AG, Kelheim, Germany) with exposure times of 100 ms. Images were processed and analyzed using ImageJ (version1.47k, Wayne Rasband, National Institute of Health, USA).

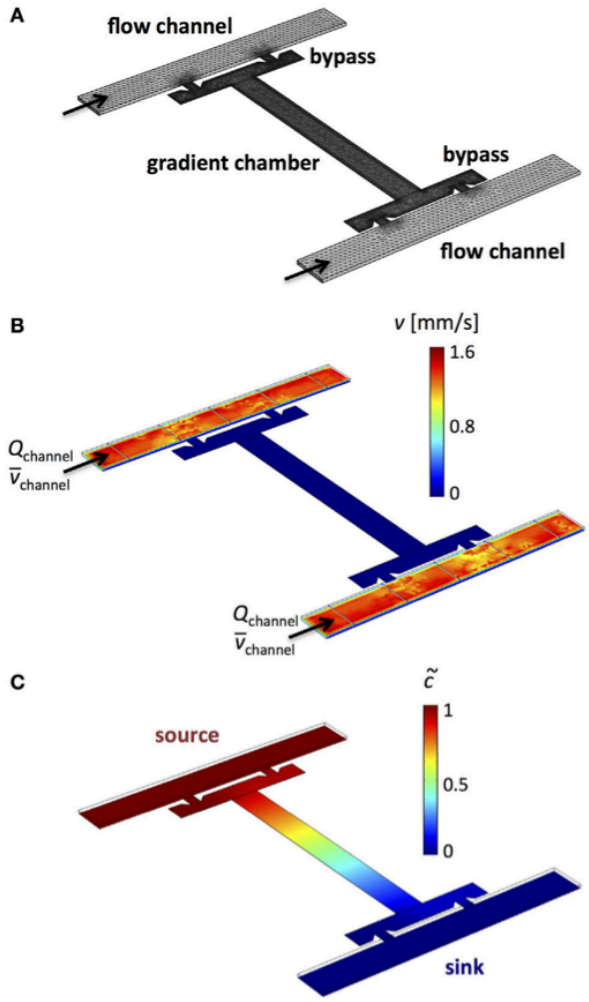

Figure 3.1: Microfluidic device design for flow-free, steady-state linear gradients. (a) Design of a multiheight device with two flow channels, corresponding bypasses and a rectangular microchamber. (b) Computational simulation of velocity distribution of flow within the microfluidic device reveals advective transport in the two flow channels and absence of flow across the rectangular microchamber. (c) A linear concentration gradient across the rectangular microchamber is generated when one flow channel acts as the concentration source and the other flow channel as the sink.

3.2.4 Simulations

All simulations were carried out using COMSOL Multiphysics 4.3a, a program solving partial differential equations numerically using the finite element method (FEM). The used mesh of the gradient chambers and the two flow channels consisted of 90'227 elements. The fluid velocities or pressures in the flow channels were tuned at the inlets. The incompressible Navier-Stokes

equation was solved for the geometry with no-slip boundary conditions at the walls. A stationary flow-field was obtained and used to solve the advection-diffusion-equation.

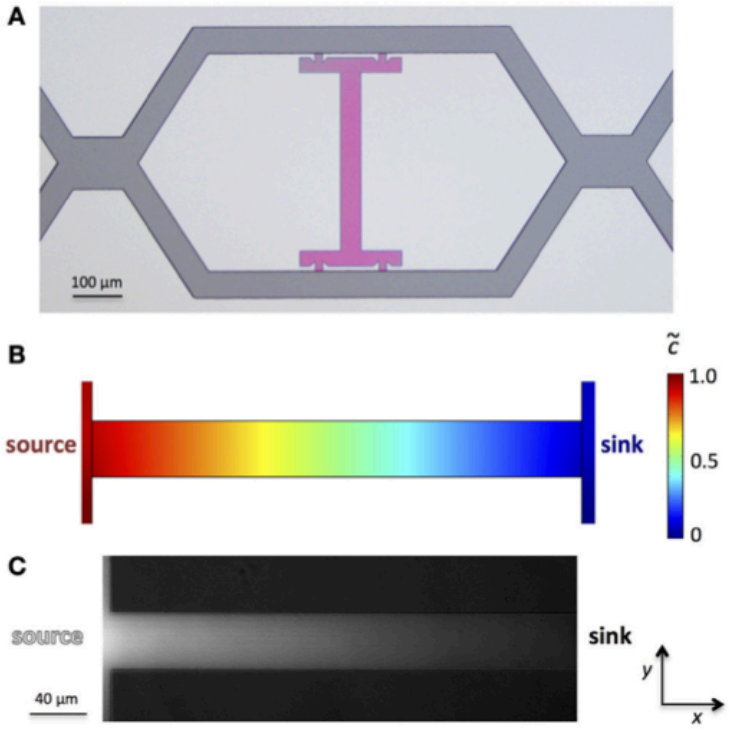

Figure 3.2: Experimental realization of a microfluidic device for flow-free, steady state linear gradients. (a) The bright-field image of the device master prepared by photolithography is shaded with dark grey (flow channels) and pink (bypasses and microchamber) to visualize the multi-height design. The simulated linear concentration gradient (b) can be verified by an aqueous fluorescein solution using the left flow channel as the fluorescein source and the second as the sink (c).

3.3 Results and Discussions

3.3.1 Microfluidic device for flow-free, steady state linear gradients

Based on the principles of diffusion-advection chamber microfluidics[62,136], we developed a microfluidic setup for generating flow-free, steady state concentration gradients. The corresponding microfluidic device consists of

two controllable flow channels (width 50 µm, height h_{channel} = 5 µm), either of which is connected to a bypass by two small connecting channels (width 5 µm, height h_{bypass} = 0.5 – 1 µm) as shown in **Figure 3.1** and 3.2. The two bypasses are interconnected by a rectangular chamber (width 40 µm, length 350 µm, h_{chamber} = 0.5 – 1 µm). In case of an equal pressure difference Δp between the inlet and outlet of both flow channels or equal volume flow rates Q_{channel} in both channels, a diffusional interface between the main flow channels and bypasses with the rectangular microchamber is created. The approximately ten-fold larger height of the flow channels in comparison to the bypasses and microchamber generates a volume flow reduction of several orders of magnitude, and thus, diffusion is the dominating transport mechanism for molecules in the microchamber. **Figure 3.1b** shows the distribution of flow velocity v in the microfluidic device calculated by finite element simulations. Based on these simulations, we find a reduction of the volume flow rate of $Q_{\text{channel}}/Q_{\text{bypass}} \approx 6250$ (or a reduction of the mean flow velocity of $\bar{v}_{\text{channel}}/\bar{v}_{\text{bypass}} \approx 250$) between the flow channels and the bypasses and a reduction of $Q_{\text{channel}}/Q_{\text{chamber}} \approx 2.1 \cdot 10^6$ ($\bar{v}_{\text{channel}}/\bar{v}_{\text{chamber}} \approx 1.7 \cdot 10^5$) between the flow channels and the center position of the microchamber, using an input volume flow rate of the channels, $Q_{\text{channel}} = 0.25\,\text{nL/s}$ ($\bar{v}_{\text{channel}} = 1.0 \cdot 10^{-3}\,\text{m/s}$).

In order to generate a linear concentration gradient across the rectangular microchamber, one flow channel served as the concentration source through addition of the gradient-forming substance to the solution while the second flow channel served as the concentration sink (**Figure 3.1c**). Finite element simulations of the linear concentration gradient are shown in **Figure 3.2b**. Using an aqueous fluorescein solution as the concentration source and an aqueous solution without fluorescein as the sink, a stable fluorescein gradient was established across the microchamber in x-direction (**Figure 3.2c**), assuming that the fluorescence intensity increases linearly with the concentration of fluorescein. Important for the stability of flow-free, steady state gradients is a good control of the volume flow rates ($Q_{\text{channel 1}} = Q_{\text{channel 2}}$) or of the pressure drops ($\Delta p_{\text{channel 1}} = \Delta p_{\text{channel 2}}$) in both flow channels. The control of flow can be facilitated by adding pressure adjustment points upstream of the microchambers, where the two flow channels come in

contact for a short distance. At these sites, which are shown in the image of the microdevice master in **Figure 3.2a**, the pressures of the two flow channels are equilibrated, making the adjustment of the two individual solution flows (source and sink) more amenable.

The time of achieving a fully developed steady state gradient of fluorescein can be estimated by using $t = \frac{x^2}{2D}$, with x = 430 µm, the microchamber length including the bypasses, and the diffusion coefficient of fluorescein, $D_{\text{fluo}} = 425\,\mu\text{m}^2/\text{s}$ [142]. A gradient is fully developed in $t_{\text{fluo}} \approx 215\,\text{s}$. However, a gradient with around 90 % of the final steady state gradient concentrations can be achieved in less than $\frac{1}{2}t$.

In the following, we study the polymerization of actin monomers into filaments in a KCl gradient, and the bundling of actin filaments (F-actin) in a gradient of Mg^{2+}. Due to the smaller size of these ions in comparison to fluorescein, we expect a faster evolution of the concentration gradients with $t_{K^+} \approx 46.2\,\text{s}$ for K^+ ($D_{K^+} = 2000\,\mu\text{m}^2/\text{s}$) and $t_{Mg^{2+}} \approx 132\,\text{s}$ for Mg^{2+} ($D_{Mg^{2+}} = 700\,\mu\text{m}^2/\text{s}$)[143].

3.3.2 Actin polymerization in KCl gradients

In vitro actin polymerization can be initiated by adding 50 mM KCl to a buffered solution of monomeric actin[136]. To address the polymerization of actin in KCl gradients, we aimed to form a linear steady state gradient ranging from 0 to 100 mM KCl. The channel operating as the KCl source was flushed with a solution of actin monomers (3 µM) containing 100 mM KCl, whereas the second flow channel was flushed with a solution containing only actin (3 µM) to operate as a sink. Under these conditions, a linear KCl gradient could be generated with a concentration of about 100 mM KCl at the interface between the bypass and microchamber at the source side, and about 0 mM at the interface between the bypass and microchamber at the sink side, with approximately 50 mM KCl at the center of the microchamber. Due to the much slower polymerization time of actin filaments in comparison to the time achieving a stable KCl gradient, the whole polymerization process occurs in a

linear KCl gradient across the microchamber. Using fluorescently labeled actin, the polymerization process can be directly followed by fluorescence microscopy. After a few hours, a stationary state of partially entangled polymerized actin filaments was reached. The impact of the KCl gradient on the assembly of entangled actin filaments is shown in **Figure 3.3**. Actin polymerization can occur, when the concentration of unassembled subunits is above a critical concentration, which is about 0.1 µM in 100 µM KCl as well as *in vivo*[6]. Thus, along a steady state KCl gradient in the chamber, the monomer concentration decreases from 3 µM to 0.1 µM with increasing KCl, whereas the polymer density is increasing.

A transition zone from a semi-dilute entangled filament solution defined by a number density of actin filaments $\rho \gg \frac{1}{l^3}$, with the length l of the filaments, to a dilute solution defined by $\rho \ll \frac{1}{l^3}$ [144] was observed at a distance of about ¾ of the microchamber length ($x \sim 260\,\mu m$) away from the source, which corresponds to a concentration of ~25 mM KCl. Semi-dilute solutions of entangled actin filaments show distinct viscoelastic properties. At intermediate strain frequencies, which represent the time scales that are significant in cells, solutions of semi-dilute filaments behave like networks of temporarily fixed links[144,145]. In this frequency range, the storage modulus G' shows a plateau with $G' \propto \rho^{7/5} k_B T$, where k_B is the Boltzmann's constant and T the absolute temperature[144]. We find an almost linear decrease of the density of actin filaments ρ from 100 – 25 mM KCl ($x \sim 0 - 260\,\mu m$, **Figure 3.3**), $\rho \propto c_{KCl}$. Using the aforementioned relation for G', are proportionality of $G' \propto c_{KCl}^{7/5} k_B T$ in this regime should be expected. In the dilute regime ($x \gtrsim 260\,\mu m$), actin solutions show an almost purely viscous behavior with a viscosity close to the solvent[144].

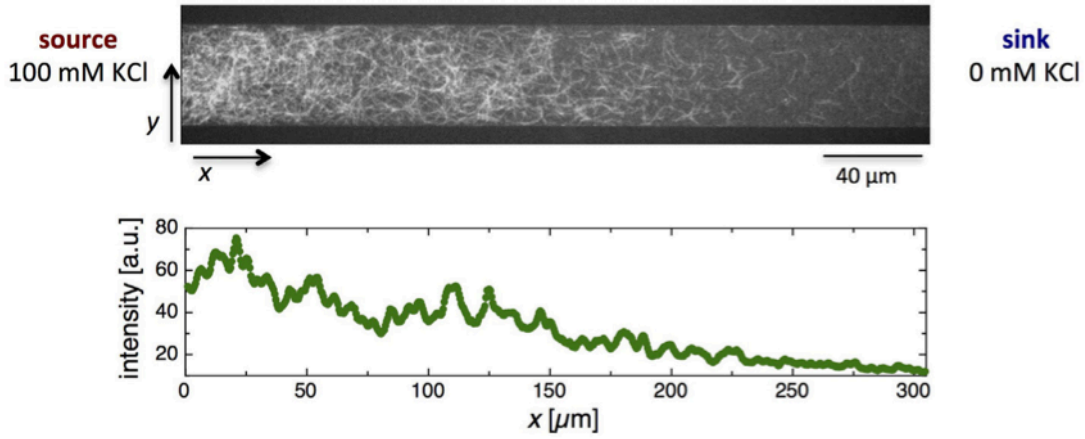

Figure 3.3: Fluorescence micrograph of actin filament assembly in a KCl gradient over a rectangular microchannel (top panel). The density of the entangled actin filaments decreases with decreasing KCl concentration. In the bottom panel, the decrease in F-actin density is represented as a plot of the averaged fluorescence intensity against the distance from the source, x.

3.3.3 Formation of networks of F-actin bundles in Mg^{2+} gradients

Multivalent cations in the mM range, such as Mg^{2+}, cross-link F-actin by compensating the electrostatic repulsion between filaments, which are overall negatively charged with a linear charge density of 4 e^-/nm. Beyond a critical multivalent cation concentration, a sharp bundling transition of filaments occurs[62,146]. In order to form a Mg^{2+} cross-linking gradient along the microchamber with entangled filaments, Mg^{2+} was added to the flushing solution of one of the flow channels and not to the other. The formation of a network of bundled F-actin in a linear Mg^{2+} gradient is shown in **Figure 3.4a**. In a first step, an anisotropic, partially entangled F-actin solution was formed in a linear KCl gradient (~0 - 100 mM KCl) over several hours. Subsequently, a linear Mg^{2+} (~0 - 50 mM Mg^{2+}) was generated. For the final steady state (**Figure 3.4a**), one flow channel was flushed with an actin solution (3 µM) containing 100 mM KCl and 50 mM Mg^{2+} to operate as KCl and Mg^{2+} source, and the second flow channel was only flushed with an actin solution (3 µM) without additional salts. In comparison to the F-actin polymerization which takes several hours under the experimental conditions used, actin filaments

undergo a fast bundling transition within a few minutes. Subsequently, bundles fuse together to give rise to a network of bundled F-actin.

We found two distinct regimes of the bundled F-actin along the Mg^{2+} concentration gradient. At the source side of the microchamber, a single network of actin bundles emerged in response to the bundling agent. The actin filaments were frequently shared between two or more links of the network, aided by the close proximity of the entangled filaments. Adjacent to the percolated network towards the sink side of the microchamber, isolated, non-interconnected bundles were detected. This behavior appeared to be related to the decrease of filament density resulting from the decrease of the KCl concentration rather than the decrease of the Mg^{2+} concentration.

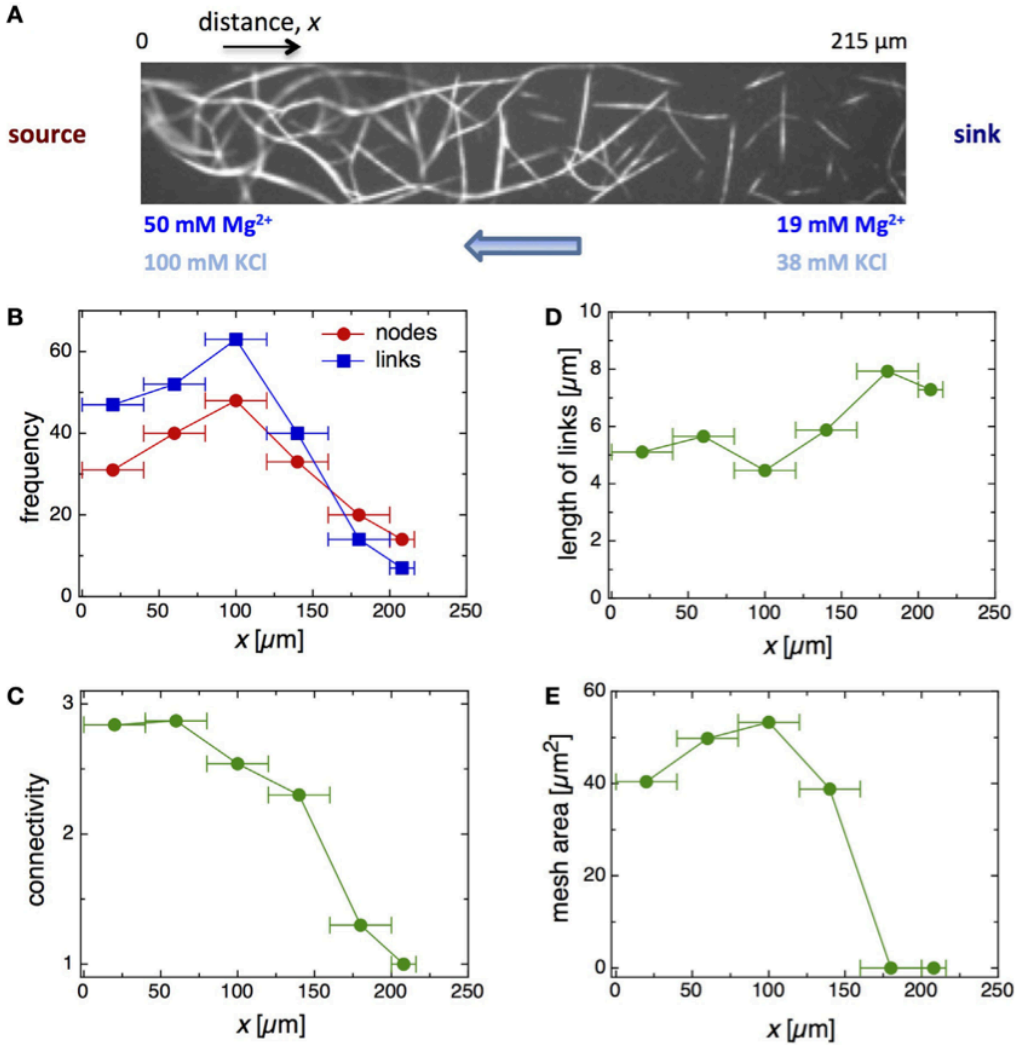

Figure 3.4: (a) Fluorescence micrograph of the formation of a Mg^{2+} induced F-actin bundle network in a double gradient of KCl and Mg^{2+}. Several network properties are plotted against the x-position along the concentration gradients including the

frequency of nodes and links (b), the network connectivity (c), the length of links (d), and the mesh area (e).

To gain more insight into the bundling of F-actin in Mg^{2+} gradients, the network properties along the concentration gradient were further characterized. We analyzed the nature of links, nodes and meshes of the network depending on their position in the microchamber and thus the gradient. The number of links and nodes versus the x-position of the microchamber are shown in **Figure 3.4b**. The link and node numbers of the network are slightly increasing from the beginning of the chamber at $x \sim 20\mu m$ to position $x \sim 100\mu m$, followed by a strong decrease at larger distance. Up to $x \sim 140\mu m$, the number of links is greater than the number of nodes, but switches at $x \geq 180\mu m$. Conceivably, this observation is attributed to the poorly evolved network and the appearance of isolated bundles at these positions. The connectivity obtained, and number of incident links on a specific node (**Figure 3.4c**) further supported this notion. For the network developed, we found an average connectivity of about 3^{62} that slightly decreased with increasing x. In addition, we observed a jump to an average connectivity value of about 1 at $x \sim 180\mu m$, which correlates to the presence of isolated bundles. The average link lengths within the network were approximately 5 µm (**Figure 3.4d**), and the average mesh areas between 40 - 60 μm^2 (**Figure 3.4e**). In comparison, the average link length of isolated bundles are 8 µm. In regions with only isolated bundles, the average mesh areas were obviously 0.

Overall, in the gradient of KCl and Mg^{2+}, a single percolated network of F-actin bundles was formed that spread on the source side to an x-position of about 160 µm in the microchamber, followed by a region of isolated bundles that tapered off towards the sink side. For the network between $x \sim 0$ - 120 µm, we found almost the same network properties - average number of length and nodes, connectivity, link length and mesh area indicating that the entangled filaments form a homogenous network of F-actin bundles in this region. In view of the decrease in filament density associated with the KCl gradient with no bundling agent, this result is astonishing (**Figure 3.3**). Only at the border to the transition zone to the isolated bundle phase was the

network connected looser, with more open link ends that lead to a reduced connectivity.

In order to elucidate the mechanical behavior of the network of F-actin bundles, the amount of filaments inside the bundles was estimated on the basis of their fluorescence intensity profiles. As shown in **Figure 3.5a**, the greyscale histogram of the fluorescence micrograph of the network (**Figure 3.4a**) was plotted and analyzed. Higher greyscale values correspond to thicker bundles, which are composed of a higher number of filaments. To characterize the filament distribution within the network, we have defined four different greyscale intervals (grey, red, blue and green areas in plot 3.**5a**), which represent different bundle thickness or amount of filaments. To translate the greyscale value into numbers of filaments, a linear increase of the fluorescent intensities with the number of filaments per bundle was assumed[62]. The selected intervals correspond to a number of filaments of $n_{\text{grey}} \sim 2-6$, $n_{\text{red}} \sim 6-11$, $n_{\text{blue}} \sim 11-16$, and $n_{\text{green}} \gtrsim 16$. To illustrate this analysis, the network of F-actin bundles was color-coded according to the number of filaments in the network links (**Figure 3.5b**). The distribution of the four classes of bundle thickness (i.e., number of filaments) in the network links versus the spatial position x is shown in **Figure 3.5c**. Up to $x \sim 120$ µm, no major differences between the relative frequencies of red, blue, and green bundles (20 25 %) or for the grey bundles (25 40 %) were observed. However, fewer thicker (red, blue and green) bundles and an increase in thinner bundles (grey) were observed in the network close to the transition zone ($x \sim 120-160$ µm). The isolated bundles ($x \gtrsim 160$ µm) were much thinner than the bundles in the network and consist primarily of grey bundles.

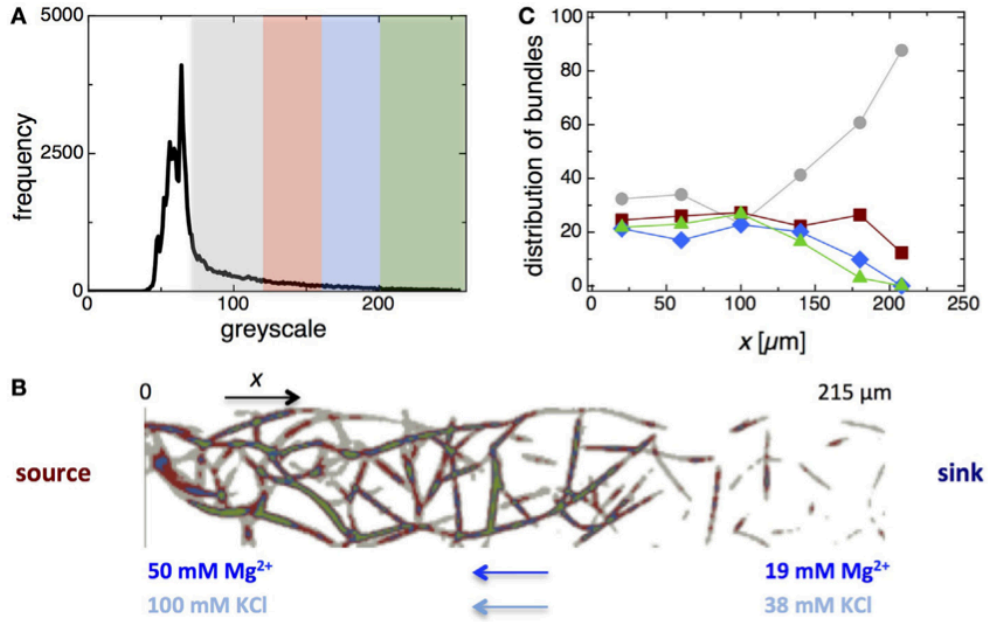

Figure 3.5: Analysis of the distribution of bundle thickness within the F-actin bundle network. (a) Frequency histogram of greyscale values of the fluorescence micrograph of the F-actin bundle network (**Figure 3.4a**). The greyscale is divided into four segments that represent bundles of different thickness grey represents bundles with filament numbers of n_{grey}~$2-6$, red with n_{red}~$6-11$, blue with n_{blue}~$11-16$, and green with $n_{\mathrm{green}} \gtrsim 16$. (b) Fluorescence micrograph of the bundle network colorized according to the amount of filaments within the network links. (c) Distribution of four classes of bundle thickness, i.e. number of filaments, in the network links versus the distance, x from the source of the double gradient.

In the range between $x \sim 0$ 120 µm, the network exhibited not only similar properties, but also a comparable distribution of filament numbers within the bundles, indicating that the composition and the mechanical properties of this network section were homogenous. As mentioned above, considering the gradual decrease of filament density prior to bundling (in the absence of bundle inducing Mg^{2+}), this result is surprising. During the bundling and fusion processes involved in network formation, a redistribution of the filaments occurs. At the length scale of a few tenths of a micrometer, the Brownian motion of semiflexible filaments as well as of the partially formed and fused bundles may be fast enough to support this reorganization of F-actin within network section. In the transition region ($x \sim 120-160$ µm), the links within the networks are becoming thinner as indicated by a relative

increase of the thinner (grey) bundles and a decrease of the number of thicker bundles.

Describing the links in the network as homogenous rods made up of a definite number n of actin filaments, the elastic properties of the bundles can be determined from the bending rigidity κ_n, a parameter describing the resistance of a rod to a bending force. The bending rigidity κ of a single actin filament can be calculated from its persistence length $L_P \approx 13\mu m$ [131] by $\kappa = L_P k_B T \approx 5.3 \cdot 10^{-26} \mathrm{Nm}^2$ with the Boltzmann's constant k_B and the temperature T. To describe the bending of a bundle consisting of n filaments, two limiting types of F-actin bundle bending can be distinguished. In the decoupled case, bending shows no interfilament shearing as the interjacent crosslinks do not resist shear. The bending rigidity of a bundle κ_n depends linearly on the number of filaments n, $\kappa_n = n \cdot \kappa$. In the fully coupled case, crosslinks strongly resist shear and show a quadratic dependence, similar to the bending of a homogenous mechanical beam, $\kappa_n = n^2 \cdot \kappa$. Interestingly, Ca^{2+}-induced bundles show a partly coupled behavior, $\kappa_n = n^{1.3} \cdot \kappa$, most probably due to an optimization of the charge distribution inside the bundles[4]. Since the flexural rigidity of Ca^{2+}- and Mg^{2+}-induced bundles are very similar[147,148] and Mg^{2+} ions also bundle filaments by counter-ion condensation, we presume the same partly coupled case for Mg^{2+}-induced bundles as for Ca^{2+}-induced bundles. Therefore, the bending rigidity of bundles within the network can be calculated by $\kappa_{n,\mathrm{Mg}^{2+}} = n^{1.3} \cdot L_P k_B T$. The bundles of the network in the region between $x \sim 0$ 120 µm have an average bending rigidity of $\kappa_{n,\mathrm{Mg}^{2+}}^{0-120} \approx 1.3 \cdot 10^{-24} \mathrm{Nm}^2$, and in the transition region to isolated bundles ($x \sim 120$ 160 µm) of $\kappa_{n,\mathrm{Mg}^{2+}}^{120-160} < 1 \cdot 10^{-24} \mathrm{Nm}^2$.

3.3.4 Gradient formation across sequential microchambers

Connecting the two bypasses of the flow channels by five sequentially linked square microchambers, each with a side length of 40 µm, an interesting variation of the microfluidic gradient device can be introduced (**Figure 3.6**). This design should generate a nearly step-like gradient profile with a steep gradient in the narrow channels connecting the microchambers and an almost constant gradient across individual microchambers. The realization of a steady

state, step-like change of concentrations resulting from a sequence of microchambers is confirmed by finite element method simulations (**Figure 3.6a**) as well as by fluorescein experiments, where an aqueous fluorescein solution flowing in one of the flow channels served as a concentration source and an aqueous solution without fluorescein in the second flow channel as a sink (**Figure 3.6b**).

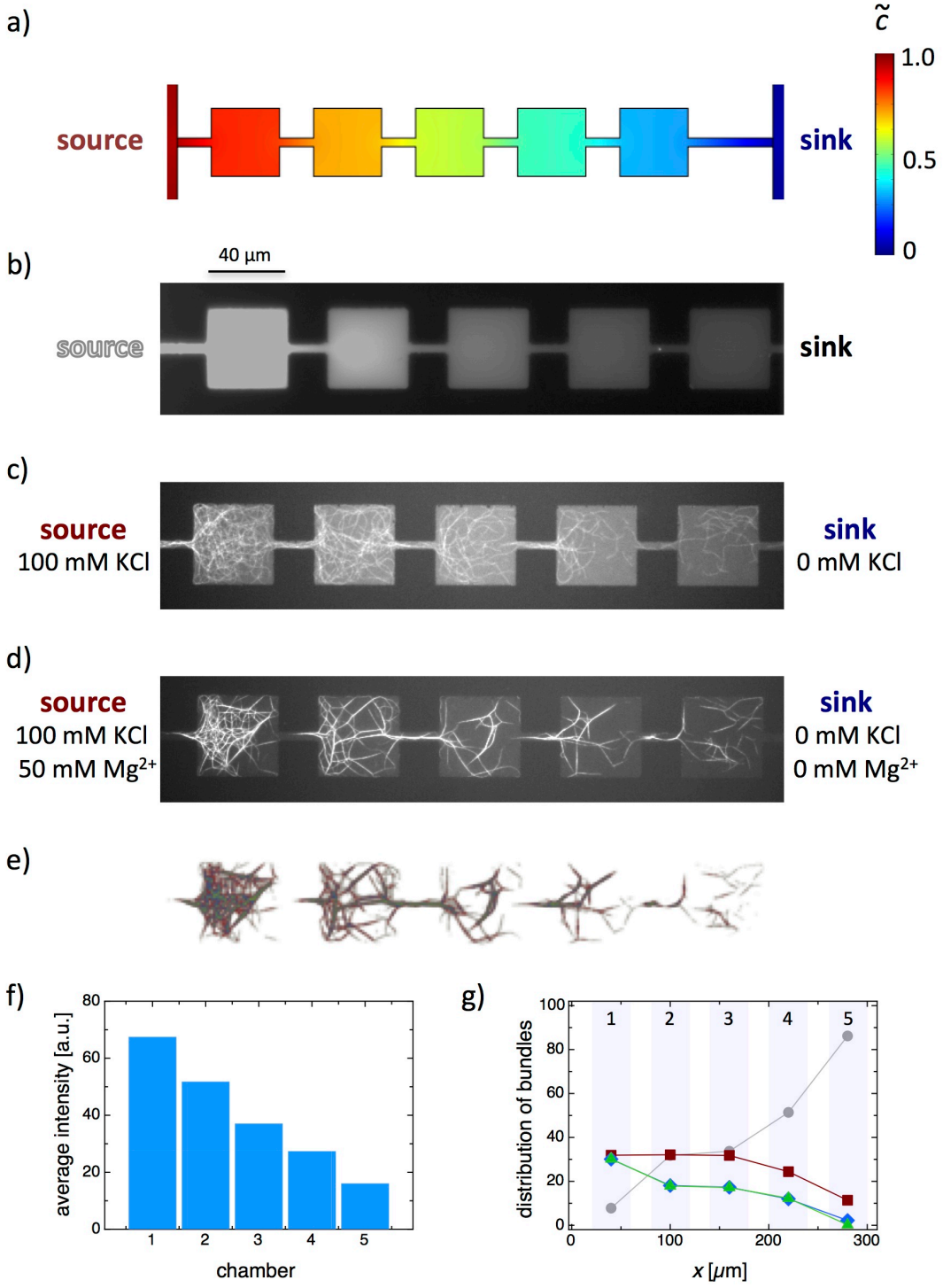

Figure 3.6: Experimental realization of microfluidic gradient formation over consecutive microchambers. (a) Simulations reveal a step-like gradient profile with a steep gradient in the narrow connecting channels and an extremely weak gradient across individual squared microchambers. (b) The step-like gradient was experimentally verified by using an aqueous fluorescein solution as a source. (c) Actin polymerization in a KCl gradient over a series of five connected square

microchambers shos a decreased amount of filaments from one microchamber to the next from the source to the sink. (d) Formation of bundled F-actin networks in a double gradient of KCl and Mg^{2+}. (e) Fluorescence micrograph of the bundle network colorized according to the amount of filaments within the network links (grey represents bundles with $n_{\mathrm{grey}}\sim 2-6$, red with $n_{\mathrm{red}}\sim 6-11$, blue with $n_{\mathrm{blue}}\sim 11-16$, and green with $n_{\mathrm{green}}\gtrsim 16$). (f) Average fluorescence intensity plotted against the chamber number, where chamber 1 is closest to the source and chamber 5 is closest to the sink. The average fluorescence intensity is proportional to the overall number of filaments in a microchamber. (g) Distribution of four classes of bundle thickness, i.e. number of filaments, in the network links versus the microchamber number.

A corresponding microdevice was used to examine the effects of a KCl gradient over the sequentially connected chambers on actin polymerization. One flow channel was flushed with a freshly prepared actin solution of (3 μM) containing 100 mM KCl as the KCl source while a sink was provided by flushing the other flow channel with a corresponding actin solution (3 μM) without KCl. The fluorescence micrograph at steady state (**Figure 3.6c**) revealed a decrease in the amount of filaments in consecutive microchambers from the source to the sink. However, contrary to what the simulations and fluorescein experiments led to expect, the distribution of filaments within individual microchambers was not always homogeneous. Conceivably, this effect might emerge from the trapping and entrenchment of filaments in the narrow connection channels[134], which was most evident at the higher KCl concentrations.

The formation of an additional Mg^{2+}-cross-linker gradient over the consecutive microchambers is shown in **Figure 3.6d**. Mg^{2+} was added to the actin solution in the source flow channel, whereas no Mg^{2+} was added to the sink flow channel. Under these conditions, the actin filaments underwent a bundling transition and formed bundles that ultimately fuse to give rise to a network of bundled F-actin. The density of the network as well as the network properties are strongly related to the amount of individual filaments that were found in the microchambers before the addition of Mg^{2+}. In the microchamber closest to the source (chamber 1), i.e. with the highest concentration of Mg^{2+} (~40 mM), the densest network with the smallest meshsize, the most links and nodes, and thickest bundles were observed. Moving from one microchamber

to the next toward the sink (from chamber 1 to 5), more open network structures with bigger meshsizes, less links and nodes, and thinner bundles were obtained. In the microchamber closest to the sink with the lowest Mg^{2+} concentration (~10 mM; chamber 5), a loose collection of bundles rather than a percolated network was found. Analyzing the overall filament number and the bundle thickness distribution (**Figure 3.6e**) in successive microchambers supports these observations. An almost linear decrease of the averaged fluorescence intensity, which is proportional to the overall number of filaments, from chamber 1 to 5 was obtained (**Figure 3.6f**). In addition, the thickest bundles within the networks are found in chamber 1, whereas the thickness and thickness distribution decreased with increasing chamber number and decreasing Mg^{2+} concentration (**Figure 3.6g**). Trapping and entrenchment of actin filaments in the narrow connection channels led to the accumulation of F-actin bundles at these sites independent of the Mg^{2+} concentration. In contrast to the long rectangular microchamber with a linear Mg^{2+} gradient (**Figure 3.4 and 3.5**), experiments with the sequential microchambers did not reveal a redistribution of actin filaments during the bundling process. Instead, the geometric partitioning produced a cross-linker gradient that resulted in distinct assembly levels of bundled F-actin networks from one chamber to the next.

3.4 Conclusions

We successfully developed a microfluidic-based method to generate steady state and flow-free gradients to discover polymerization, bundling, and network formation of the cytoskeletal protein actin under an unequaled range of experimental conditions. Using multi-height microfluidic devices with corresponding geometrical designs, linear and step-like gradients for polymerizing and cross-linking actin filaments were established. We analyzed the density distribution of actin filaments from semi-dilute to dilute polymer solutions that were formed in KCl gradients. Moreover, the ample and heterogeneous properties of actin networks that emerge in Mg^{2+} gradients at cross-linking concentrations could be determined by analyzing the space-

dependent connectivity, mesh sizes, and distributions of nodes, links and link lengths. Additionally, the local bending rigidity of the network as well as the overall elastic behavior could be estimated from the analysis of the bundle thicknesses and network geometry. Moreover, we found a partial redistribution of actin filaments during the bundling process in a linear double gradient of KCl and Mg^{2+}, which can be suppressed in step-like gradients achieved by geometric partitioning of the microchamber.

This powerful method can be applied to many other experiments involving anisotropic cytoskeletal materials. Owing to the extensive flexibility and simplicity of the microfluidic setup, the impact of material gradients that vary over time, as well as of many other manipulations including the effects of components that associate with the networks can be examined. Furthermore, by adding colloidal particles, the mechanical properties of the cytoskeletal assemblies that are formed in the respective gradients might be directly measured by microrheology[149,150]. The technique of investigating materials in gradients is not limited to components of the cytoskeleton but might be applicable to studies on other soft biological, synthetic or hybrid materials[151]. The combination of microfluidic gradients with advanced microscopy, spectro-microscopy, or X-ray nanoscattering and imaging[43] extends the potential of this technique even further.

Acknowledgments

We thank Stefan Arnold and Joël Wahl for their experimental support at different stages of the project and Zoe Swank and Siddharth Deshpande for fruitful discussions. Financial support by the Swiss National Science Foundation (SNF_200020_141270) and the NCCR Molecular Systems Engineering is gratefully acknowledged.

Author contributions:

NS, C-AS, and TP designed the experiments; NS and FH performed the experiments; NS, FH, C-AS, and TP analyzed data; and NS, C-AS, and TP wrote the manuscript.

Chapter 4

Direct observation of alternating stretch-coil and coil-stretch transitions of semiflexible polymers in microstructured flow

The following section has been published in:

Macromolecular Chemistry and Physics, Volume 218, 1600474, 2017
http://onlinelibrary.wiley.com/doi/10.1002/macp.201600474/full

Direct observation of alternating stretch-coil and coil-stretch transitions of semiflexible polymers in microstructured flow

Natalja Strelnikova[1], Michael Göllner[1], Thomas Pfohl[1,*]
[1]Department of Chemistry, University of Basel, Basel, Switzerland

* Correspondence: Thomas Pfohl, Biomaterials Science Center (BMC), University of Basel Gewerbestrasse 14, 4123 Allschwil, Switzerland
thomas.pfohl69@gmail.com

N. Strelnikova and M. Göllner contributed equally to this work

Keywords: non-equilibrium dynamics, actin filaments, microfluidics, buckling, bending energies

Abstract

Analyzing the behavior of semiflexible polymers experiencing hydrodynamic forces is an important step towards a better understanding of polymer dynamics in microfluidic applications as well as in living cells. In particular, studying conformational changes of fluorescently labeled, semiflexible actin filaments in flow fields of spatially varying flow strength will significantly contribute to this goal. The experimental situation is realized in flows through structured microchannels with alternating high- and low-velocity segments. While entering the wider channel segments, the semiflexible filaments undergo a buckling transition under compression whereas they are stretched with a suppression of thermal fluctuations in the extensional regime when reentering the narrow segments. The nature of these non-equilibrium and non-stationary conformational transitions is characterized by analyzing the evolution of the end-to-end distances, center-of-mass velocities and bending energies along the passage of the filaments through the channels.

4.1 Introduction

The behavior of individual macromolecular and biological filaments in confining geometries and at low Reynolds numbers microflows has apart from its fundamental relevance in biology a huge impact on materials science, biotechnology and chemical engineering[152,153]. Especially, studies of the non-equilibrium dynamics and fluctuations of semiflexible polymers, having an elastic rigidity between the extremes of floppy, flexible polymers and rigid rods, have recently attracted much attention[154,155]. Suspending semiflexible filaments in viscous fluids may lead to buckling transitions in the presence of thermal fluctuations if the hydrodynamic forces dominate over the restoring elastic forces[154–157]. These conformational instabilities far from equilibrium[158] show significant differences and new properties in comparison to equilibrium ones and can be studied experimentally[132,155,159] as well as in theoretical and simulation models[154–156,160] by analyzing the transport of semiflexible polymers in microchannel flow. A detailed understanding of these dynamic processes of semiflexible filaments is of central importance for the analysis and sorting of biologically relevant polymers, e.g. DNA[161], as well as for the description of non-Newtonian flow behavior[65,162], unusual transport in cellular flows[163] and pattern formation processes in cytoplasmic streaming[66].

Here, we study the dynamics of actin filaments in spatially structured microchannels with alternating high- and low-velocity areas. We observe a buckling of stretched semiflexible polymers as they enter the wider channel segments and a transition from a coiled to a stretched conformation while reentering the narrow constrictions from the wider segments. In detail, the impact of different flow velocities, channel geometries and filament lengths on the nature of these transitions is characterized.

4.2 Materials and Methods

4.2.1 Actin filament solution

Monomeric actin from rabbit skeletal muscle, fluorescently labeled Atto488-actin (protein/dye molar ratio of 1:0.6) as well as all buffers were purchased as lyophilized powders from Hypermol EK (Bielefeld, Germany) and reconstituted in water. A solution of 1 mg/ml actin contains 23.8 µM actin, 2 mM Tris-Cl (pH 8.2), 0.4 mM ATP, 0.1 mM dithiothreitol (DTT), 0.08 mM $CaCl_2$ and 0.2 % disaccharides and a solution of 23.8 µM Atto488-actin consists of 2 mM Tris-Cl (pH 8.2), 0.4 mM ATP, 0.1 mM DTT, 0.2 mM $CaCl_2$ and 0.4 % disaccharides. The monomix buffer for actin dilution contains 2 mM Tris-Cl (pH 8.2), 0.4 mM ATP, 0.1 mM $CaCl_2$ and 0.5 mM DTT, and the polymix buffer for actin polymerization consists of 1 M KCl, 0.1 M imidazole (pH 7.4), 10 mM ATP and 20 mM $MgCl_2$. In order to polymerize actin filaments, the stock solutions were mixed to a final composition of 3 µM actin (actin/Atto488-actin ratio 2:1), 1.4 mM ATP, 100 mM KCl, 2 mM $MgCl_2$, 0.09 mM $CaCl_2$, 0.4 mM DTT, 10 mM imidazole, 1.8 mM Tris-Cl (pH 7.4) and 0.05 % disaccharides. After about one hour at room temperature, actin monomers were polymerized into homogeneously labeled actin filaments and the solution was then diluted at a ratio of 1:10 with a buffer mixture (monomix 90% and polymix 10%) in order to enable single molecule experiments as well as to prevent interactions among filaments[16].

4.2.2 Microfluidcs platform

Microfluidic devices were designed for different channel width ratios of $A_n{:}\,A_w = 1{:}\,2$ ($A_n = 2$ µm; $A_w = 4$ µm) and $A_n{:}\,A_w = 1{:}\,4$ ($A_n = 2$ µm; $A_w = 8$ µm) and fabricated using soft lithography[131,164]. The length of the narrow and wider channel regions is $B_n = B_w = 25$ µm at a constant height of $h = 2$ µm (**Figure 4.1**). Silicon wafers (Si-Mat, Kaufering, Germany) were spin-coated with SU-8 2002 negative photoresist (Microchem, Newton, MA, USA) and exposed to ultraviolet light through a chromium mask (ML&C GmbH, Jena,

Germany) containing the desired design. The obtained master structures were then used for producing replicas in polydimethylsiloxane (PDMS, Sylgard 184, Dow Corning GmbH, Wiesbaden, Germany), which were covalently bound to a glass slide after surface activation for 30 s at 2 mbar in oxygen plasma (Harris Plasma, NY, USA). Plastic tubes were connected to the inlet and outlet of the devices and the flow was controlled by syringe pumps (Cetoni, Korbußen, Germany). To avoid interactions of the actin filaments with the walls of the microchannels, the device was rinsed by a 2 mg/ml aqueous bovine serum albumin (BSA, Sigma-Aldrich, Saint Louis, USA) solution for about 30 min and then flushed with water. The final devices were further equilibrated in water for at least one hour before as well as during the measurements in order to prevent permeation-driven flow or an increase in buffer concentration due to the permeability properties of PDMS.

4.2.3 Microscopy and image analysis

Actin filaments were observed with an Olympus IX81 inverted microscope equipped with fluorescence illumination (X-Cite Series 120 Q) and a 100 × (N.A. 1.49) UApo N oil immersion objective (Olympus, Tokyo, Japan). Images were recorded at 22 fps using a PCO Edge SensiCam (PCO AG, Kelheim, Germany) with an exposure time of 45 ms and processed as well as analyzed using ImageJ (version 1.47k, Wayne Rasband, National Institute of Health, USA) and MATLAB (R2012b, The MathWorks Inc.) by applying custom-developed scripts. In particular, skeleton lines of the filaments were obtained from the original fluorescence images by applying background subtraction, local contrast enhancement, Gaussian blurring and topological skeletonization using ImageJ[132,34]. The center-of-mass velocities, end-to-end distances and bending energies of the filaments were then determined through further analyzing the skeleton lines by means of MATLAB.
Due to the dynamics of our system, three-dimensional information about the filaments is not directly feasible through conventional scanning confocal microscopy. However, in order to calculate bending curvatures from three-dimensional coordinates, we developed a straightforward approximation

method of acquiring 3D positions from 2D fluorescence images. First, the mean intensities of pixel-value cross-sections along line segments perpendicular to the filament's two-dimensional skeleton line were calculated from the processed fluorescence images. During all experiments, the objective was focused to the center of the microchannel with respect to its height, i.e. 1 µm above the cover glass surface. As a result, the maximum fluorescence intensity along a filament's skeleton line results from a position of the corresponding filament segment at $z = 1\,\mu m$, whereas a linear decrease in intensity was found from both, a filament segment leaving the focal plane to the direction of the cover glass surface at $z = 0\,\mu m$ as well as towards the top of the channel with $z = 2\,\mu m$. In order to avoid an overestimation of filament bending in z-direction, we corrected for this effect by assuming an alternating top-down sequence of filament segments with respect to maximum fluorescence intensity. Consequently, the corrected intensity along the filament's skeleton line is henceforth directly related to its z-coordinate and scaling to the geometric boundaries of the channel height by assuming global intensity minima at $z = 0\,\mu m$ and maxima at $z = 2\,\mu m$ during the whole sequence of acquired images finally leads to the corresponding three-dimensional coordinates of a filament's conformation.

4.2.4 Computational fluid dynamics (CFD) simulations

All simulations were carried out using COMSOL Multiphysics 4.3a, a program solving partial differential equations numerically by means of the finite element method (FEM). In particular, the used mesh for the microchannels consisted of more than 100'000 elements, the fluid velocities were tuned at the inlet and the incompressible Navier Stokes equation was then solved for the geometry with no-slip boundary conditions at the walls.

4.3 Results and Discussion

4.3.1 Design of microstructured flow

Computational fluid dynamics (CFD) simulations of the velocity magnitudes in microchannels with the different aspect ratios $A_n{:}A_w$ of $1{:}4$ and $1{:}2$ are shown in **Figure 4.1a, 4.b**. The alteration of the flow velocity between the narrow and the wide channel regions is inverse proportional to the ratio of their width, $A_n{:}A_w$. Consequently, the fluid is strongly decelerated while flowing from narrow to wide regions with streamlines at the exit of the narrow segment having y-components to direction of the walls whereas it is accelerated with streamlines having y-components to the direction of the center at the passage from the wide to the narrow segments (**Figure 4.1b**). The flow in the narrow regions has an almost parabolic flow profile, whereas a plug-like velocity profile is found in the wide regions (**Figure 4.1a**).

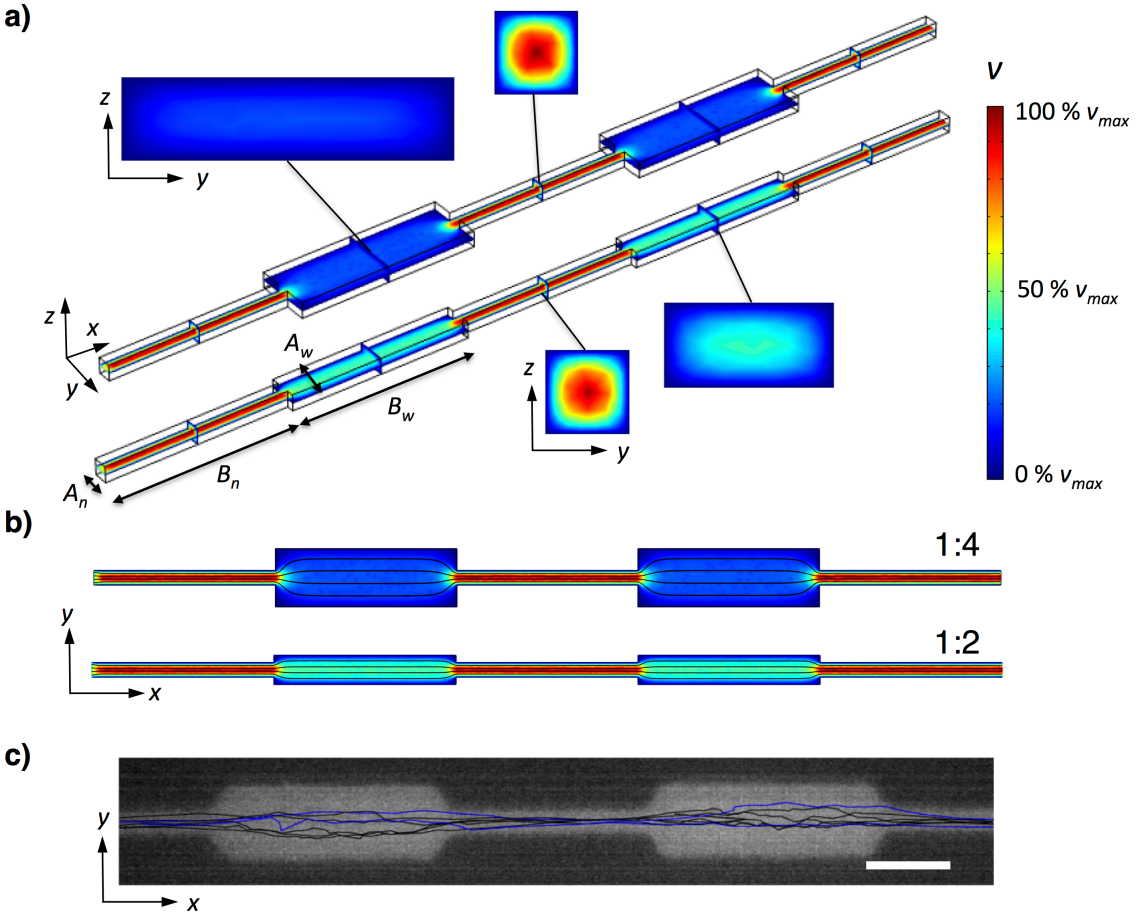

Figure 4.1: (a) CFD simulations of the (relative) velocity magnitude in channels with aspect ratios $A_n{:}A_w = 1{:}4$ and $A_n{:}A_w = 1{:}2$. The flow in the narrow regions shows an almost parabolic flow profile, whereas a plug-like velocity profile can be found in the wide regions. (b) Top (xy) view of the simulated velocity magnitude with overlaid streamlines (black lines) at the center height position (z = 1 µm). (c) Observed center-of-mass streamlines of actin filaments with lengths $L_c \approx 8 - 22$ µm in the channel with aspect ratio of 1:4. Scale bar: 10 µm.

Center-of-mass streamlines of individual fluorecently-labelled actin filaments with lengths of $L_c \approx 8 - 22$ µm for different flow rates are shown in **Figure 4.1c**. The centers-of-mass of flowing filaments have independently on their length and velocity the tendency to follow streamlines close to the center of the microchannels, both in the narrow and wide regions. However, actin filaments undergo strong flow-induced conformational changes while passing the microstructured device (**Figure 4.2**). In the narrow constrictions, the filaments are in an elongated, stretched conformation with low local curvatures whereas they start buckle while entering the wider segment with

the corresponding strong increase of local curvatures due to a flow-induced compression (**Figure 4.2a, supporting movie M1**). The nature of this compressive force can be illustrated through a moving wall model, where a semiflexible filament is pushed forward by a rigid wall, which is penetrable for the fluid and moves with a constant velocity[3]. Conversely, conformational changes of the filaments from a coiled to a stretched state occur while leaving the wider regions and reentering the narrow constrictions due to the acting extensional flow (**Figure 4.2b, supporting move M2**). Directly at the passages from the narrow to wide regions and *vice versa*, fascinating non-equilibrium conformations can be observed: single actin filaments consisting of a stretched - low local curvatures - and a buckled - high local curvatures - part (**Figure 4.2**).

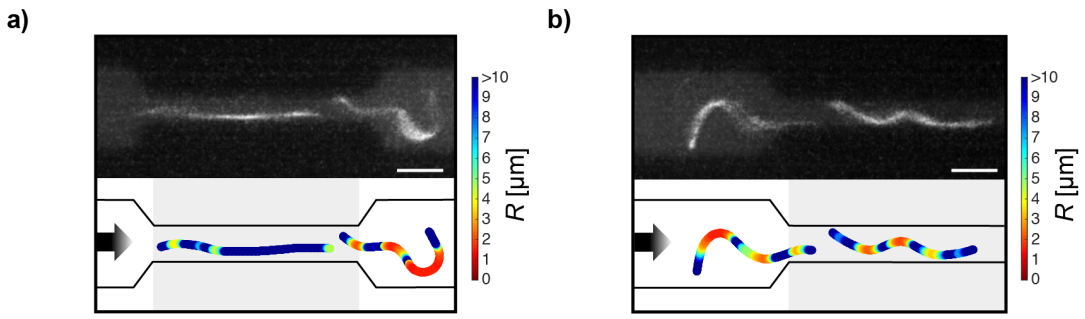

Figure 4.2: Typical flow-induced changes in the conformation of an actin filament while moving through structured microchannels. (a) Overlay of frames from a fluorescence image sequence (top) and the corresponding local curvature (bottom) of a typical stretch-coil transition while passing from the narrow to the wide segment of the channel as well as (b) during its reentering from the wide into the narrow channel region. Scale bar: 5 µm.

4.3.2 Center-of-mass velocity, end-to-end distance and bending energy

We studied the effect of different filament contour lengths L_c, fluid flow velocities q and microchannel aspect ratios $A_n{:}A_w$ on the change of the filaments' center-of-mass velocities V_{COM}, end-to-end distances R_E as well as their bending energies U_b during the flow through alternating narrow and

wide regions of the channel. The bending energy of the filaments was calculated from their contour lines as projections onto the image plane by[165]

$$U_b = \frac{1}{2} k_B T \cdot L_p \cdot \int_0^{L_c} R^{-2} ds \qquad (4.1)$$

where k_B is the Boltzmann constant, T is the absolute temperature, $L_p = 10\ \mu m$ is the persistence length of actin filaments[62,166] and R are the local radii of curvatures.

In order to investigate the influence of different contour lengths on the center-of-mass velocity, end-to-end distance and the bending energy of actin filaments during flow, the average fluid flow velocity was hold constant at about $q = 33\ \mu m/s$ in the narrow parts of the channel. In addition, the filaments were grouped into $L_c \lesssim \frac{1}{2} L_p$ (short), $L_c \approx L_p$ (intermediate) and $L_c \approx 2L_p$ (long) according to their contour length (short: $L_c = (3.1 \pm 0.9)\ \mu m$, intermediate: $L_c = (10.8 \pm 3.1)\ \mu m$, long: $L_c = (19.0 \pm 3.6)\ \mu m$. The short filaments present rigid rods, whereas the intermediate and the long filaments are described by semiflexible filaments. The center-of-mass velocities of the filaments strongly depend on their position inside the channel with a large decrease during the transition from the narrow ($A_n = 2\ \mu m$) to the wide region ($A_w = 8\ \mu m$) (**Figure 4.3a**). In particular, the short and rigid filaments are much faster compared to the semiflexible filaments especially in the narrow segment, whereas the center-of-mass velocities of the intermediate and long semiflexible filaments are similar and therefore showing no dependence on the contour length for filaments with $L_c \geq L_p$. During the movement from the narrow high-velocity into the wide low-velocity channel segment, the corresponding mean filament velocities decrease from $\langle v_n \rangle_{short} = (50.9 \pm 6.7)\ \mu m/s$ to $\langle v_w \rangle_{short} = (14.8 \pm 4.3)\ \mu m/s$ for rigid filaments, $\langle v_n \rangle_{im} = (21.4 \pm 4.1)\ \mu m/s$ to $\langle v_w \rangle_{im} = (9.5 \pm 2.6)\ \mu m/s$ for intermediate contour lengths and $\langle v_n \rangle_{long} = (22.1 \pm 4.1) \mu m/s$ to $\langle v_w \rangle_{long} = (9.1 \pm 2.1)\ \mu m/s$ for long semiflexible filaments, where $\langle v_n \rangle$ and $\langle v_w \rangle$ denote the wide and narrow regions, respectively.

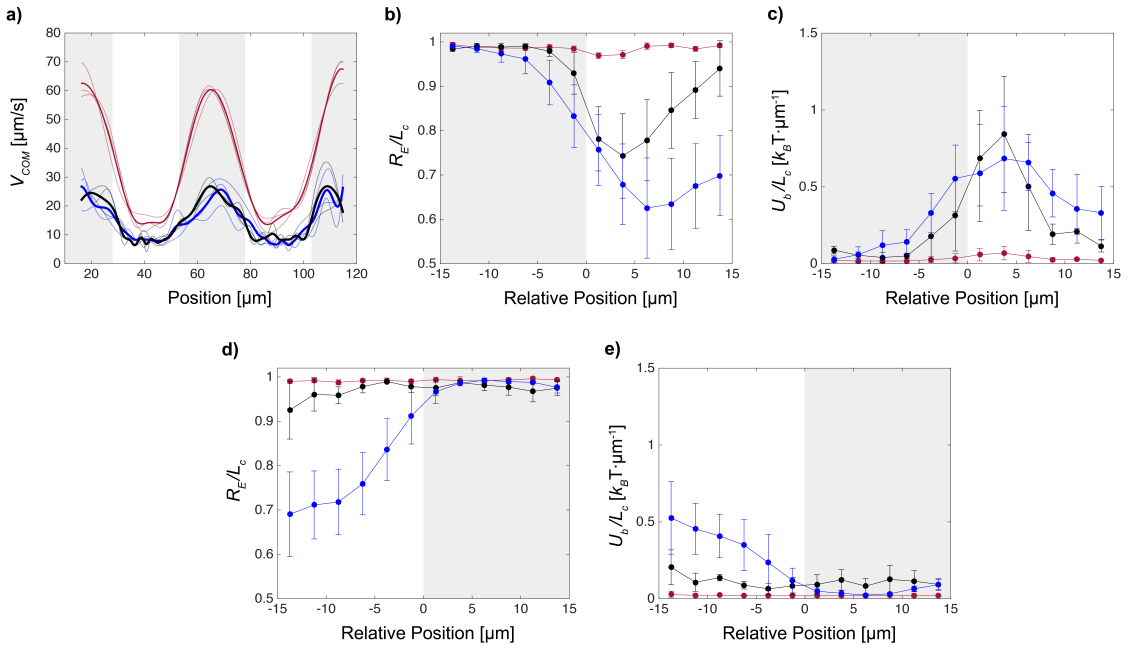

Figure 4.3: Influence of the contour length (red lines: short, black lines: intermediate, blue lines: long) on the center-of-mass velocity, end-to-end distance and bending energy of actin filaments while moving through alternating narrow (grey areas) and wide regions (white areas) of the channel. (a) The short, rigid filaments show higher center-of-mass velocities in comparison to the intermediate and long, semiflexible filaments. Evolution of the (b) end-to-end distance and the (c) length-normalized bending energy of rigid and semiflexible filaments for the movement from the narrow into the wide channel segment. Evolution of the (d) end-to-end distance and the (e) length-normalized bending energy for the movement from the wide into the narrow channel segment.

Along the passage through the alternating narrow and wide low-velocity channel segments, the short and rigid filaments do not show a change of R_E with $R_E/L_c \approx 1$ and are preferably aligned parallel to the streamlines in the narrow channel segments as well as partially rotate in the wide channel segments (**Figure 4.3b**). For the longer, semiflexible filaments in thermodynamic equilibrium, the end-to-end distance is given by[167,168]

$$R_{eq} = \sqrt{\langle {R_E}^2 \rangle} = \sqrt{2L_pL_c\left[1 - \frac{L_p}{L_c}\left(1 - e^{-L_c/L_p}\right)\right]} \qquad (4.2)$$

resulting in a corresponding length-normalized equilibrium end-to-end distance of $\left(R_{eq}/L_c\right)_{im} = 0.85 \pm 0.03$ for the intermediate and $\left(R_{eq}/L_c\right)_{long} = 0.76 \pm 0.03$ for the long contour lengths. During the flow through the narrow channel segment, the semiflexible filaments exhibit a stretched, rod-like, non-equilibrium conformation with $R_E/L_c \approx 1$ before getting subjected to the compressive force due to the difference in fluid velocity between the narrow and wide channel segment (**Figure 3b**). As a result, R_E/L_c decreases to a minimum of $(R_E/L_c)_{long} = 0.63 \pm 0.11$ for long filaments, whereas the intermediate filaments exhibit a less pronounced decrease to $(R_E/L_c)_{im} = 0.74 \pm 0.10$, which is the consequence of a larger relative stiffness L_p/L_c of intermediate filaments compared to long ones. The length-normalized bending energies U_b/L_c are not significantly increasing for the rigid filaments, whereas the intermediate show a delayed coiling with respect to their center-of-mass position as well as a faster relaxation after the stretch-coil transition compared to long filaments (**Figure 4.3c**). However, the magnitude of increase in U_b/L_c shows no difference between the intermediate and the long filaments and U_b increases from a minimum of $U_b/L_c < 0.05\ k_BT/\mu m$ for both lengths inside the narrow channel region to a maximum of $(U_b/L_c)_{long} = (0.70 \pm 0.36)\ k_BT/\mu m$ and $(U_b/L_c)_{im} = (0.84 \pm 0.37)\ k_BT/\mu m$ during flow-induced coiling. The length-normalized end-to-end distance further indicates that the period of flow through the wide region of the channel with its plug-like flow profile is sufficient for the semiflexible filaments to already relax into a conformation of $R_E/L_c \approx R_{eq}/L_c$ (**Figure 4.3d**) with a corresponding decrease in U_b/L_c (**Figure 4.3e**). Subsequently, the filaments are experiencing substantial extension from R_{eq}/L_c to stretched conformations with a suppression of fluctuations at the end of the wide channel segment as well as during the passage into the narrow region.

The effect of different fluid flow velocities q on V_{COM} during the flow of the filaments $L_c = (15.7 \pm 5.4)\ \mu m$) through the microchannel is shown in **Figure 4.4a**. The mean velocity of the filaments' center of mass in the narrow segment of the channel with an average fluid flow velocity of $q_{low} = 33\ \mu m/s$ was $\langle v_n \rangle_{low} = (21.9 \pm 3.7) \mu m/s$, decreasing to $\langle v_w \rangle_{low} = (10.1 \pm 2.5)\ \mu m/s$ in the wide region (**Figure 4a**). Increasing the average flow velocity q to $q_{high} = 108\ \mu m/s$ resulted in a large rise of $\Delta v = |\langle v_n \rangle - \langle v_w \rangle| \approx 73\ \mu m/s$,

with $\langle v_n \rangle_{high} = (113.2 \pm 29.3)\ \mu m/s$ and $\langle v_w \rangle_{high} = (40.5 \pm 14.2)\ \mu m/s$. The ratio of the average fluid flow velocity between the narrow (q_n) and the wide (q_w) segments of the channel is $q_n/q_w = A_w/A_n = 4$, and the absolute values of the extensional or the according deceleration/compression rate

$$|\epsilon| \approx \frac{2q_n}{A_w}\left(1 - \frac{A_n}{A_w}\right) \tag{4.3}$$

are $|\epsilon|_{low} \approx 6\ s^{-1}$ and $|\epsilon|_{high} \approx 20\ s^{-1}$. However, due to the interactions of the flowing actin filaments with the different flow fields in the wider channel regions (plug flow) and in the narrow channel regions (parabolic flow profile), the experimentally observed change in the center-of-mass velocities between the wide and narrow segments is smaller than the corresponding difference in average flow velocities. Although the filaments exhibiting a significantly larger rise in V_{COM} and $|\epsilon|$ when exposed to a higher average flow velocity, the length-normalized end-to-end distance shows a less pronounced difference between slow and fast filaments (**Figure 4.4b**). In particular, R_E/L_c decreases from a stretched conformation to a minimum of $(R_E/L_c)_{q_{low}} = 0.70 \pm 0.09$ for q_{low} and to $(R_E/L_c)_{q_{high}} = 0.63 \pm 0.08$ for fast average fluid flow velocities, respectively. In contrast, the filaments exposed to q_{high} are exhibiting a larger rise in U_b/L_c during the transition from the narrow into the wide channel segment, resulting from the stronger spatial change in fluid flow strength and the corresponding higher compression force (**Figure 4.4c**). Here, the length-normalized bending energy of the filaments increases during flow-induced coiling from a minimum of $U_b/L_c < 0.05\ k_BT/\mu m$ within the narrow channel segment for both q to a maximum $(U_b/L_c)_{q_{low}} = (0.74 \pm 0.33)\ k_BT/\mu m$ for the low fluid flow velocity. The length-normalized bending energy of the faster filaments exhibit a higher increase to a maximum value of $(U_b/L_c)_{q_{high}} = (2.36 \pm 0.62)\ k_BT/\mu m$, which demonstrate a strong dependence of the maximum bending energy on $|\epsilon|$. Although largely depending on the contour length, R_E/L_c shows a smaller difference between slow and fast fluid flow velocities during the filaments' flow through the wide segment of the channel and the subsequent elongation while entering the narrow channel region (**Figure 4.4d**). However, with respect to rearrangement into an entirely

stretched conformation before reentering the narrow channel segment, filaments exposed to a higher flow velocity are still experiencing significantly more deformation with $(R_E/L_c)_{q_{high}} = 0.86 \pm 0.04$ compared to $(R_E/L_c)_{q_{low}} = 0.94 \pm 0.05$ for filaments when applying q_{low}. Accordingly, the period of flowing through the wide region of the channel is not sufficient for filaments exposed to fast fluid flow velocities to relax into a lower bending energy conformation before reentering the narrow channel segment. In particular, filaments experiencing a high flow velocity are still exhibiting an elevated bending energy of $(U_b/L_c)_{q_{high}} = (0.96 \pm 0.36)\, k_BT/\mu m$ directly before getting elongated into the stretched conformation due to the passage into the narrow region of the microchannel (**Figure 4.4e**). However, due to the relaxation into a lower bending energy conformation along the passage through the wider regions, the transition from a coiled to a stretched conformation shows no symmetry to the inverse transition (stretch-coil), although both transitions occur at the same absolute rate value $|\epsilon|$ of the fluid.

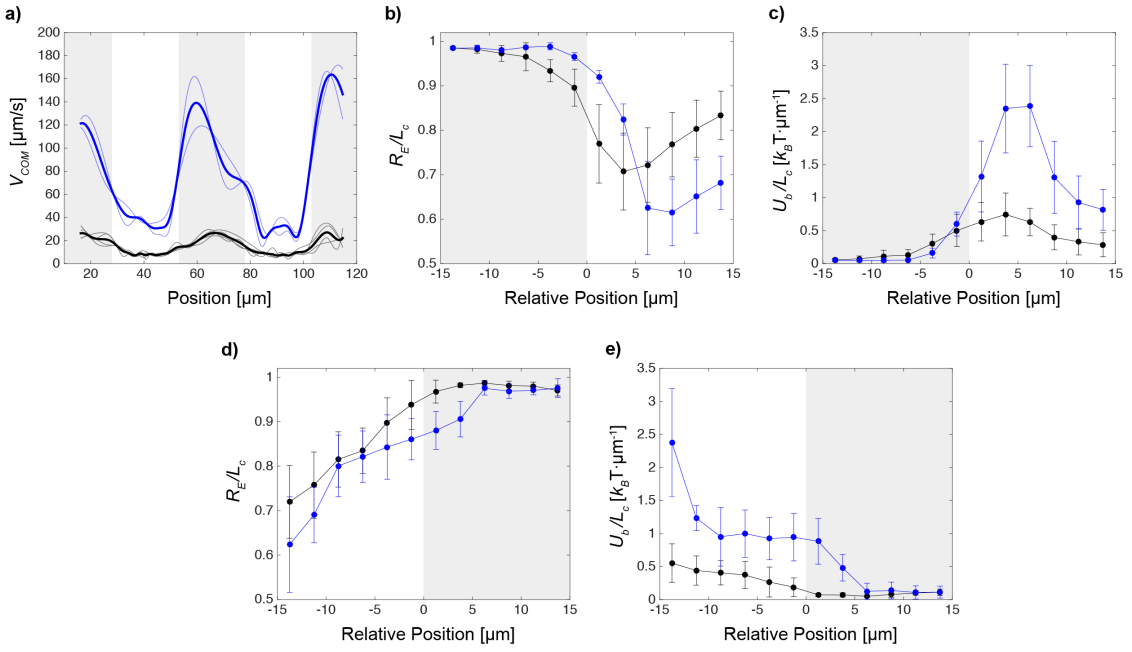

Figure 4.4: Effect of an increase in fluid flow velocity (black lines: slow, blue lines: fast) on the filaments' center-of-mass velocities, end-to-end distances and bending energies, while moving through alternating narrow (grey areas) and wide regions (white areas) of the channel. (a) Increasing the fluid flow velocity leads to a higher mean center-of-mass velocity as well as a larger relative difference between the channel segments. Dependence of the (b) end-to-end distance and the (c) length-

normalized bending energy on the fluid flow velocities during the stretch-coil transition. Influence of the fluid flow velocity on the (d) end-to-end distance and the (e) length-normalized bending energy of the filaments on the coil-stretch transition in extensional flow.

Decreasing the channel width of the wide segment to $A_w = 4\ \mu m$ allowed us to study the dependence of v, R_E and U_b on the aspect ratio of the microchannels and therefore on the confinement in the wider channel regions. The average fluid flow velocity was adjusted in order to obtain filaments with similar center-of-mass velocities in the region with the most pronounced coiling behavior, *i.e.* the wide area of the channel. Changing the aspect ratio between the narrow and the wide segments from $A_n{:}A_w = 1{:}4$ to $A_n{:}A_w = 1{:}2$ leads to a large decrease of $\Delta v \approx 21\ \mu m/s$, with $\langle v_n \rangle_{1:2} = (62.6 \pm 10.1)\ \mu m/s$ and $\langle v_w \rangle_{1:2} = (42.0 \pm 6.4)\ \mu m/s$ (**Figure 4.5a**). As a result of the smaller reduction in flow strength for the reduced aspect ratio, the magnitude of coiling while entering the low-velocity, wide channel region decreased to a corresponding less pronounced minimum in length-normalized end-to-end distance $(R_E/L_c)_{1:2} = 0.75 \pm 0.11$ in comparison to $(R_E/L_c)_{1:4} = 0.63 \pm 0.08$ (**Figure 4.5b**). Correspondingly, the filaments also exhibit a smaller rise in length-normalized bending energy to a maximum of $(U_b/L_c)_{1:2} = (1.32 \pm 0.55)\ k_B T/\mu m$ in comparison to $(U_b/L_c)_{1:4} = (2.36 \pm 0.62)\ k_B T/\mu m$ (**Figure 4.5c**). The end-to-end distance further effectively indicates the period of relaxation during the flow through the wide segment of the channel as well as the filaments' lateral positions during elongation into an almost straight, low-bending energy conformation with $(R_E/L_c)_{1:2} = 0.93 \pm 0.04$ and $(U_b/L_c)_{1:2} = (0.10 \pm 0.06)\ k_B T/\mu m$ directly before reentering into the narrow channel region (**Figure 4.5d and 4.5e**).

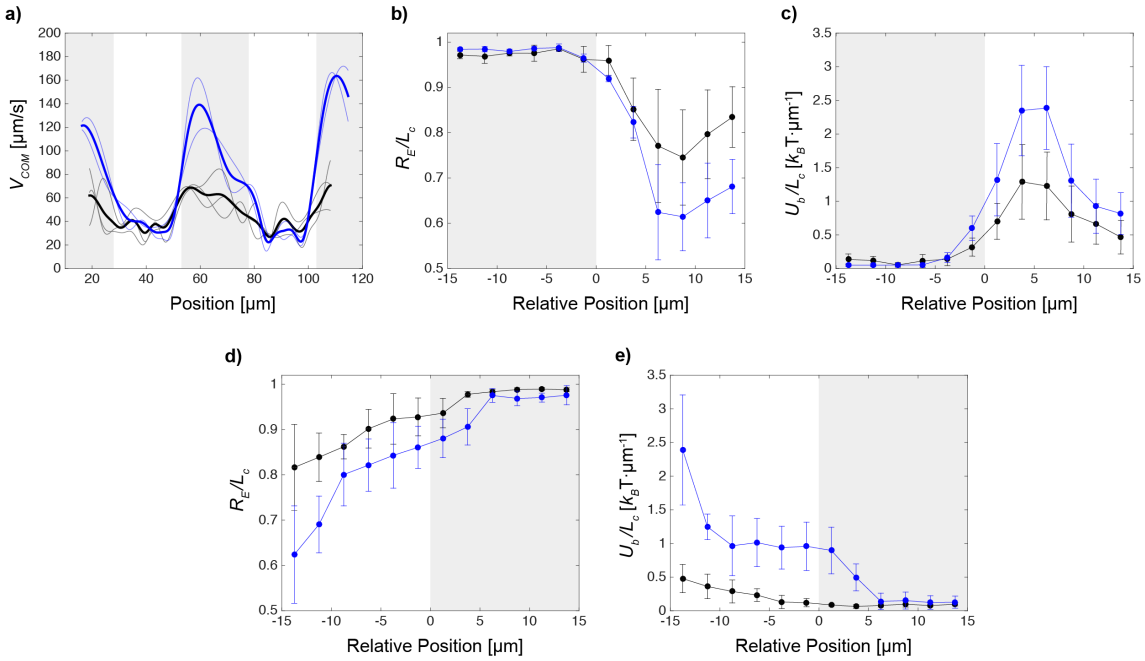

Figure 4.5: Impact of the aspect ratio between the narrow (grey areas) and wide (white areas) channel segments (black lines: 1:2, blue lines: 1:4) on the on center-of-mass velocities and bending energies of actin filaments. (a) Reduction of the aspect ratio causes a decrease in Δv between the distinct segments of the microchannels. Dependence of evolution of the (b) end-to-end distance and (c) length-normalized bending energy on the aspect ratio during the stretch-coil transition. Evolution of the (d) end-to-end distance and (e) length-normalized bending energy during the coil-stretch transition in extensional flow for different aspect ratios.

4.3.3 Bending energies calculated from *xy*-projections *vs.* obtained from 3D coordinates

A typical sequence of overlaid frames from fluorescence images of an actin filament and its corresponding projection onto the image plane of an actin filament flowing through several alternating segments of the microchannel are shown in **Figure 4.6a**. In order to obtain the bending radii of curvature from three-dimensional coordinates by taking into account the axial position of the filaments, we developed a straightforward approximation method of acquiring 3D positions from 2D fluorescence images. Using this approximation method, we were able to calculate the local radii of curvature for the sequence of the actin filament (**Figure 4.6a**). Comparing these calculated radii of curvature

with the radii obtained solely from the filaments' projections onto the image *xy*-plane show only minute differences (**Figure 4.6b**). In analogy to the bending energy obtained from the *xy*-projections, U_b was now calculated using the corresponding radii of curvature from three-dimensional coordinates and shows only a marginal difference compared to solely using the radii from the filament's projections onto the image *xy*-plane (**Figure 4.6c**). This excellent agreement in the calculated U_b results from the chosen "pseudo"-2D microfluidic setup due to the constant and to low height of the microchannels with negligible flow components into the axial *z*-direction. Consequently, our preceding analysis by using the projection of the filaments onto the image *xy*-plane[169] represents an excellent and straightforward method to study the flow-induced alternating stretch-coil and coil-stretch transitions in semiflexible actin filaments. However, using the straightforward approximation method of acquiring 3D positions, we can image a (distorted) helical coiling of the filament during hydrodynamic compression (**Figure 4.6b**, "3D") as it was described in a recent simulation study[154].

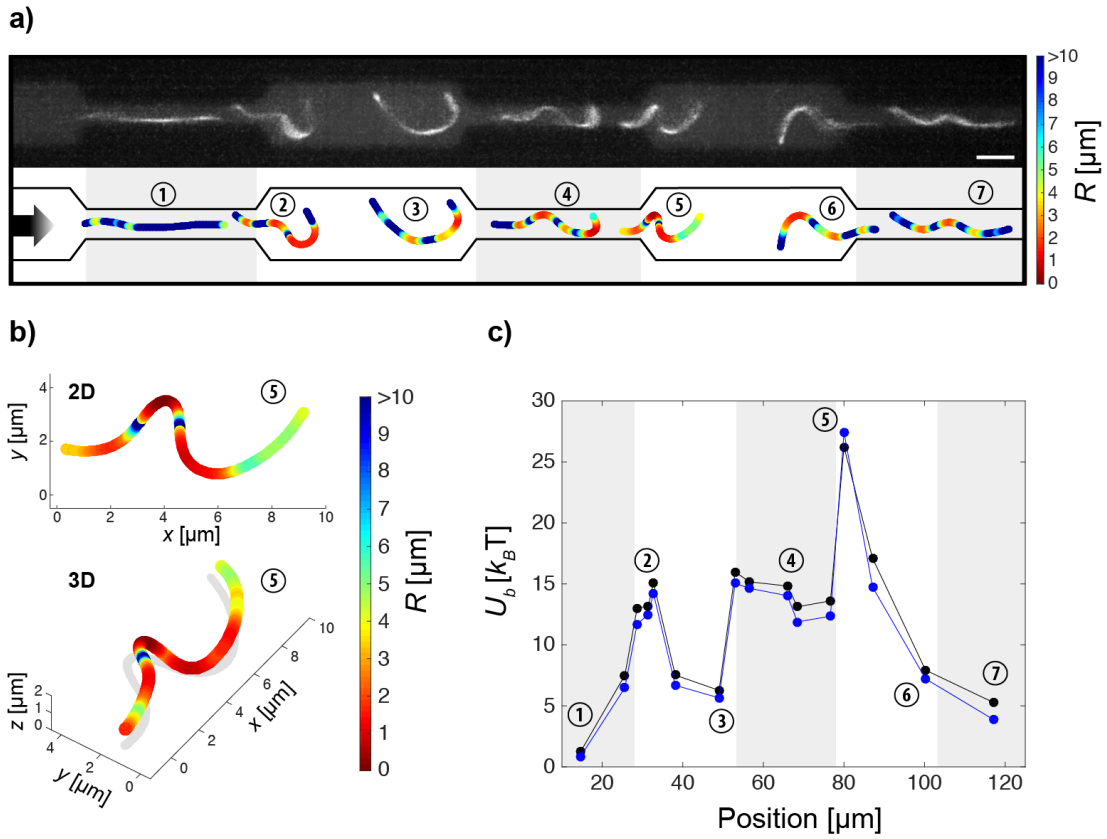

Figure 4.6: Comparison of radii of curvature obtained from *xy*-projections and from 3D coordinates with the corresponding calculated bending energy. (a) Overlay of frames from a fluorescence image sequence (top) of an actin filament and its corresponding projections onto the image *xy*-plane (bottom) while flowing through alternating segments of the microchannel. Scale bar: 5 µm. (b) Obtained radii of curvature considering solely *xy*-projections (top) and three-dimensional reconstruction of a filament's helical conformation with the obtained radii of curvature (bottom). (c) Comparison of the bending energies along the course of the moving filament through alternating narrow (grey areas) and wide (white areas) segments, using the two different calculation methods (blue line: U_b from *xy*-projections, black line: U_b from 3D approximation).

4.4 Conclusions

We experimentally studied the dynamics of actin filaments in spatially structured microchannels with alternating high- and low-velocity segments. A symmetric channel design was chosen with a similar absolute value of the

extensional and the according deceleration/compression rate $|\epsilon|$ for the fluid flow streaming from the narrow to the wide segments and *vice versa*. Short actin filaments with a length of about $L_c \lesssim \frac{1}{2} L_p$ move as rigid rods through the structured microchannels with a preferred parallel alignment to the streamlines in the narrow channel segments, whereas they are partially rotating in the wide channel segments. Longer, semiflexible filaments with lengths of about $L_p \lesssim L_c \lesssim 2L_p$ have a reduced center of mass velocity in comparison to the shorter rigid filaments. Moreover, the flowing semiflexible polymers mainly exhibit a buckling from a stretched, non-equilibrium conformation into a coiled conformation due to a compressive hydrodynamic force while entering into the wider channel segments. The acting compressive force leads to a strong deformation of the filaments, a reduction of the (length-normalized) end-to-end distances and storage of elastic energy due to the bending of the filaments. During this transition, the (length-normalized) end-to-end distance strongly depends on the contour length of the filament, whereas the magnitude of increase in (length-normalized) bending energy shows no evident dependence on the contour length. At lower fluid flow velocities, the period of flow through the wide channel segment is sufficient in order to relax from higher energy conformations to lower energy conformations by dissipating energy into the fluid. However, shorter semiflexible filaments relax faster into lower energy states in comparison to longer ones. At the passage from the wider channel segments to the narrow ones an extensional force is acting on the partially elastically relaxed filaments and a conformational transition from a coiled to a stretched state with a suppression of thermal fluctuations can be observed. Increasing the fluid flow velocity and therefore the extensional and the according deceleration/compression rate $|\epsilon|$ resulted in a large rise of the compressive hydrodynamic force at the passage from the narrow into the wide channel segments, which is associated with a strong increase of the bending energy of the filaments. Moreover, the periods of flow through the wide channel segments are shorter, and less relaxed filaments with higher bending energies experience an extensional flow at the passage from the wider to the narrow channel segments. Despite the symmetry of the microfluidic channels and a therefore similar rate of the fluid flow $|\epsilon|$ for compression and extension, the

observed stretch-coil and coil-stretch transition distinctly differ in the evolution of the conformational changes and bending energies. The observed deviation can be attributed to the relaxation and energy dissipation of the filaments at the passage through the wide segments. This asymmetry of the transitions is strongly dependent on the fluid flow velocity, the absolute value of the rate $|\epsilon|$, the aspect ratio $A_n{:}A_w$, length of wide segments B_w, the polymer length L_c, and the persistence length L_p.

In summary, our presented studies elucidate the non-Newtonian flow behavior of semiflexible filaments in specific microflows and therefore may have an impact on the analysis as well as sorting of polymers, which may consequently lead to a better understanding intercellular flows.

Supporting Information

Supporting Information, movie M1 and M2, is available from the Wiley Online Library

Acknowledgements

We thank Kathrin Hönerlage and Benjamin Bellon for their experimental support at different stages of the project, Zoe Swank for fruitful discussions and Cornelia Palivan and Wolfgang Meier for their support. Financial support by the Swiss National Science Foundation (SNF_ 200020_141270) is gratefully acknowledged.

Chapter 5

Live cell X-ray imaging of autophagic vacuoles formation and chromatin dynamics in fission yeast

The following section has been published in:

Scientific Reports, Volume 7, 13775, 2017
https://www.nature.com/articles/s41598-017-13175-9

Live cell X-ray imaging of autophagic vacuoles formation and chromatin dynamics in fission yeast

Natalja Strelnikova[1], Nora Sauter[1], Manuel Guizar-Sicairos[2], Michael Göllner[1], Ana Diaz[2], Petrina Delivani[3], Mariola Chacon[3], Iva M. Tolić[3,4], Vasily Zaburdaev[5], and Thomas Pfohl[1,6*]

[1]Department of Chemistry, University of Basel, Switzerland.
[2]Paul Scherrer Institut, Villigen, Switzerland.
[3]Max Planck Institute of Molecular Cell Biology and Genetics, Dresden, Germany.
[4]Division of Molecular Biology, Ruđer Bošković Institute, Zagreb, Croatia.
[5]Max Planck Institute for the Physics of Complex Systems, Dresden, Germany.
[6]Biomaterials Science Center, University of Basel, Switzerland.
[7]Present Address: Institute of Physics, University of Freiburg, Germany.
* Correspondence: Thomas Pfohl, Department of Chemistry, University of Basel, Klingelbergstrasse 80, Basel, 4056, Switzerland
thomas.pfohl69@gmail.com

Keywords: Schizosaccharomyces pombe, ptychography, living cells, apoptosis, chromosome oscilations.

Abstract

Seeing physiological processes at the nanoscale in living organisms without labeling is an ultimate goal in life sciences. Using X-ray ptychography, we explored *in situ* the dynamics of unstained, living fission yeast *Schizosaccharomyces pombe* cells in natural, aqueous environment at the nanoscale. In contrast to previous X-ray imaging studies on biological matter, in this work the eukaryotic cells were alive even after several ptychographic X-ray scans, which allowed us to visualize the chromatin motion as well as the autophagic cell death induced by the ionizing radiation. The accumulated radiation of the sequential scans allowed for the determination of a characteristic dose of autophagic vacuole formation and the lethal dose for fission yeast. The presented results demonstrate a practical method that opens another way of looking at living biological specimens and processes in a time-resolved label-free setting.

5.1 Introduction

Studies of nanoscale structures and dynamics of biological matter greatly benefit from observing samples in living state using label-free methods[170]. X-ray ptychography enables quantitative visualization of whole biological cells with nanoscale resolution based on the natural electron density contrast of the cell content[76,171–173]. An ideal eukaryotic model organism for cellular dynamic studies is fission yeast at the horsetail stage owing to the oscillations of meiotic chromosomes in the time scale of minutes to hours[82,83,174]. Moreover, intracellular structure changes caused by X-ray radiation are of interest for a direct analysis *in situ*[175]. The major challenge of X-ray imaging of living cellular specimens is the very low lethal radiation dose, and owing to the intense radiation damage and a low electron density contrast, sequential X-ray imaging of live eukaryotic cells was not possible so far[75,176–178]. To record sufficient information, the samples have to be exposed to a certain amount of radiation, which has to be greater than the minimum of the required dose for imaging and less than the maximum tolerable dose for the specimen[176]. The limiting factor of the resolution is therefore set by the X-ray radiation dose[176,177]. Natural, aqueous environments of biological specimens significantly decrease the electron density contrast, thus higher X-ray flux is required, which consequently increases the radiation dose needed for a given resolution[176]. Radiation induced degradation can be reduced by chemical or cryo-fixation. Using cryo-fixation, X-ray ptychography[76,77,171] and diffraction microscopy[179,180] of frozen hydrated cells were accomplished. More advanced X-ray studies were realized on initially alive cells[74,181] and appear to be a promising approach to analyze cellular processes *in situ*. Imaging of living cells simplifies sample preparation, owing to the fact that fixation steps are not required. Imaged living cells died during the first X-ray scan[74] or after a free electron laser (FEL) pulse[75], due to the lethal radiation dose. However, first electron density maps measured with X-rays of initially alive bacteria, which were obtained with less than a lethal dose, were recently presented, but due to the sample movement in the solution, the resolution of the image was depredated[78]. X-ray ptychography is a coherent diffractive imaging (CDI) technique that combines scanning microscopy with advanced phase retrieval

algorithms[182, 184]. It relies on scanning the extended sample by the X-ray beam, collecting 2D diffraction patterns from a number of overlapping regions of the specimen and a subsequent iterative reconstruction of a single projection image, which is consistent with all recorded diffraction patterns[184].

5.2 Results and Discussion

Ptychography is an X-ray imaging technique with spatial resolution limited in principle by the spatial wavelength of the incident beam and the maximum angle at which diffracted signal can be measured with sufficient signal-to-noise ratio, although in practice the resolution can be also limited by scanning precision or radiation induced damage on the specimen under study (**Figure 5.1**). In living samples, intracellular motions are happening during a single scan which can blur the images. A ptychography setup with a pinhole-defined illumination was chosen in order to achieve good contrast and high resolution with a reduced dosage of radiation (**Figure 5.1a**) due to the broad spatial spectrum[185]. We obtained reconstructed images with pixel sizes of 45×45 nm^2 and estimated resolution in the range of 100-200 nm of live cells in aqueous environment and reduced the radiation doses down to about 10^3-10^4 Gy per scan. These doses are two to three orders of magnitude less than 1.8×10^6 Gy recorded for recent X-ray images of (initially) alive eukaryotic cells[74] and close to the dose of 8.9×10^3 Gy used for holographic imaging of living bacteria[78].

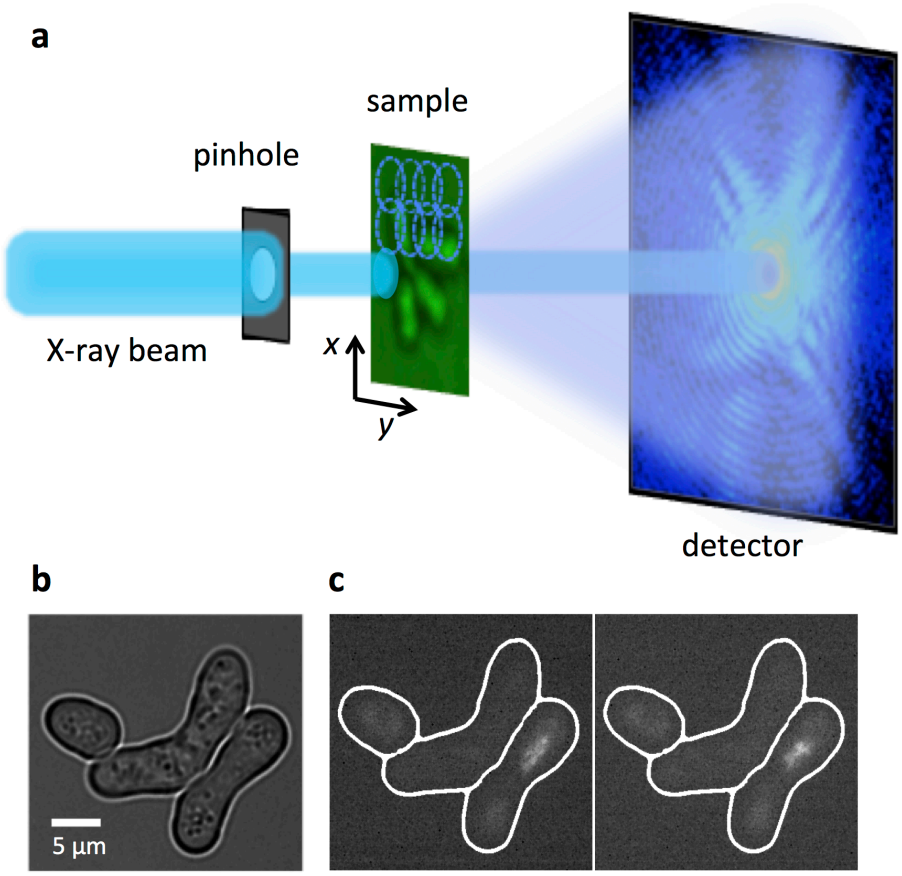

Figure 5.1: Schematic representation of the experimental ptychography setup for imaging living cells. (a) For the X-ray ptychography experiments, a monochromatic (λ = 0.2 nm) beam was used to coherently illuminate a pinhole. The cell sample was scanned to collect a series of diffraction patterns from partially overlapping illuminated regions, which allow for a robust image reconstruction. The high dynamic range and count rate of the detector allows us to record the full dynamic range of the 2D diffraction patterns at the detector and avoid a loss of low spatial-frequency information that would occur if a beamstop was used. (b) A visible light bright-field optical micrograph shows three fission *Schizosaccharomyces pombe* yeast cells under nitrogen starvation conditions, where two of them were banana-shaped zygotes. (c) Corresponding fluorescence microscopy images of the same cells as in (b) in a time interval of 5 min are shown. In order to distinguish zygotes with moving chromosomes, 'nuclear oscillations', among cells with 'non-oscillating' ones, rec25 gene was labeled with green fluorescent protein (GFP) and used as an indirect marker of DNA double strand breaks[84]. Here, only one of two zygotes was at the horsetail stage.

Here, we explore the dynamics of living fission yeast *Schizosaccharomyces pombe* cells during meiosis in natural, aqueous environment *in situ*. Fission yeast cells are ideal eukaryotic model organisms, because many of basic cellular principles and cell regulators are conserved from yeast to humans[82]. Meiosis in fission yeast is induced by depleting nitrogen sources from the culture medium and haploid cells of the opposite mating type conjugate and form a diploid "banana-shaped" zygote[83] (**Figure 5.1b,c**). At the horsetail stage of meiosis strong oscillations of chromosomes can be observed with extended periods of chromosomal back and forth motions along the cell axis[80]. The period of an individual oscillation is about 10 -15 min[83]. After several hours, at the end of the horsetail stage, the oscillations slow down and finally stop.

5.2.1 X-ray induced autophagy in fission yeast cells

X-ray ptychography micrographs of a successive image sequence of a fission yeast zygote and an analysis of the impact of ionizing radiation on the cell are shown in **Figure 5.2**. During the first four scans, no structural changes - almost homogenous density within the entire cell - of a zygote were observed. A further exposure of X-rays in the successive scans led to the appearance of clear, light and rounded structures in the zygote. These observed cellular structures may be a signature of a radiation induced formation of vacuoles[186] and autophagic bodies[85], which were described for fission yeast cells and might be a visual indication of autophagy[187 189]. These structural changes coincided with an overall positive shift in the phase shift histograms of zygote images showing autophagic vacuoles in comparison to zygote images without vacuoles (**Figure 5.2b**). Increasing the radiation dose further, a bursting of the membrane and shrinkage of the cell was observed (**Figure 5.2a-ix,x**), which demonstrates that after accumulating a certain amount of radiation the zygote perished. To characterize the dynamics of the autophagic vacuole formation and cell lysis, changes of the projected zygote area and of the projected area of individual vacuoles were analyzed (**Figure 5.2c**). In the first four ptychography scans, a slight increase of the projected area of the zygote was observed. At an accumulated dose of about 2.2×10^4 Gy (sixth scan) for the particular scan

shown in (**Figure 5.2c**), the area decreased back to its initial size and the autophagic vacuole formation set in, a first critical dose for live fission yeast cells can be defined. Applying more X-ray radiation, the initial number of vacuoles did not change, whereas their volume (projected area) increased until the cell burst. At a dose of about 9.2 × 104 Gy for this particular cell, the bursting of the cell membrane was concurred by a strong decrease of the projected zygote area. The observed formation of vacuoles can be attributed to ionizing effects of the X-ray radiation, which induce radiolysis of water and cause hydrogen peroxide (H_2O_2) and hydroxyl radical ($OH^{\cdot}$) formation[85]. These very reactive oxygen species (ROS) activate protein kinases in yeast[175] and can cause autophagy[190]. Apart from the fact that the zygote was exposed to X-rays, yeast cells grew under nitrogen depletion, which might be a stimulus to facilitate autophagy if cells starve for several hours[191]. However, the autophagic vacuole formation was observed only after several ptychography scans, and was not observed in comparable experiments using optical microscopy.

In total, nine individual live fission yeast zygotes were analyzed. The average radiation dose at which autophagic vacuole formation occurred was about $(3.30 \pm 0.74) \times 10^4$ Gy. When the radiation dosages accumulated to $(9.6 \pm 3.2) \times 10^4$ Gy, zygotes were lysed, which can be defined as the lethal radiation dose for fission yeast. Interestingly, non-meiotic cells were more resistant to X-ray radiation, where vacuole formation occurred at higher doses of $(8.7 \pm 3.8) \times 10^4$ Gy and cell death at about $(1.20 \pm 0.19) \times 10^5$ Gy, indicating that the lethal radiation dose of non-meiotic cells is similar to zygotes, whereas the vacuole formation in non-meiotic cells occurs at much higher radiation doses.

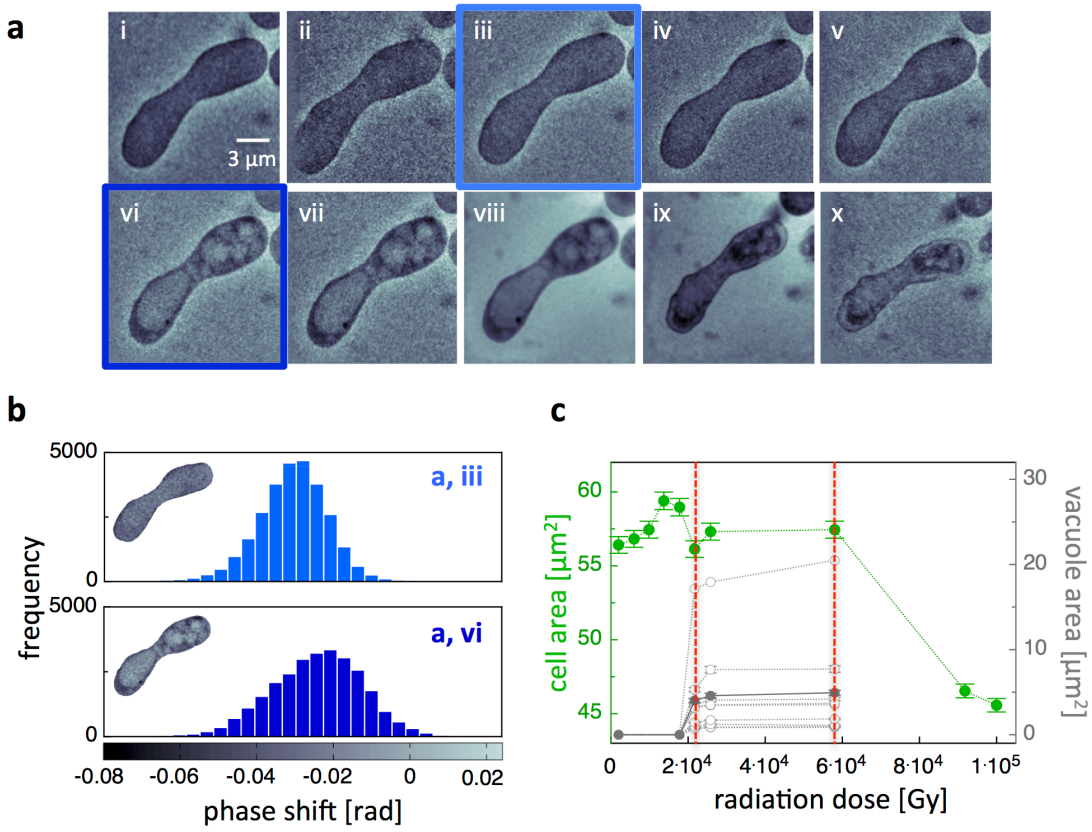

Figure 5.2: X-ray ptychography images of a live fission yeast zygote. (a) Successive image sequence of a live fission yeast zygote obtained by ptychographic CDI scans. (b) Phase shift histograms (plot of the number of pixels with a specific phase shift) of a zygote in the image without autophagic vacuoles (a, iii) and with autophagic vacuoles (a, vi). A positive shift corresponds to a lighter color. (c) Projected cell area and projected vacuole area versus the radiation dose calculated from the ptychographic zygote images. Each set of grey circles connected by a line corresponds to a different vacuole and the filled circles correspond to the mean area of the vacuoles. A characteristic dose of the onset of vacuole formation and a lethal dose can be identified (red dashed lines).

5.2.2 X-ray imaging of the chromosome motion

To further demonstrate the potential of our method for studying cellular dynamics, we imaged meiotic yeast zygote at the horsetail stage. During this stage, an extended movement of the whole chromatin happens, and at the same time, the motion matches the time scales of the X-ray imaging technique. Freshly prepared samples were firstly analyzed with a fluorescence

microscope to find a zygote at the horsetail stage in the sample and then mounted on the X-ray ptychography setup. A temporal sequence of six X-ray ptychography images of a live fission yeast zygote in the horsetail stage is presented in **Figure 5.3a**. Interestingly, a darker (a more negative phase shift) and denser structure in the top part of the zygote was observed. This structure was moving during one scan to another and furthermore changed its shape. We identified this densified structure as moving chromatin, which has the same appearance as the chromosomes in the fluorescence micrograph taken before the X-ray ptychography scans (**Figure 5.3b**). Image processed contours of the chromosomes overlaid on the original ptychography images are shown in **Figure 5.3c**. The motion of the chromosomes was analyzed by calculating their center of mass. Starting from the initial position of the chromosomes the subsequent center of mass positions showed a movement of several hundreds of nanometer away from the upper cell end in the direction of the lower part of the cell (**Figure 5.3d**). For further analysis, we compared the shape changes of the chromosomes over time by calculating the radius of gyration

$$R_g = \sqrt{\frac{1}{N}\sum_{i=1}^{N}(\vec{r}_i - \vec{r}_{CM})^2}, \tag{5.1}$$

where N is the number of pixels of the chromatin, $\vec{r}_i$ are the position vectors and $\vec{r}_{CM}$ is the center of mass of the chromosomes. The radius of gyration, which characterizes the packing and shape of the chromosomes, versus time is plotted in **Figure 5.3f**. Firstly, a looser packing of the chromosomes, bigger R_g, was observed, reaching a maximum of $R_g = (1.32 \pm 0.07)$ µm after 10 min during their motion to the lower cell end. Afterwards, R_g steadily decreased to a minimum of (0.85 ± 0.04) µm, which characterizes a strong compaction of the chromosomes. This chromosome compaction was found in conjunction with the formation of autophagic vacuoles, which could be observed after about 20 min (**Figure 5.3a**). The motion of the chromosomes was slowed down in comparison to the observed period of the oscillation of about 10 – 15 min [6]. This observed deceleration of the chromosome motion is an indication of an impact of X-ray radiation, which most probably damages the cell at the molecular level; especially the appearance of autophagic vacuoles in

concurrence with the chromosomes compaction had a strong impact on the oscillating chromosomes.

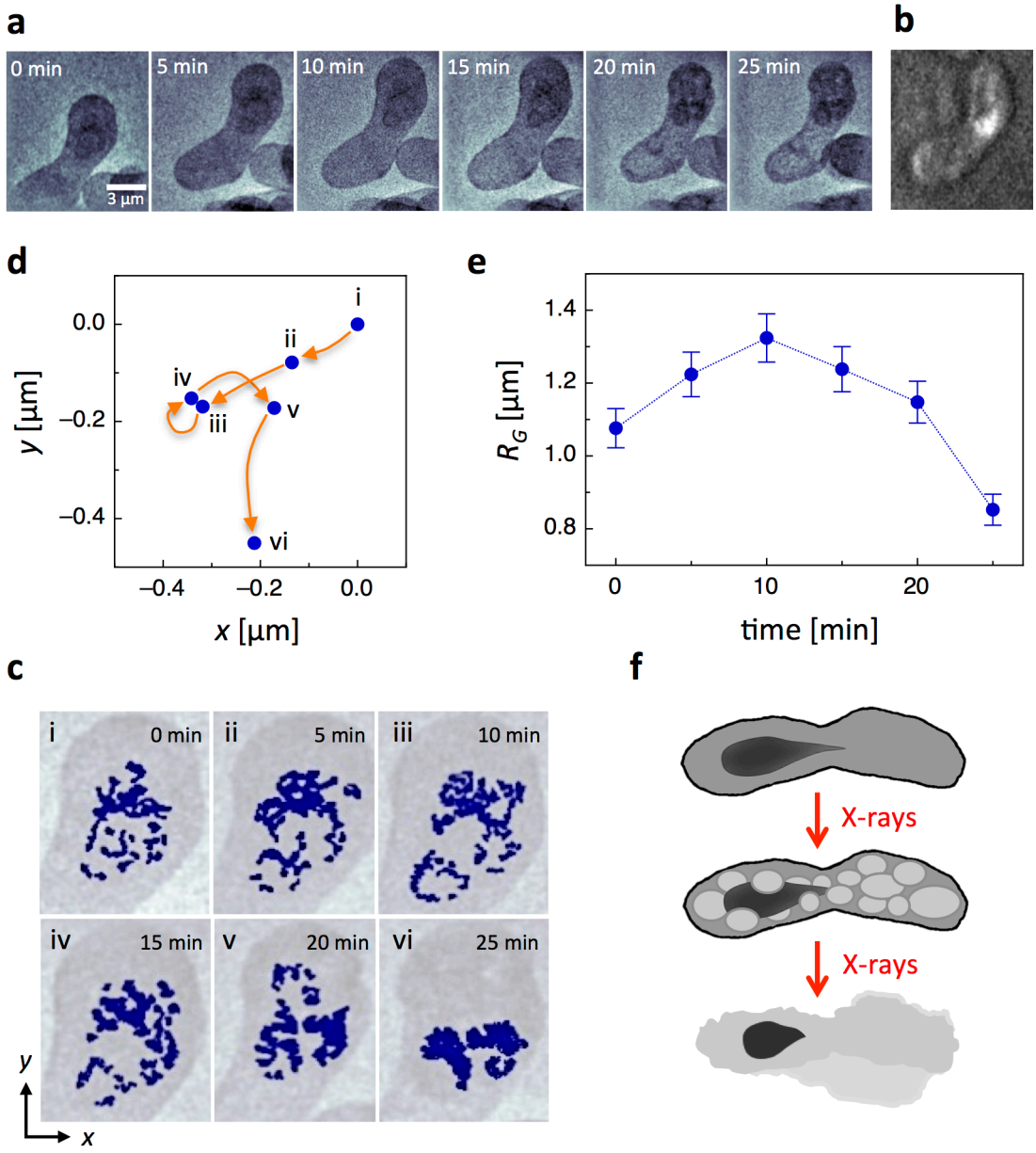

Figure 5.3: X-ray ptychography images of chromosomes motion in a live fission yeast zygote at the horsetail stage. (a) Temporal image sequence of a live zygote in the horsetail stage obtained by X-ray ptychography. (b) Fluorescence micrograph of the zygote taken before the X-ray ptychography scans. (c) Overlay of image processed contours of the chromosomes (dark blue) on the original ptychography images. (d) Center of mass motion of chromosomes between the sequential ptychographic images. The x and y-position of the center of mass of the first scan at 0 min was set to 0,0. (e) Calculated radius of gyration of the chromosomes versus time. (f) Schematic

representation of autophagic vacuoles formation and cell lysis during meiotic chromosome oscillations.

Moreover, due to a time-consuming sample preparation and mounting procedure, the X-ray ptychography images were presumably taken at the end of the horsetail period, when the oscillations slowed down. The appearance of autophagic vacuoles was observed, when the radiation dose accumulated to about 1.2×10^4 Gy. This critical dose of the vacuole formation is less than half of the critical dose, which was found for normal yeast zygotes, which might be an indication that zygotes in the horsetail stage are much more sensitive to X-ray radiation.

5.3 Conclusions

In these experiments, we optimized the sample preparation and experimental setup to successfully apply ptychography for sequential imaging producing X-ray movies of the live meiotic yeast cells in aqueous environment and established an advanced method to investigate intracellular nanostructures. Based on the natural electron density contrast, this label-free imaging method allowed us to visualize cellular structures *in situ*. We discovered autophagic cell death or type II programmed cell death[187] and cell lysis, induced by the pathological environment due to the ionizing X-ray radiation. Autophagy in the yeast and mammalian cells is similar[189] and it is considered to play an important part in the response of radiation therapy[192]. The radiation-induced damage on the molecular level most probably occurred already during the first X-ray scan, but it did not cause visible cell changes and the cell stayed alive. Thus an average radiation dose at which visible signs of autophagy occurs by formation of autophagic vacuoles[191] and a characteristic dose of membrane bursting of the eukaryotic cells can be obtained. Moreover, the dynamics of denser structures, which are most likely chromatin structures at the end of their oscillatory motion during the horsetail stage of yeast zygotes, can be imaged and analyzed. However zygotes are most likely already damaged at the molecular level by radiation. This imaging approach also simplifies sample

preparation and avoids artifact formation caused by fixation, sectioning or labeling.

We believe that improved sample environments, e.g. microfluidics setup[43] to flush fresh medium and remove free radicals[190], modified scanning protocols and adjusted ranges of interest will further advance the new, here demonstrated, way of seeing physiological processes of individual eukaryotic cells as well as tissues with subcellular, nanoscale resolution.

5.4 Materials and Methods

In order to avoid a strong background signal and to create a cytocompatible environment, we used biocompatible and X-ray resistant 200 nm thick silicon nitride (Si_3N_4) membrane windows (frame: 5×5 mm^2 $\times$ 200 µm, membrane: 1.5×1.5 mm^2 $\times$ 200 nm; Silson Ltd, Blisworth, England)[37,179,180]. The Si_3N_4 membrane windows were coated with lectin (Sigma-Aldrich, St. Louis, MO, USA) to increase cell adhesion to the membrane surface, which is crucial for the spatial stability of the cells and thus for the reproducibility of X-ray ptychography scans. Fission yeast *Schizosaccharomyces pombe* cells were kept in phosphate-buffered saline (PBS) medium at room temperature. For fluorescence optical imaging, we used the genotype of the fission yeast strain h90 rec25::GFP-KanMX6. The strain was a kind gift from C. Martín-Castellanos (CM62, IBFG, Salamanca, Spain). To induce meiosis, fission yeast cells were transferred to an Eppendorf tube with 100 µl of nutrition deficient Edinburgh minimal medium (EMM-N)[174] and kept for 30 min at room temperature. Afterwards, a small droplet of medium with cells were put on a lectin-coated Si_3N_4 membrane window and the device was covered by an uncoated Si_3N_4 membrane window and accurately glued with UHU plus epoxy quick set adhesive at the edges of the membranes. The described procedure enables the preparation of hydrated living cell samples for X-ray experiments with an intercalated aqueous film of 5 to 10 µm in thickness. The gap was determined based on bright field optical imaging where the distance between the membranes was comparable to the size of the cell as observed by changing the focus. Since the aqueous environment drastically decreases the electron

density contrast of the sample, a small sample thickness is crucial to reduce the background signal caused by the medium in the device.

X-ray ptychography experiments were performed at the coherent small-angle X-ray scattering (cSAXS) beamline of the Swiss Light Source, Paul Scherrer Institut, PSI, Villigen, Switzerland. The schematic representation of the setup is shown in **Figure 5.1a**. An X-ray beam of 6.2 keV photon energy, λ = 0.2 nm, was selected using a double crystal Si (111) monochromator. The incident beam was defined by a pinhole with a transverse diameter of about 2.5 µm in order to obtain a coherent spatially confined illumination at the sample, which was placed 3 mm downstream of the pinhole and had at the sample position approximately the same diameter. The sample of hydrated live cells was placed on a piezoelectric scanning stage to allow for nanometer precision scanning. The coherent X-ray beam diffracted by the sample propagates through a helium flushed flight tube to a photon-counting Pilatus 2D detector[193], which is located at distance of 7.412 m from the sample. The broad angular spectrum of a pinhole-defined illumination is well suited for minimizing the radiation dose while acquiring images with good contrast and a moderately high resolution[185]. Before the X-ray ptychography experiments, the cell samples were imaged by fluorescent microscopy in order to identify oscillating zygotes. The membranes were then mounted on the setup and the identified cells were positioned using an on-stage bright field microscope.

In order to avoid the raster grid pathology[194] all scans were performed following a Fermat spiral scanning pattern[195]. In order to find optimal scanning parameters, different step sizes and exposure times were applied. For the measurements in **Figure 5.2a** a scanning field of view of 18 × 14 µm^2 and an average step size of 0.7 µm were used with an exposure time of 0.1 s per scanning point. For these parameters the resolution was about 200 nm with an average flux of about 7.4 × 10^5 photons/µm^2. To calculate the average flux we first normalized the reconstructed illumination intensity using the total number of counts arriving at the detector after compensating for absorbing and scattering elements in the path of the beam, then we used the scanning pattern to generate a grid of the distribution of photons incident on the sample for the whole scan. The flux in photons/µm^2 is finally calculated by integrating over an area significantly larger than the illumination and dividing

by the area, in this manner we included in the calculation the total dose incident on the sample including the overlapping regions of the scan[196]. The corresponding dose of 3.9×10^3 Gy was estimated as described in Ref.[180]: The dose, D, is calculated based on the surface dose equation $D = \mu N_0 h\nu/\rho$[176], where the attenuation length, $1/\mu$, was obtained from tabulated values[197] assuming an average composition of $H_{128}C_{30}N_9O_{49}S_1$ and average density of ρ = 1 g cm^{-3}.

In order to observe the cell behavior (death or ability to recover) between the X-ray scans, the time interval among the images was different: 5min, 25min, 20min, 20min, 50min, 30 min, 40 min, 2h, 3h. This allows us to assume that the cell death is initiated by the X-ray radiation and does not occur/continue when the X-rays are switched off. The radiation doses used for single ptychography scans in **Figure 5.2a** were different, the 1st scan 1.96 x 10^3 Gy, 2nd scan 4.01 x 10^3 Gy, 3rd scan 3.87 x 10^3 Gy, 4th scan 3.86 x 10^3 Gy, 5th scan 4.09 x 10^3 Gy, 6th scan 3.87 x 10^3 Gy, 7th scan 4.14 x 10^3 Gy, and 10th scan 8.20 x 10^3 Gy. The quality of the images in **Figure 5.2a** (**viii**, **ix**) and resolution down to about 100 nm was improved using smaller step sizes of 0.5 µm and longer exposure times of 0.4 s, which increased the radiation dose to about 3.3×10^4 Gy.

The images in **Figure 5.3a** were obtained with an exposure time of 0.1 s per scanning point and an average step size of 1 µm. The flux at the sample position was 4.2×10^5 photons/µm^2 for the individual scans, corresponding to an estimated resolution of about 100 nm. The radiation doses per scan were 1.93 x 10^3 Gy (1st), 1.83 x 10^3 Gy (2nd), 2.71 x 10^3 Gy (3rd), 2.70 x 10^3 Gy (4th), 2.76 x 10^3 Gy (5th), and 2.74 x 10^3 Gy (6th).

Reconstructions were carried out using the maximum likelihood method through non-linear optimization[182,184]. In order to reduce the noise in the reconstructions, gradient preconditioning and regularization, as described by Thibault and Guizar-Sicairos[184], were used. A good estimate of the incident illumination is important to facilitate the reconstruction of weak contrast specimens[198], such as the hydrated live cells presented here. For this purpose we characterized the incident illumination via ptychography before the

experiments using a 2D test patterns similar to those used in[199]. The illumination phase and amplitude profile were stable for the duration of a single scan. For this case the resolution of the reconstruction could not be assessed via Fourier shell correlation (FSC)[200,201] because two identical datasets were not available due to changes or movement of the live specimens. To assess the resolution of each image we used instead a method based on the angular-averaged power spectral density (PSD) method as described in[77] .

X-ray ptychography images were analyzed using ImageJ (version 1.47k, Wayne Rasband, National Institute of Health, USA) and MATLAB (version R2012b, The MathWorks, Natick, USA) by applying custom developed scripts. The images were first denoised by conditional mean filtering resulting in an edge preserving smoothing. Further applying edge detection algorithms yield the contour of the cells, which acts as the range of interest in order to find the chromosomes by local thresholding.

Acknowledgements

X-ray measurements were carried out at the cSAXS beamline of the Swiss Light Source, Paul Scherrer Institut (PSI), Villigen, Switzerland. We thank Prof. Kurt Ballmer for the use of his fluorescence microscope at PSI during our X-ray ptychography measurements, C. Martin-Castellanos for the kind gift of the Rec25-GFP strain, Zoe Swank and Raphael Urbani for their support during synchrotron experiments. Financial support by the Swiss National Science Foundation (SNF_200020_141270) and Swiss Nanoscience Institute is gratefully acknowledged.

Author contributions:

N. S., M. G.-S., A. D., V. Z., and T. P. conceived the research work and designed the experiments. N. S., N. S. (II), M. G.-S., A. D., P. D., V. Z., and T. P. performed the experiments. P. D., M. C. and I. M. T. contributed and modified samples and protocols. N. S., M. G.-S., M. G., V. Z., and T. P. analyzed the data. N. S., M. G.-S., V. Z., and T. P. wrote the paper with contributions from all authors.

Chapter 6

Conclusions and outlook

Non-equilibrium and time resolved measurements were performed using specially designed microfluidic devices in combination with fluorescence microcopy, bright field microscopy or small-angle X-ray scattering. Additionally, we have custom-designed and successfully applied sample preparation methods for ptychographic X-ray imaging, which allowed us to measure the dynamics in living yeast cells.

In particular, we discovered actin filament formation and density distribution in KCl concentration gradients and bundle network formation in double gradients of KCl and Mg^{2+}. For these experiments, we developed a multi-height microfluidic device to generate steady state, flow-free linear and step-like gradients. The principle of the device is based on the advective transport in two flow channels, which generate diffusion in interconnected microchambers. The actin networks were examined by measuring the mesh sizes, space-dependent connectivity, and distributions of nodes, links and link lengths. Moreover, we define the local bending rigidity of the networks and their overall elasticity.

We also studied alternating stretch-coil and coil-stretch transitions of filamentous actin flowing though channels with geometric constrictions. The developed microchannels consist of repeating wide and narrow parts with symmetric alternating high- and low-velocity segments. We analyzed center of mass velocities, end-to-end distances and bending energy changes for

filaments of different length and at different fluid flow velocities. Depending on their contour length, the filaments act as rigid rods in case of short filaments, whereas longer filaments behave as semiflexible polymers. While entering into the wider channel segments, the semiflexible polymers undergo buckling from a stretched into a coiled conformation due to compressive hydrodynamic forces. Increasing the fluid flow rate in the channel leads to an increase of these forces at the entrance to the wide segment and consequently the bending energy of the filament. Furthermore, the stretch-coil and coil-stretch transitions of the filaments clearly differ in the evolution of the conformational changes due to the relaxation and energy dissipation while entering the wider channel.

Furthermore, we studied DNA compaction and decompaction using PAMAM G6 dendrimers as a histone core model protein. We measured DNA/ PAMAM G6 complex formation at different pH of the solution. The structural changes of DNA complexes were analyzed applying SAXS. Thus, at pH = 8.5 DNA / PAMAM G6 complexes have 2D hexagonal organization with the tendency towards the 3D hexagonal organization whereas at pH = 5.5 DNA and PAMAM G6 form a beads-on-a-string structure. DNA decondensation from PAMAM G6 dendrimers was initiated by the competitive interaction between DNA and heparin. The real-time dynamic evolution measurements of the reaction were performed in the X-ray compatible hydrodynamic focusing microfluidic device with a chevron/herringbone micromixer. The time evolution of the DNA / PAMAM G6 complex interactions with heparin was measured by scanning the reaction at different positions along the reaction channel. We detected the changes of the scattering curves and in particular the variation of the form factor. Applying the Guinier approximation, we further measured the shape of the complex through the radius of gyration R_g, where an increase in R_g indicates DNA release from cationic dendrimers and formation of dendrimer/heparin complexes.

Moreover, in this thesis, we studied live cell X-ray imaging and analyzed the chromatin dynamics and autophagic vacuoles formation in fission yeast. We obtained several sequences of X-ray images of individual living fission yeast cells by using optimized X-ray ptychography parameters (step size, exposure time) and improved sample preparation technique. Hence, we generated X-ray movies of living yeast cells, which allowed us to investigate intracellular

nanostructures *in situ*. Applying X-ray ptychography with pinhole-defined illumination and low dose of about 10^3 Gy, we achieved hundreds of μm^2 field of view 2D images with pixel sizes of 45×45 nm^2 of live cells in an aqueous environment. This label-free imaging technique allowed us to directly visualize cellular structures and to study the dynamics of chromosomal movements and densification during the horsetail stage of yeast zygotes. Furthermore, we discovered autophagic vacuole formation and cell death, induced by the ionizing X-ray radiation. We estimated the average radiation doses of the beginning of the autophagic vacuoles formation as well as the dose of the cell membrane bursting. Moreover, the developed sample preparation technique is simplified and avoids artifact formation caused by fixation, sectioning or labeling.

Fluids containing actin filaments can be considered as non-Newtonian fluids and can be analyzed in different channel geometries in future investigations. These studies might clarify the non-Newtonian flow behavior in various structured microchannel and therefore lead to even better understanding of intercellular flows. The concentration gradient technique has a potential to generate a wide range of structures. Thus, it can be applied to perform different experiments and study other material interactions, including different ion concentration gradients and different biopolymer formation, e.g., microtubules. The properties of the microfluidic devices can be also extended to the combination with advanced microscopy, spectro-microscopy, or X-ray nanoscattering and imaging. Furthermore, the combination of SAXS and fast mixing microfluidic devices is a promising tool for direct measurements of the dynamic changes of the biomimetic systems in time-resolved manner at the nanometer scale, which may be used to study additional relevant biophysical problems. The X-ray ptychography imaging technique can be applied for unstained living cell visualization. In combination with microfluidic devices, which will remove free radicals by flushing of the system with fresh medium, the cells might stay alive under X-ray radiation for even longer times.

References

1. Bahr, B., Lemmer, B. & Piccolo, R. *Quirky Quarks*. (2016). doi:10.1007/978-3-662-49509-4

2. Dominguez, R. & Holmes, K. C. Actin Structure and Function. *Annu Rev Biophys* **40,** 169–186 (2011).

3. Arber, S. *et al.* Regulation of actin dynamics through phosphorylation of cofilin by LIM-kinase. *Nature* **393,** 805–9 (1998).

4. Steinhauser, D. R. Actin Filaments and Bundles in Flow. (University of Göttingen, 2008).

5. Olson, E. N. & Nordheim, A. Linking actin dynamics and gene transcription to drive cellular motile functions. *Nat. Rev. Mol. Cell Biol.* **11,** 353–65 (2010).

6. Lodish, H. *et al. Molecular Cell Biology*. (W. H. Freeman, 2000).

7. Buccione, R., Orth, J. D. & McNiven, M. A. Foot and mouth: podosomes, invadopodia and circular dorsal ruffles. *Nat. Rev. Mol. Cell Biol.* **5,** 647–57 (2004).

8. Linder, S. The matrix corroded: podosomes and invadopodia in extracellular matrix degradation. *Trends Cell Biol.* **17,** 107–117 (2007).

9. Pellegrin, S. & Mellor, H. Actin stress fibres. *J. Cell Sci.* **120,** 3491–3499 (2007).

10. Palmer, A., Xu, J. & Wirtz, D. High-frequency viscoelasticity of crosslinked actin filament networks measured by diffusing wave spectroscopy. *Rheol. Acta* **37,** 97–106 (1998).

11. Gittes, F., Mickey, B., Nettleton, J. & Howard, J. Flexural rigidity of microtubules and actin filaments measured from thermal fluctuations in shape. *J. Cell Biol.* **120,** 923–934 (1993).

12. Gardel, M. L. *et al.* Elastic behavior of cross-linked and bundled actin networks. *Science* **304,** 1301–1305 (2004).

13. Barkley, M. D. & Zimm, B. H. Theory of twisting and bending of chain macromolecules; analysis of the fluorescence depolarization of DNA. *J. Chem. Phys.* **70,** 2991 (1979).

14. Alberts, B. *et al. Molecular Biology of the Cell*. (2014).

15. Wilhelm, J. & Frey, E. Radial distribution function of semiflexible polymers. *Phys. Rev. Lett.* **77,** 2581 2584 (1996).

16. Diamant, H. & Andelman, D. Binding of molecules to DNA and other semiflexible polymers. *Phys. Rev. E* **61,** 6740 6749 (2000).

17. Garcia, H. G. *et al.* Biological Consequences of Tightly Bent DNA: The Other Life Biological Consequences of Tight. *Biopolymers* **85,** 115 130 (2006).

18. Schiessel, H. The physics of chromatin. *J. Phys. Condens. Matter* **60301,** 90 (2003).

19. Henzel, J. V. *et al.* An asymmetric chromosome pair undergoes synaptic adjustment and crossover redistribution during Caenorhabditis elegans meiosis: Implications for sex chromosome evolution. *Genetics* **187,** 685 699 (2011).

20. Berg, J., Tymoczko, J. & Stryer, L. *Biochemistry (Fifth Edition)*. (W.H. Freeman and company, 2002).

21. Koster, S. F. Biological Matter in Microfluidic Environment - from Single Molecules to Self-Assembly. (University of Göttingen, 2006).

22. Henrik Bruus. *Theoretical Microfluidics*. (Oxford University Press, 2008).

23. Squires, T. M. & Quake, S. R. Microfluidics: Fluid physics at the nanoliter scale. *Rev. Mod. Phys.* **77,** 977 1026 (2005).

24. Whitesides, G. M. The origins and the future of microfluidics. *Nature* **442,** 368 373 (2006).

25. Deshpande, S. Dynamics of Emerging Actin Networks. (Universität Basel, 2013).

26. Weibel, D. B. *et al.* Torque-actuated valves for microfluidics. *Anal. Chem.* **77,** 4726 4733 (2005).

27. Hong, J. W. & Quake, S. R. Integrated nanoliter systems. *Nat. Biotechnol.* **21,** 1179 1183 (2003).

28. Nguyen, N.-T. & Wu, Z. Micromixers a review. *J. Micromechanics Microengineering* **15,** R1 R16 (2005).

29. Williams, M. S., Longmuir, K. J. & Yager, P. A practical guide to the staggered herringbone mixer. *Lab Chip* **8,** 1121 1129 (2008).

30. Witzigmann, D. *et al.* Encapsulation of Gold Nanoparticles to Visualize Intracellular Localization of Lipid and Polymer-Based Nanocarriers. *Sci. Speak.* 10 12 (2015).

31. Laser, D. J. & Santiago, J. G. A review of micropumps. *J. Micromechanics Microengineering* **14,** R35–R64 (2004).

32. Thangawng, A. L., Howell, P. B., Richards, J. J., Erickson, J. S. & Ligler, F. S. A simple sheath-flow microfluidic device for micro/nanomanufacturing: fabrication of hydrodynamically shaped polymer fibers. *Lab Chip* **9,** 3126–3130 (2009).

33. Dootz, R., Otten, A., Köster, S., Struth, B. & Pfohl, T. Evolution of DNA compaction in microchannels. *J. Phys. Condens. Matter* **18,** S639–S652 (2006).

34. Köster, S., Steinhauser, D. & Pfohl, T. Brownian motion of actin filaments in confining microchannels. *J. Phys. Condens. Matter* **17,** S4091 (2005).

35. Strelnikova, N., Göllner, M. & Pfohl, T. Direct Observation of Alternating Stretch-Coil and Coil-Stretch Transitions of Semiflexible Polymers in Microstructured Flow. *Macromol. Chem. Phys.* **218,** 1600474 (2017).

36. Jégou, A. & Romet-Lemonne, G. Single Filaments to Reveal the Multiple Flavors of Actin. *Biophys. J.* **110,** 2138–2146 (2016).

37. Weinhausen, B. & Köster, S. Microfluidic devices for X-ray studies on hydrated cells. *Lab Chip* **13,** 212–215 (2012).

38. Chung, B. G. & Choo, J. Microfluidic gradient platforms for controlling cellular behavior. *Electrophoresis* **31,** 3014–3027 (2010).

39. Wu, Z., Willing, B., Bjerketorp, J., Jansson, J. K. & Hjort, K. Soft inertial microfluidics for high throughput separation of bacteria from human blood cells. *Lab Chip* **9,** 1193–9 (2009).

40. Boedicker, J. Q., Li, L., Kline, T. R. & Ismagilov, R. F. Detecting bacteria and determining their susceptibility to antibiotics by stochastic confinement in nanoliter droplets using plug-based microfluidics. *Lab Chip* **8,** 1265–1272 (2008).

41. Carugo, D., Bottaro, E., Owen, J., Stride, E. & Nastruzzi, C. Liposome production by microfluidics: potential and limiting factors. *Nature* (2016).

42. Dootz, R., Evans, H., Köster, S. & Pfohl, T. Rapid prototyping of X-ray microdiffraction compatible continuous microflow foils. *Small* **3,** 96–100 (2007).

43. Köster, S. & Pfohl, T. X-Ray Studies of Biological Matter in Microfluidic Environments. *Mod. Phys. Lett. B* **26,** 1230018 (2012).

44. Paar, A. *The SAXS Guide*. (Anton Paar GmbH, 2011).

45. Huang, X. *et al.* Soft X-Ray Diffraction Microscopy of a Frozen Hydrated Yeast Cell. *Phys. Rev. Lett.* **103,** 1 4 (2009).

46. Evans, H. M., Dootz, R., Köster, S., Struth, B. & Pfohl, T. X-ray microdiffraction on flow-controlled biomolecular assemblies. *Bull. Pol. Acad. Sci. Tech. Sci.* **55,** 217 227 (2007).

47. Otten, A., Köster, S., Struth, B., Snigirev, A. & Pfohl, T. Microfluidics of soft matter investigated by small-angle X-ray scattering. *J. Synchrotron Radiat.* **12,** 745 750 (2005).

48. Brennich, M. E. *et al.* Dynamics of intermediate filament assembly followed in micro-flow by small angle X-ray scattering. *Lab Chip* **11,** 708 716 (2011).

49. Silva, B. F. B. *et al.* Nematic director reorientation at solid and liquid interfaces under flow: Saxs studies in a microfluidic device. *Langmuir* **31,** 4361 4371 (2015).

50. Moulin, J. F., Roth, S. V. & Müller-Buschbaum, P. Flow at interfaces: A new device for x-ray surface scattering investigations. *Rev. Sci. Instrum.* **79,** (2008).

51. Reich, C., Hochrein, M. B., Krause, B. & Nickel, B. A microfluidic setup for studies of solid-liquid interfaces using x-ray reflectivity and fluorescence microscopy. *Rev. Sci. Instrum.* **76,** (2005).

52. Toft, K. N. *et al.* High-throughput small angle X-ray scattering from proteins in solution using a microfluidic front-end. *Anal. Chem.* **80,** 3648 3654 (2008).

53. Urbani, R., Westermeier, F., Banusch, B., Sprung, M. & Pfohl, T. Brownian and advective dynamics in microflow studied by coherent X-ray scattering experiments. *J. Synchrotron Radiat.* **23,** 1401 1408 (2016).

54. Toma, A. C., Dootz, R. & Pfohl, T. Analysis of complex fluids using microfluidics: the particular case of DNA/polycations assemblies. *J. Phys. D. Appl. Phys.* **46,** 114001 (2013).

55. Pfohl, T. *et al.* Highly packed and oriented DNA mesophases identified using in situ microfluidic x-ray microdiffraction. *Biomacromolecules* **8,** 2167 2172 (2007).

56. Pollack, L. *et al.* Compactness of the denatured state of a fast-folding protein measured by submillisecond small-angle x-ray scattering. *Proc. Natl. Acad. Sci.* **96,** 10115–10117 (1999).

57. Martin, H. P. *et al.* Complex fluids under microflow probed by SAXS: rapid microfabrication and analysis. *J. Phys. Conf. Ser.* **247,** 12050 (2010).

58. Martin, H. P. *et al.* Microfluidic processing of concentrated surfactant mixtures: online SAXS, microscopy and rheology. *Soft Matter* **12,** 1750–1758 (2016).

59. Trebbin, M. *et al.* Anisotropic particles align perpendicular to the flow direction in narrow microchannels. *Proc. Natl. Acad. Sci. U. S. A.* **110,** 6706–11 (2013).

60. Stehle, R., Goerigk, G., Wallacher, D., Ballauff, M. & Seiffert, S. Small-angle X-ray scattering in droplet-based microfluidics. *Lab Chip* **13,** 1529 (2013).

61. Marmiroli, B. *et al.* Experimental set-up for time resolved small angle X-ray scattering studies of nanoparticles formation using a free-jet micromixer. *Nucl. Instruments Methods Phys. Res.* **268,** 329–333 (2010).

62. Houches, L. *Physics of Bio-Molecules and Cells*. (2001).

63. Vidula, M., Du, Y., Shim, J., Lo, E. & Khademhosseini, A. Generating spatially and temporally controllable long-range concentration gradients in a microfluidic device. *Bioeng. Proc. Northeast Conf.* **9,** (2009).

64. Atencia, J., Morrow, J. & Locascio, L. E. The microfluidic palette: A diffusive gradient generator with spatio-temporal control. *Lab Chip* **9,** 2707 (2009).

65. Kirchenbuechler, I., Guu, D., Kurniawan, N. a., Koenderink, G. H. & Lettinga, M. P. Direct visualization of flow-induced conformational transitions of single actin filaments in entangled solutions. *Nat. Commun.* **5,** 1–8 (2014).

66. Woodhouse, F. G. & Goldstein, R. E. Cytoplasmic streaming in plant cells emerges naturally by microfilament self-organization. *Proc. Natl. Acad. Sci. U. S. A.* **110,** 14132–7 (2013).

67. Widom, J. Structure, dynamics, and function of chromatin in vitro. *Annu. Rev. Biophys. Biomol. Struct.* **27,** 285–327 (1998).

68. Esfand, R. & Tomalia, D. A. Poly(amidoamine) (PAMAM) dendrimers: From biomimicry to drug delivery and biomedical applications. *Drug Discov. Today* **6,** 427–436 (2001).

69. Svergun, D. I. & Koch, M. H. Small-angle scattering studies of biological macromolecules in solution. *Rep.Prog.Phys.* **66,** 1735 1782 (2003).

70. Shields, A. R. *et al.* Hydrodynamically directed multiscale assembly of shaped polymer fibers. *Soft Matter* **8,** 2656 2660 (2012).

71. Witte, S., Tenner, V. T., Noom, D. W. & Eikema, K. S. Lensless diffractive imaging with ultra-broadband table-top sources: from infrared to extreme-ultraviolet wavelengths. *Light Sci. Appl.* **3,** e163 (2014).

72. Marchesini, S. A unified evaluation of iterative projection algorithms for phase retrieval. *Rev. Sci. Instrum.* **78,** (2007).

73. Fienup, J. R. Phase retrieval algorithms: a comparison. *Appl. Opt.* **21,** 2758 2769 (1982).

74. Weinhausen, B. *et al.* Scanning X-ray nanodiffraction on living eukaryotic cells in microfluidic environments. *Phys. Rev. Lett.* **112,** 88102 (2014).

75. van der Schot, G. *et al.* Imaging single cells in a beam of live cyanobacteria with an X-ray laser. *Nat. Commun.* **6,** 5704 (2015).

76. Diaz, A. *et al.* Three-dimensional mass density mapping of cellular ultrastructure by ptychographic X-ray nanotomography. *J. Struct. Biol.* **192,** 461 469 (2015).

77. Giewekemeyer, K. *et al.* Quantitative biological imaging by ptychographic x-ray diffraction microscopy. *Proc. Natl. Acad. Sci. U. S. A.* **107,** 529 534 (2010).

78. Bartels, M., Krenkel, M., Haber, J., Wilke, R. N. & Salditt, T. X-Ray Holographic Imaging of Hydrated Biological Cells in Solution. *Phys. Rev. Lett.* **114,** 48103 (2015).

79. Ding, D. Q., Chikashige, Y., Haraguchi, T. & Hiraoka, Y. Oscillatory nuclear movement in fission yeast meiotic prophase is driven by astral microtubules, as revealed by continuous observation of chromosomes and microtubules in living cells. *J Cell Sci* **111,** 701 712 (1998).

80. Vogel, S. K., Pavin, N., Maghelli, N., Jülicher, F. & Tolić-Nørrelykke, I. M. Self-organization of dynein motors generates meiotic nuclear oscillations. *PLoS Biol.* **7,** 918 928 (2009).

81. Ding, D. Q., Yamamoto, A., Haraguchi, T. & Hiraoka, Y. Dynamics of homologous chromosome pairing during meiotic prophase in fission yeast. *Dev. Cell* **6,** 329 341 (2004).

82. Patterson, J. O., Swaffer, M. & Filby, A. An Imaging Flow Cytometry-based approach to analyse the fission yeast cell cycle in fixed cells. *Methods* **82,** 74 84 (2015).

83. Chikashige, Y. *et al.* Telomere-led premeiotic chromosome movement in fission yeast. *Science* **264,** 270 273 (1994).

84. Fowler KR, Gutiérrez-Velasco S, Martín-Castellanos C, Smith, G. R. Protein Determinants of Meiotic DNA Break Hotspots. *Mol Cell* **49,** 983 996 (2014).

85. Li, L., Ishdorj, G. & Gibson, S. B. Reactive oxygen species regulation of autophagy in cancer : Implications for cancer treatment. *Free Radic Biol Med* **53,** 1399 1410 (2012).

86. van Holde, K. E. *Chromatin*. (Springer, 1989).

87. Subirana, J. a & Soler-Lopez, M. Cations as hydrogen bond donors: a view of electrostatic interactions in DNA. *Annu. Rev. Biophys. Biomol. Struct.* **32,** 27 45 (2003).

88. Manning, G. S. Electrostatic free energies of spheres, cylinders, and planes in counterion condensation theory with some applications. *Macromolecules* **40,** 8071 8081 (2007).

89. Morita, M., Tasaka, M. & Fujisawa, H. DAN Packing ATPase of Bacteriophage T3. *Virology* **193,** 748 752 (1993).

90. Ajdari, A., Prost, J. & Ju, F. Modeling molecular motors. *Rewiews Mod. Phys.* **69,** 1269 1281 (1997).

91. Wolf, S. G. *et al.* DNA protection by stress-induced biocrystallization. *Nature* **400,** 83 85 (1999).

92. Grant, R. A., Filman, D. J., Finkel, S. E., Kolter, R. & Hogle, J. M. The crystal structure of Dps, a ferritin homolog that binds and protects DNA. *Nat. Struct. Biol.* 294 303 (1998).

93. Dootz, R. Tuning DNA Compaction. (University of Basel, 2008).

94. Richmond, T. J. & Davey, C. A. The structure of DNA in the nucleosome core. *Nature* **423,** 145 150 (2003).

95. Woodcock, C. L., Skoultchi, A. I. & Fan, Y. Role of linker histone in chromatin structure and function: H1 stoichiometry and nucleosome repeat length. *Chromosom. Res.* **14,** 17 25 (2006).

96. Caracciolo, G. *et al.* Self-assembly of cationic liposomes-DNA complexes: A structural and thermodynamic study by EDXD. *Chem. Phys. Lett.* **351,** 222 228 (2002).

97. Mascotti, D. P. & Lohman, T. M. Thermodynamic extent of counterion release upon binding oligolysines to single-stranded nucleic acids. *Proc. Natl. Acad. Sci. U. S. A.* **87,** 3142 3146 (1990).

98. Phillips, R., Konde, J., Theriot, J. & Orme, N. *Physical Biology of the Cell. Garland Science* (Garland Science, 2008).

99. Felsenfeld, G. Chromatin unfolds. *Cell* **86,** 13 19 (1996).

100. Tomalia, D. a, Reyna, L. a & Svenson, S. Dendrimers as multi-purpose nanodevices for oncology drug delivery and diagnostic imaging. *Biochem. Soc. Trans.* **35,** 61 67 (2007).

101. Braun, C. S. *et al.* Structure/function relationships of polyamidoamine/DNA dendrimers as gene delivery vehicles. *J. Pharm. Sci.* **94,** 423 436 (2005).

102. Lee, I., Athey, B. D., Wetzel, a W., Meixner, W. & Baker, J. R. Structural molecular dynamics studies on polyamidoamine dendrimers for a therapeutic application: Effects of pH and generation. *Macromolecules* **35,** 4510 4520 (2002).

103. Nisato, G., Ivkov, R. & Amis, E. J. Size invariance of polyelectrolyte dendrimers. *Macromolecules* **33,** 4172 4176 (2000).

104. Majoros, J., Myc, A., Thomas, T., Mehta, C. B. & Baker, J. R. PAMAM Dendrimer-Based Multifunctional Conjugate for Cancer Therapy : Synthesis , Characterization , and Functionality. *Biomacromolecules* **7,** 572 579 (2006).

105. Kurtoglu, Y. E., Mishra, M. K., Kannan, S. & Kannan, R. M. Drug release characteristics of PAMAM dendrimer-drug conjugates with different linkers. *Int. J. Pharm.* **384,** 189 194 (2010).

106. Pack, D. W., Hoffman, A. S., Pun, S. & Stayton, P. S. Design and development of polymers for gene delivery. *Nat. Rev. Drug Discov.* **4,** 581 93 (2005).

107. Dufès, C., Uchegbu, I. F. & Schätzlein, A. G. Dendrimers in gene delivery. *Adv. Drug Deliv. Rev.* **57,** 2177 2202 (2005).

108. Huang, R.-Q. *et al.* Efficient gene delivery targeted to the brain using a transferrin-conjugated polyethyleneglycol-modified polyamidoamine dendrimer. *FASEB J.* **21,** 1117 1125 (2007).

109. Anderson, F. & Record, M. T. Polyelectrolyte theories and their applications to DNA. *Ann. Rev. Phys. Chem.* **33,** 191 222 (1982).

110. Glatter, O. & Kratky, O. *Small Angle X-ray Scattering*. (Academic Press INC, 1982).

111. Glatter, O. Determination of particle-size distribution functions from small-angle scattering data by means of the indirect transformation method. *J. Appl. Crystallogr.* **13,** 7 11 (1980).

112. Bracewell, R. N. *The Fourier Transform and applications*. (McGraw Hill, 1965).

113. Toma, A. C. & Pfohl, T. Small-Angle X-ray Scattering (SAXS) and Wide-Angle X-ray Scattering (WAXS) of Supramolecular Assemblies. *Supramol. Chem.* (2012). doi:10.1002/9780470661345.smc042

114. Svergun, D. I. Determination of the regularization parameter in indirect-transform methods using perceptual criteria. *J. Appl. Crystallogr.* **25,** 495 503 (1992).

115. Urbani, R. B. Dynamics in Microfluidics Measured by X-Ray Scattering Techniques. **6,** (2014).

116. Pfohl, T. *et al.* Controlled modification of microstructured silicon surfaces for confinement of biological macromolecules and liquid crystals. *Langmuir* **17,** 5343 5351 (2001).

117. Choi, M. C. *et al.* Ordered patterns of liquid crystal toroidal defects by microchannel confinement. *Proc. Natl. Acad. Sci. U. S. A.* **101,** 17340 4 (2004).

118. Idziak, S., Koltover, I., Israelachvili, J. & Safinya, C. Structure in a Confined Smectic Liquid Crystal with Competing Surface and Sample Elasticities. *Phys. Rev. Lett.* **76,** 1477 1480 (1996).

119. Nogales, A., Hsiao, B. S., Somani, R. H., Srinivas, S. & Tsou, A. H. Shear-induced crystallization of isotactic polypropylene with different molecular weight distributions : in situ small- and wide-angle X-ray scattering studies. *Polymer (Guildf).* **42,** 5247 5256 (2001).

120. Livolant, F., Levelut, a M., Doucet, J. & Benoit, J. P. The highly concentrated liquid-crystalline phase of DNA is columnar hexagonal. *Nature* **339,** 724 726 (1989).

121. Castelletto, V., Itri, R., Amaral, L. Q. & Spada, G. P. Small-Angle X-Ray-Scattering of DNA Fragments - Form and Interference Factors. *Macromolecules* **28,** 8395 8400 (1995).

122. Giambaşu, G. M. *et al.* Competitive interaction of monovalent cations with DNA from 3D-RISM. *Nucleic Acids Res.* **43,** 8405–8415 (2015).

123. Ettig, R., Kepper, N., Stehr, R., Wedemann, G. & Rippe, K. Dissecting DNA-histone interactions in the nucleosome by molecular dynamics simulations of dna unwrapping. *Biophys. J.* **101,** 1999–2008 (2011).

124. Evans, H. M. *et al.* Structural polymorphism of DNA-dendrimer complexes. *Phys. Rev. Lett.* **91,** 75501 (2003).

125. Jacques, D. A. & Trewhella, J. Small-angle scattering for structural biology - Expanding the frontier while avoiding the pitfalls. *Protein Sci.* **19,** 642–657 (2010).

126. Putnam, C. D., Hammel, M., Hura, G. L. & Tainer, J. a. X-ray solution scattering (SAXS) combined with crystallography and computation: defining accurate macromolecular structures, conformations and assemblies in solution. *Q. Rev. Biophys.* **40,** 191–285 (2007).

127. Janmey, P. A., Slochower, D. R., Wang, Y.-H., Wen, Q. & Cēbers, A. Polyelectrolyte properties of filamentous biopolymers and their consequences in biological fluids. *Soft Matter* **10,** 1439–49 (2014).

128. Bausch, a. R. & Kroy, K. A bottom-up approach to cell mechanics. *Nat. Phys.* **2,** 231–238 (2006).

129. Huber, F. *et al.* Emergent complexity of the cytoskeleton: from single filaments to tissue. *Adv. Phys.* **62,** 1–112 (2013).

130. Yang, C., Hoelzle, M., Disanza, A., Scita, G. & Svitkina, T. Coordination of membrane and actin cytoskeleton dynamics during filopodia protrusion. *PLoS One* **4,** 1–9 (2009).

131. Köster, S. & Pfohl, T. An in vitro model system for cytoskeletal confinement. *Cell Motil. Cytoskeleton* **66,** 771–776 (2009).

132. Steinhauser, D., Köster, S. & Pfohl, T. Mobility Gradient Induces Cross-Streamline Migration of Semi-flexible Polymers. *ACS Macro Lett.* **1,** 541–545 (2012).

133. Soares e Silva, M. *et al.* Self-organized patterns of actin filaments in cell-sized confinement. *Soft Matter* **7,** 10631 (2011).

134. Swank, Z., Deshpande, S. & Pfohl, T. Trapping, entrainment and synchronization of semiflexible polymers in narrow, asymmetric confinements. *Soft Matter* **12,** 87–92 (2016).

135. Hirst, L. S. *et al.* Microchannel systems in titanium and silicon for structural and mechanical studies of aligned protein self-assemblies. *Langmuir* **21,** 3910–3914 (2005).

136. Deshpande, S. & Pfohl, T. Hierarchical self-assembly of actin in micro-confinements using microfluidics. *Biomicrofluidics* **6,** 1–13 (2012).

137. Kim, S., Kim, H. J. & Jeon, N. L. Biological applications of microfluidic gradient devices. *Integr. Biol. (Camb).* **2,** 584–603 (2010).

138. Toh, A. G. G., Wang, Z. P., Yang, C. & Nguyen, N. T. Engineering microfluidic concentration gradient generators for biological applications. *Microfluid. Nanofluidics* **16,** 1–18 (2014).

139. Berthier, E. & Beebe, D. J. Gradient generation platforms: new directions for an established microfluidic technology. *Lab Chip* 3241–3247 (2014).

140. Huang, Y., Agrawal, B., Sun, D., Kuo, J. S. & Williams, J. C. Microfluidics-based devices: New tools for studying cancer and cancer stem cell migration. *Biomicrofluidics* **5,** 13412 (2011).

141. Wu, X. *et al.* Analysis of CCR7 mediated T cell transfectant migration using a microfluidic gradient generator. *J. Immunol. Methods* **419,** 9–17 (2015).

142. Culbertson, C. Diffusion coefficient measurements in microfluidic devices. *Talanta* **56,** 365–373 (2002).

143. Cussler, E. L. *Diffusion: Mass Transfer in Fluid Systems*. (Cambridge University Press, 1997).

144. Boal, D. *Mechanics of the Cell*. *Cambridge University Press* (2002).

145. Xu, J. Y., Palmer, a & Wirtz, D. Rheology and microrheology of semiflexible polymer solutions: Actin filament networks. *Macromolecules* **31,** 6486–6492 (1998).

146. Tang, J. X. & Janmey, P. A. The polyelectrolyte nature of F-actin and the mechanism of actin bundle formation. *J. Biol. Chem.* **271,** 8556–8563 (1996).

147. Isambert Herve, Venier Pascal, Maggs Anthony C., F. A. Flexibility of Actin Filaments Derived from Thermal Fluctuations. *J. Biol. Chem.* **270,** 11437–11444 (1995).

148. Scharf, R. E. & Newman, J. Mg- and Ca-actin filaments appear virtually identical in steady-state as determined by dynamic light scattering. *Biochim. Biophys. Acta.* **1245,** 129–132 (1995).

149. Gardel, M. L., Valentine, M. T., Crocker, J. C., Bausch, A. R. & Weitz, D. A. Microrheology of Entangled F-Actin Solutions. *Phys. Rev. Lett.* **91,** 158302 (2003).

150. Lee, H., Ferrer, J. M., Nakamura, F., Lang, M. J. & Kamm, R. D. Passive and active microrheology for cross-linked F-actin networks in vitro. *Acta Biomater.* **6,** 1207 1218 (2010).

151. Wu, Z. L. *et al.* Anisotropic hydrogel from complexation-driven reorientation of semirigid polyanion at Ca2+ diffusion flux front. *Macromolecules* **44,** 3535 3541 (2011).

152. Pfohl, T., Mugele, F., Seemann, R. & Herminghaus, S. Trends in Microfluidics with Complex Fluids. *ChemPhysChem* **4,** 1291 1298 (2003).

153. Squires, T. M. Microfluidics: Fluid physics at the nanoliter scale. *Rev. Mod. Phys.* **77,** (2005).

154. Chelakkot, R., Winkler, R. G. & Gompper, G. Flow-induced helical coiling of semiflexible polymers in structured microchannels. *Phys. Rev. Lett.* **109,** 1 5 (2012).

155. Kantsler, V. & Goldstein, R. E. Fluctuations, dynamics, and the stretch-coil transition of single actin filaments in extensional flows. *Phys. Rev. Lett.* **108,** 1 5 (2012).

156. Young, Y. N. & Shelley, M. J. Stretch-coil transition and transport of fibers in cellular flows. *Phys. Rev. Lett.* **99,** 3 6 (2007).

157. Manikantan, H. & Saintillan, D. Buckling transition of a semiflexible filament in extensional flow. *Phys. Rev. E* **92,** 41002 (2015).

158. Golubovic, L., Moldovan, D. & Peredera, A. Flexible polymers and thin rods far from equilibrium: Buckling dynamics. *Phys. Rev. E* **61,** 1703 1715 (2000).

159. Harasim, M., Wunderlich, B., Peleg, O., Kröger, M. & Bausch, A. R. Direct observation of the dynamics of semiflexible polymers in shear flow. *Phys. Rev. Lett.* **110,** 108302 (2013).

160. Guglielmini, L., Kushwaha, A., Shaqfeh, E. S. G. & Stone, H. A. Buckling transitions of an elastic filament in a viscous stagnation point flow. *Phys. Fluids* **24,** (2012).

161. Levy, S. L. & Craighead, H. G. DNA manipulation, sorting, and mapping in nanofluidic systems. *Chem. Soc. Rev.* **39,** 1133 (2010).

162. Huber, B., Harasim, M., Wunderlich, B., Kröger, M. & Bausch, A. R. Microscopic origin of the non-newtonian viscosity of semiflexible polymer solutions in the semidilute regime. *ACS Macro Lett.* **3,** 136 140 (2014).

163. Manikantan, H. & Saintillan, D. Subdiffusive transport of fluctuating elastic filaments in cellular flows. *Phys. Fluids* **25,** (2013).

164. Xia, Y. & Whitesides, G. M. Soft Lithography. *Annu. Rev. Mater. Sci.* 153 184 (1998).

165. Powers, T. R. Dynamics of filaments and membranes in a viscous fluid. *Rev. Mod. Phys.* **82,** 1607 1631 (2010).

166. Wen, Q. & Janmey, P. A. Polymer physics of the cytoskeleton. *Curr. Opin. Solid State Mater. Sci.* **15,** 177 182 (2011).

167. Rubinstein, M. & Colby, R. H. Polymer physics. *Polymer International* 440 (2003).

168. Uppaluri, S. *et al.* Impact of microscopic motility on the swimming behavior of parasites: Straighter Trypanosomes are more directional. *PLoS Comput. Biol.* **7,** 1 8 (2011).

169. Nöding, B. & Köster, S. Intermediate filaments in small configuration spaces. *Phys. Rev. Lett.* **108,** 88101 (2012).

170. Landecker, H. Seeing things : from microcinematography to live cell imaging. *Nat. Methods* **6,** 707 709 (2009).

171. Deng, J. *et al.* Simultaneous cryo X-ray ptychographic and fluorescence microscopy of green algae. *PNAS* **112,** 2314 2319 (2015).

172. Miao, J., Ishikawa, T., Robinson, I. K. & Murnane, M. M. Beyond crystallography: Diffractive imaging using coherent x-ray light sources. *Science* **348,** 530 535 (2015).

173. Hemonnot, C. J. *et al.* X-rays Reveal the Internal Structure of Keratin Bundles in Whole Cells. *ACS Nano* **10,** 3553–3561 (2016).

174. Forsburg, S. L. & Rhind, N. Basic methods for fission yeast. *Yeast* **23,** 173 183 (2006).

175. Spitz, D. R., Azzam, E. I., Li, J. J. & Gius, D. Metabolic oxidation / reduction reactions and cellular responses to ionizing radiation : A unifying concept in stress response biology. *Cancer Metastasis Rev* **23,** 311 322 (2004).

176. Howells, M. R. *et al.* An assessment of the resolution limitation due to radiation-damage in X-ray diffraction microscopy. *J. Electron Spectros. Relat. Phenomena* **170,** 4 12 (2009).

177. Schneider, G., Guttmann, P., Rehbein, S., Werner, S. & Follath, R. Cryo X-ray microscope with flat sample geometry for correlative fluorescence and nanoscale tomographic imaging. *J. Struct. Biol.* **177,** 212 223 (2012).

178. Kimura, T. *et al.* Imaging live cell in micro-liquid enclosure by X-ray laser diffraction. *Nat. Commun.* **5,** 3052 (2014).

179. Weinhausen, B. *et al.* X-ray nano-diffraction on cytoskeletal networks. *New J. Phys.* **14,** (2012).

180. Lima, E. *et al.* Cryo-scanning x-ray diffraction microscopy of frozen-hydrated yeast. *J. Microsc.* **249,** 1 7 (2013).

181. Sedlmair, J. *et al.* Imaging of Vascular Smooth Muscle Cells with Soft X-Ray Spectromicroscopy. *Microsc. Microanal.* **17,** 991 1001 (2011).

182. Guizar-Sicairos, M. & Fienup, J. R. Phase retrieval with transverse translation diversity: a nonlinear optimization approach. *Opt. Express* **16,** 7264 7278 (2008).

183. Thibault, P. *et al.* High-Resolution Scanning X-ray Diffraction Microscopy. *Science* **321,** 379 383 (2008).

184. Thibault, P. & Guizar-Sicairos, M. Maximum-likelihood refinement for coherent diffractive imaging. *New J. Phys.* **14,** 63004 (2012).

185. Guizar-Sicairos, M. *et al.* Role of the illumination spatial-frequency spectrum for ptychography. *Phys. Rev. B - Condens. Matter Mater. Phys.* **86,** 1 4 (2012).

186. Weisman, L. S. Organelles on the move : insights from. *Nat Rev Mol Cell Biol* **7,** 243 252 (2006).

187. Pyo, J. O. *et al.* Essential roles of Atg5 and FADD in autophagic cell death: Dissection of autophagic cell death into vacuole formation and cell death. *J. Biol. Chem.* **280,** 20722 20729 (2005).

188. Suzuki, K. & Ohsumi, Y. Molecular machinery of autophagosome formation in yeast, Saccharomyces cerevisiae. *FEBS Lett.* **581,** 2156 2161 (2007).

189. Tsukada, M. Isolation and characterization of autophagy-defective mutants of Saccharomyces cerevisiae. *FEBS Lett.* **333,** 169 174 (1993).

190. Mahmoud, B. S. M. The effects of X-ray radiation on Escherichia coli O157 : H7 , Listeria monocytogenes , Salmonella enterica and Shigella fl exneri inoculated on whole Roma tomatoes q. *Food Microbiol.* **27,** 1057 1063 (2010).

191. Mizushima, N. Autophagy : process and function. *Genes Dev* **21,** 2861 2873 (2007).

192. Palumbo, S. & Comincini, S. Autophagy and ionizing radiation in tumors: The 'survive or not survive' dilemma. *J. Cell. Physiol.* **228,** 1 8 (2013).

193. Henrich, B. *et al.* PILATUS: A single photon counting pixel detector for X-ray applications. *Nucl Instr Meth Phys Res* **607,** 247 249 (2009).

194. Thibault, P., Dierolf, M., Bunk, O., Menzel, A. & Pfeiffer, F. Probe retrieval in ptychographic coherent diffractive imaging. *Ultramicroscopy* **109,** 338 343 (2009).

195. Huang, X. *et al.* Optimization of overlap uniformness for ptychography. *Opt. Express* **22,** 12634 12644 (2014).

196. Wilke, R. N. *et al.* Hard X-ray imaging of bacterial cells : nano-diffraction and ptychographic reconstruction. **20,** 4795 4797 (2012).

197. Gullikson, E. http://henke.lbl.gov/optical_constants/.

198. Dierolf, M. *et al.* Ptychographic coherent diffractive imaging of weakly scattering specimens. *New J. Phys.* **12,** (2010).

199. Holler, M. *et al.* X-ray ptychographic computed tomography at 16 nm isotropic 3D resolution. 1 5 (2013). doi:10.1038/srep03857

200. Heel, M. Van & Schatz, M. Fourier shell correlation threshold criteria q. **151,** 250 262 (2005).

201. Vila-comamala, J. *et al.* Characterization of high-resolution diffractive X-ray optics by ptychographic coherent diffractive imaging. **19,** 175 184 (2011).

Publications

N. Strelnikova, N. Sauter, M. Guizar-Sicairos, M. Göllner, A. Diaz, P. Delivani, M. Chacon, I. Tolic-Norrelykke, V. Zaburdaev and T. Pfohl. Live cell X-ray imaging of autophagic vacuoles formation and chromatin dynamics in fission yeast. *Scientific Reports*, 7, 13775 (**2017**)

N. Strelnikova*, M.Göllner* and T. Pfohl. Direct observation of alternating stretch-coil and coil-stretch transitions of semiflexible polymers in microstructured flow. *Macromolecular Chemistry and Physics* 218, 1600474 (**2017**) *contributed equally

N. Strelnikova, F. Herren, C.A. Schoenenberger and T. Pfohl. Formation of Actin Networks in Microfluidic Concentration Gradients. *Front. Mater* 3, 20 (**2016**)

M. Göllner, A. C. Toma, N. Strelnikova, S. Deshpande and T. Pfohl. A self- filling microfluidic device for noninvasive and time-resolved single red blood cell experiments. *Biomicrofluidics* 10, 054121 (**2016**)

D. Witzigmann, S. Sieber, F. Porta, P. Grossen, A. Bieri, N. Strelnikova, T. Pfohl, C. Prescianotto-Baschong, J. Huwyler. Encapsulation of Gold Nanoparticles to Visualize Intracellular Localization of Lipid and Polymer Based Nanocarriers. *CRS Newsletter* 33, 12-14 (**2016**)

D. Witzigmann, S. Sieber, F. Porta, P. Grossen, A. Bieri, N. Strelnikova, T. Pfohl, C. Prescianotto-Baschong, J. Huwyler. Formation of Lipid and Polymer Based Gold Nanohybrids Using a Nanoreactor Approach. *RSC Adv.* 5, 74320 74328 (**2015**)

M. Turks, N. Strelnikova, V. Kumpins, U. Kalejs. Synthesis of Enantiomerically Enriched 1,2,3- Triazole-derivatized Homoalanines. *Material Science and Applied Chemistry.* 28, 21-28 (**2013**)

Acknowledgements

I would like to express my sincere gratitude to my supervisor **Thomas Pfohl** for giving me the opportunity to do a PhD in his group, guiding me through all the projects and for continuous support during my PhD studies. I am thankful for his patience, care, concern, support and immense knowledge. I could not have imagined having a better supervisor for my PhD studies.

I am very grateful to **Cornelia Palivan** for being my co-referee and **Wolfgang Meier** for being the faculty representative. Thank you for providing me the opportunity to join your group and creating a kind and helpful atmosphere. Without you, my PhD would not have been accomplished.

I also would like to thank all my colleagues for the friendly and cooperative time we spent together. Especially **Michael Göllner**, for his support, encouragement and for being more than just a colleague. I am very grateful to **Raphael** for the introduction to SAXS and for his endured help during my PhD. **Siddharth**, thank you for sharing your knowledge about actin**.** I would like to thank **Axel** for showing me how to use the clean room and making the devices. **Nora**, I would like to thank you for the great time we spent together at the PSI and at ESRF. I will always remember the walk in the night though the forest together with you. **Cora,** thank you for the great collaboration on one of the publications and for the Rat2sm9 fibroblast images. I also would like to thank **Adriana, Matteo** and **Michael Gerspach** for all the valuable discussions and suggestions.

My sincere thanks also go to all coauthors of the publications. Thank you for the fruitful and friendly collaborations and great outcome.

Finally, I would like to express a deep sense of gratitude to my parents and friends who gave me constant support and love during the completion of my thesis.

Curriculum Vitae

Personal Information

Name	Natalja Strelnikova
Date of birth	16.05.1987
Place of birth	Jelgava, Latvia
Nationality	Latvian

Education

2012 2017	PhD in Biophysics University of Basel
2010 2012	M.Sc. in Chemical Engineering Riga Technical University
2007 2010	B.Sc. in Chemical Engineering Riga Technical University